1-1-2013

RADAR Based Collision Avoidance for Unmanned Aircraft Systems

Allistair A. Moses
University of Denver

RADAR Based Collision Avoidance for Unmanned Aircraft Systems

---

A Dissertation

Presented to

the Faculty of the Daniel Felix Ritchie School of Engineering and Computer Science

University of Denver

In Partial Fulfillment

of the Requirements for the Degree

Doctor of Philosophy

---

by

Allistair A. Moses

August 2013

Advisors: Kimon P. Valavanis, Ph.D. and Matthew J. Rutherford Ph.D.

Author: Allistair Moses
RADAR Based Collision Avoidance for Unmanned Aircraft Systems
Advisor: Kimon P. Valavanis, Matthew J. Rutherford
Degree Date: August 2013

Abstract

Unmanned Aircraft Systems (UAS) have become increasingly prevalent and will represent an increasing percentage of all aviation. These unmanned aircraft are available in a wide range of sizes and capabilities and can be used for a multitude of civilian and military applications. However, as the number of UAS increases so does the risk of mid-air collisions involving unmanned aircraft. This dissertation aims to present one possible solution for addressing the mid-air collision problem in addition to increasing the levels of autonomy of UAS beyond waypoint navigation to include preemptive sensor-based collision avoidance. The presented research goes beyond the current state of the art by demonstrating the feasibility and providing an example of a scalable, self-contained, RADAR-based, collision avoidance system. The technology described herein can be made suitable for use on a miniature (Maximum Takeoff Weight $<$ 10kg) UAS platform. This is of paramount importance as the miniature UAS field has the lowest barriers to entry (acquisition and operating costs) and consequently represents the most rapidly increasing class of UAS.

Acknowledgments

This work was made possible through the dedication of my family, friends, and coworkers. Without their support none of this would have been possible. In particular, I would like thank my advisers, Dr. Kimon Valavanis, and Dr. Matthew Rutherford for their guidance and support. Additionally, the contributions of Dr. Richard Garcia by means of his constant friendship and advice cannot be emphasized enough. Any success I have had up to this point is a by product of the training I received from my father and mother: Glenroy and Cheryl Moses. Thank you for making me who I am today. Finally, I would like to thank Amanda Lacy for her limitless patience and understanding throughout this process.

Table of Contents

List of Figures

List of Tables

Chapter 1

Introduction

Modern Unmanned Aircraft Systems (UAS) are available in a wide range of sizes from the palm-sized "Black Widow" to the 39.8 meter wingspan Global Hawk[9][10]. At the time of this writing, most modern UAS are generally limited to autonomously following pre-programmed waypoints or executing pre-programmed commands while under the supervision of a human operator. Only recently are UAS beginning to operate with some level of independence from pre-programmed commands as demonstrated by [11] in which a miniature quadrotor UAV autonomously constructs a map of an indoor environment. However, these exercises have, largely been limited to computer vision and laser rangefinder based systems operating in an indoor environment.

One of the next steps for UAV technology development is to enable unmanned systems to perform the same tasks in an outdoor environment with a similar level of safety and autonomy. This level of autonomy is challenging in many ways due to the different sensor arrangements required when transitioning to the outdoor environment. This sensor paradigm shift is typically necessitated by the fact that many of

the sensors used in indoor laboratory conditions are not well suited for the demands of UAV operation in an outdoor environment due to the longer ranges, higher speeds, and environmental factors normally encountered. More importantly, the threats to safe operation are dramatically different in regulated airspace wherein the risk of a collision between a manned aircraft and an UAS exists.

There are a number of existing solutions to address the mid-air collision problem. These solutions are typically divided into two categories which may be combined to form a complete collision avoidance solution: transponders and non-cooperative sensors.

There are a number of transponder solutions including *Traffic Collision Avoidance System* (TCAS), *Portable Collision Avoidance System* (PCAS), *FLight AlaRM* (FLARM), and *Automatic Dependent Surveillance and Broadcast* (ADS-B) [12][13][14][15]. The TCAS transponders (currently required in the U.S. for turbine powered, aircraft with more than 10 seats) function by interrogating other TCAS transponders to determine heading, velocity, and altitude information while simultaneously responding to TCAS interrogations from opposing aircraft [16]. If a collision is detected, the TCAS automatically determines a collision avoidance maneuver and presents the information to the pilot via a cockpit display. TCAS is an effective solution for manned aircraft, however, the cost of a typical installation is often prohibitive for many general aviation craft, which comprise a substantial portion of the aircraft population [17][18]. To address this issue, PCAS receivers have been made available for under 2000USD [19]. PCAS receivers achieve this cost reduction, in part, by the elimination of the transmit functionality present within TCAS transponders. In essence, PCAS receivers listen for TCAS signals and determine the risk of collision without transmitting their own location. In this fashion, PCAS equipped aircraft can

actively avoid TCAS equipped aircraft. However, the passive nature of PCAS makes it unsuited for avoiding collisions with other PCAS equipped aircraft, nor does it allow TCAS equipped aircraft to detect or avoid PCAS equipped aircraft. There are a wide range of flight regimes present throughout aviation including many cases where aircraft routinely operate in close proximity to each other without the risk of a mid-air collision. Manned gliders are useful examples of this type of flight. The FLARM transponder was developed to provide a collision avoidance solution for aircraft operating under these conditions. FLARM utilizes barometric pressure and GPS data to estimate the host vehicle's location and velocity vector. It then broadcasts this data to the airspace while listening for position and velocity information from other FLARM devices. If a mid-air collision situation arises, the FLARM transponder alerts the pilot who can then take action if necessary. The final transponder system, ADS-B, is currently poised to supersede secondary surveillance RADAR (which is based on RADAR transponders located on board aircaft) as the primary air traffic control method. ADS-B operates in a manner similar to FLARM but adds additional features such as weather and terrain data broadcast by ground stations [15]. While ADS-B use is not currently required, the FAA aims to make it mandatory for all aircraft by January 1st, 2020 [20]. The common theme with all the transponder solutions is the need for cooperative infrastructure if collisions are to be successfully avoided.

In contrast to the cooperative nature of transponders, sensor-based collision avoidance otherwise known as "Sense and Avoid" (SAA) systems typically do not require cooperation between aircraft to effect a useful collision avoidance solution. There are a number of prototype systems utilizing a wide range of sensor technologies. These technologies include acoustic sensors, laser rangefinders, and camera

systems (both visible and infrared wavelengths). This dissertation describes the development of an additional SAA system based on Radio Detection and Ranging (RADAR) [21][22][23][24]. More specifically, this dissertation investigates the use of RADAR technology for the detection and identification of miniature (MTOW<10kg) UAVs. Additionally, vertical and horizontal collision avoidance maneuvers are compared and a computationally-efficient method for collision avoidance is proposed and evaluated.

1.1 Why RADAR?

RADAR has a well established history dating back to Heinrich Hertz's initial experiments in 1886. The publication of Heinrich Hertz's book documenting his experiments form the foundation of modern radio concepts. [25]

The use of RADAR for active detection of objects was first demonstrated by Christian Hulsmeyer who created a device he called the Telemobiloscope. This device, patented in 1904, transmitted broadband Radio Frequency (RF) energy in a wide pattern while observing reflections with a narrow beam antenna which could be directed in order to make observations of a specific area. Originally intended for use in an anti-collision role in a maritime environment, the device never saw widespread acceptance [26].

RADAR was significantly advanced during the 1930s and 1940s in the United Kingdom, Germany, and the United States. The demands of World War II facilitated many innovations and RADAR technology advanced rapidly during this period. Previously, only limited to ground installations, RADARS soon became small enough to install in aircraft [27]. After WWII RADAR applications in the civilian

domain continued to increase, particularly with regard to civilian aviation. This trend continues to this day [28].

RADAR-based sensors have a number of distinct advantages when compared with other sensor types such as LASER rangefinders, computer vision / focal plane arrays, acoustic sensors, etc... Unlike optical systems, RADARs are not affected by sunlight, smoke, fog, dust, and other factors that typically affect optical wavelengths. Furthermore RADARs typically have improved directionality and range characteristics when compared with acoustic systems, additionally, RADAR systems can be used on-board aircraft with high levels of acoustic noise and can detect aircraft with little to no acoustic noise emissions (something that is increasingly important as the number of UAS using electric propulsion increases). At present, no other non-cooperative sensor type provides all these capabilities [29].

1.2 Existing Challenges

There are a number of existing challenges that preclude the widespread adoption of collision avoidance RADARs on UAS. The first challenge is the physical volume and mass of many RADAR systems as most currently available RADAR systems are far too large for widespread UAS implementation.

Furthermore, most airborne RADAR systems currently installed on UAS are designed for use in Air-to-Ground modes either for mapping or for target detection/tracking purposes. An example of such a system is ImSAR's NanoSAR line of Synthetic Aperture RADARs (SAR) [30][31]. This dedication to the Air-to-Ground operating mode often inhibits effective use when attempting to use the RADAR for air-to-air operations. This is because additionally Air-to-Air RADARs must of-

ten incorporate ground clutter rejection features not typically present in dedicated Air-to-Ground RADARs.

Power consumption is another area that must be addressed before widespread collision avoidance RADAR becomes a reality. Many airborne RADARs require hundreds of watts of electrical power to operate. This is often unavailable on small UAS. There are however, some small RADAR systems with low electrical power consumption. The NanoSAR B utilizes 30 Watts of electrical power.

Finally, one of the more important issues that must be addressed is the prohibitive cost of many airborne RADAR solutions. Existing systems can easily cost upwards of 100,000 USD and greatly exceed the cost of UAS platforms with MTOWs $<$ 50kg [30].

1.3 Contributions

The primary contribution of this work is the development and evaluation of a scalable framework for RADAR-based collision avoidance system suitable for implementation on UAS. The contributions are summarized as follows:

1. Development and testing (on a small scale) of hardware technologies suitable for collision avoidance on UAS. That can also be scaled to be applicable on a wide range of UAS.

2. Development of real-time techniques for the identification of UAS based on their micro Doppler signature.

3. Development of a real-time, computationally efficient collision avoidance algorithm that incorporates threat identity to improve overall performance.

1.4 Organization of Dissertation

The remainder of this Dissertation is organized as follows: Chapter 2 provides a literature review to provide some background information on various RADAR technologies and collision avoidance methods. Chapter 3 describes the RADAR hardware developed throughout the course of this research. Chapter 4 details the micro Doppler signal sources, target identification ranges and the target identification methodology. In addition, experimental results are provided for the target identification and localization functions. Chapter 5 describes the collision detection and evasion method and simulations are provided to demonstrate the efficacy of the proposed approach. Finally, chapter 6 summarizes the research performed throughout this dissertation and describes the work needed to further advance the technology.

Chapter 2

Related Work

Substantial research and development work has been performed regarding collision avoidance. The following literate review investigates two subsets of the general collision avoidance body of work: RADAR for collision avoidance, and the algorithms used for detecting collisions and planning an collision avoidance path.

2.1 RADAR for Automotive Collision Avoidance

RADAR has seen widespread adoption in the automotive industry. In this market, RADARs are used primarily for adaptive cruise control systems wherein the RADAR serves to provide information to the vehicle's computers so that a specified distance between the host vehicle and the vehicle ahead can be maintained. These systems are also capable of applying the brakes and stopping a vehicle without driver intervention [32]. RADAR systems are also capable of providing more information than line of sight range.

The versatility of RADAR in the autonomous ground vehicle arena is demonstrated by a number of research groups: Viikari et al developed a 24GHz automotive RADAR capable of identifying road conditions (icy, gravel, sand, etc...) by measuring the polarization of the backscattered energy [33]. Bartsch, et al demonstrates the development and applicability of micro Doppler modulation target profiles in pedestrians, and the differentiation of slowly moving pedestrians from static objects [34].

In addition to expanding the capabilities of RADAR sensors, the constraints of the automotive industry, with its emphasis on cost effectiveness, has given rise to a number of innovative system packaging arrangements and antenna designs [35].

2.2 RADAR for UAV Collision Avoidance

The use of RADAR systems for UAS collision avoidance is a natural application of RADAR research and has been explored by a number of researchers and commercial groups:

In [36] Richley, et. al. detail the development of a miniature Ultra Wide Band (UWB) RADAR for micro air vehicles. They demonstrate the applicability of RADAR technology to very small UAVs often less than 15cm in any dimension. The use of UWB technologies substantially decreases the power requirements and mass of the RADAR sensor, to 0.8 watts peak and 42.5 grams, respectively.

In [37] Viquerat et. al., demonstrate the viability of miniature Doppler RADAR as a collision avoidance sensor. Their work produced a lightweight (304 grams) continuous wave Doppler sensor consisting of 4 transmit-receive modules arranged in a quadrant pattern. This allows for the ready implementation of what they describe

as a "Reactive Collision Avoidance Algorithm" wherein the host vehicle steers away from the quadrants with the highest returned signal energy.

Fully operational systems, however, are not widely discussed in the literature. The only example of a real-world, full-scale (vehicles with comparable size to manned aircraft), UAV-based sense and avoid RADAR system is the SkySense 2020H from ITT Exelis which is set to achieve initial operational capability on the MQ-4C by 2015 [38]. The SkySense system utilizes a number of discrete, electronically steered active arrays to achieve the requisite field of regard. These modules can be arranged around the aircraft to expand the fields of regard (observation angles) as needed.

2.3 Target Identification Using RADAR

The use of RADAR systems for determining the type (and often the model) of vehicle(s) within the current scene is not new. This functionality has been present in larger vehicles and installations including most modern military aircraft. The level of detail possible is readily demonstrated:

In 1998, Wellman R.J, and Silvious J.L. of the U.S. Army Research Laboratory published technical report ARL-TR-1637 [39]. In this document they provide a description of their use of a 92GHz Doppler RADAR system to characterize the spectral shifts generated by a full scale helicopter, in this case a Mil Mi-24 Hind-D. They achieve this by first measuring the diameters and angular rates of the various rotating structures within the aircraft including: the main and tail rotor blades and hub components, the Auxiliary Power Unit (APU), oil coolers, and engine compressors and free turbines. The Doppler shift generated by these components is then associated with the tip velocity of the rotating structures. Experimental

validation proved that their model is quite accurate. Their prediction of the turbine compressor Jet Engine Modulation (JEM) spectral lines deviated from the measured values by 1.6%. This research is important as it forms the foundation for the work done in Section 4.1.

For large scale vehicles, and especially in the case of turbine powered systems, identification is eased by the possibility of sensing not only the larger aerodynamic components, but also the Doppler modulation caused by the power source. Indeed, JEM is one of the foremost methods of target identification in addition to or in the absence of large periodically rotating parts (e.g. a helicopter rotor system) [4]. Applying this research to miniaturized vehicles (of the type used in this dissertation) is not impossible, but is hampered by the extensive use of plastics and other dielectrics that typically comprise class 1 UAS. However, in larger class 1 UAS utilizing miniature gas turbine engines, or Electric Ducted Fans (EDF) JEM becomes valuable for target identification.

Additionally, even in the absence of large (with respect to the wavelength of the carrier) or complex structures (such as jet engine compressors), identification of UAV-scale vehicles is still possible, albeit at shorter ranges and higher frequencies. This is because the integral components of smaller vehicles modulate electromagnetic radiation in a manner comparable to large scale systems. This property is being exploited by Aerophysics Inc who received a DARPA grant in 2009 to develop an anti-UAV system [40]. However, information regarding the progress of Aerophysics' research is not forthcoming due to the sensitive nature of militarized systems.

2.4 Collision Avoidance Path Planning

There exists a substantial body of work dedicated to the collision avoidance problem for mobile robots. The following sections describe the related work done as it relates specifically to aircraft. This is due to the unique constraints present in an aerial environment (minimum velocity, acceleration limits, etc...).

2.4.1 Grid-Type Approaches

Grid-type approaches involve the discretization of the airspace into cells. For some grid-type approaches, each cell is connected to its neighbors by a weighted connection representing the "cost" of traversing from the present cell to a neighboring cell. Other grid-type approaches apply the weights to the cells themselves. Nevertheless, in both approaches, transitions to cells containing obstacles will have a relatively high / infinite cost, while transitions to cells without obstacles will have a low cost. Collision avoidance is performed by using a minimum cost algorithm to determine an appropriate path to the destination.

One of the more popular minimum cost algorithms, A*, has been applied to the task of UAV path planning by Ruz and others [41]. The discretized nature of the grid approach requires some constraints however. Ruz describes the application of two such constraints: flying direction and inertial. As most aircraft types (with the exception of Vertical Takeoff and Landing (VTOL) craft) cannot hover, fly backwards, or execute extremely tight turns, the search algorithm is constrained to only investigate paths between +90 and -90 degrees from the current flight path. Furthermore, given the same physical limitations of most aircraft, the inertial constraint takes into account the minimum flight velocity and therefore the overshoot involved

at end nodes. Nevertheless, the dynamic nature of multi-agent collision avoidance compromises the applicability of a pure A* approach for real time UAV collision avoidance [42]. [43] describes enhancements to the pure A* approach to adapt it for UAV collision avoidance. These modification include the use of heuristics to reduce computation time and a prediction mechanism to modify the cost of cells in a manner corresponding to the motion of the opposing aircraft. Nevertheless, grid-type approaches are not utilized in this dissertation due to the relatively high computational requirements, and the need for a software pipeline approach to smooth the generated paths: The A* method will generate a meandering path consisting of a very coarse set of angles relative to the UAS flight vector: $\pm 90°$, $\pm 45°$, and $0°$. This meandering path is almost certainly unnavigable. Therefore, a smoothing/curve-fitting operation must be performed to translate the highly discontinuous path generated by A* to a continuous path that can be input into the UAS navigation computer.

Another grid-type approach is the Vector Field Histogram (VFH) which was first proposed in 1991 [1]. The algorithm functions utilizing three operations. First, an occupancy grid is updated where the value of each cell represents the probability of that location being occupied by an obstacle. Next, a polar-format histogram vector is generated from the host vehicle's perspective by summing the values of the cells along a range of heading vectors. Finally, the collision avoidance heading is selected by setting the polar histogram vector values whose magnitude is below a false alarm threshold to zero then adjusting the host vehicle's heading to align with a section of zero valued histogram values that are closest to the host vehicle's current heading. An illustration of this process is shown in Figure 2.1.

VFH collision avoidance is not utilized in this research because it fails to take into account the dynamic nature of the airspace. Adapting VFH to dynamic environments

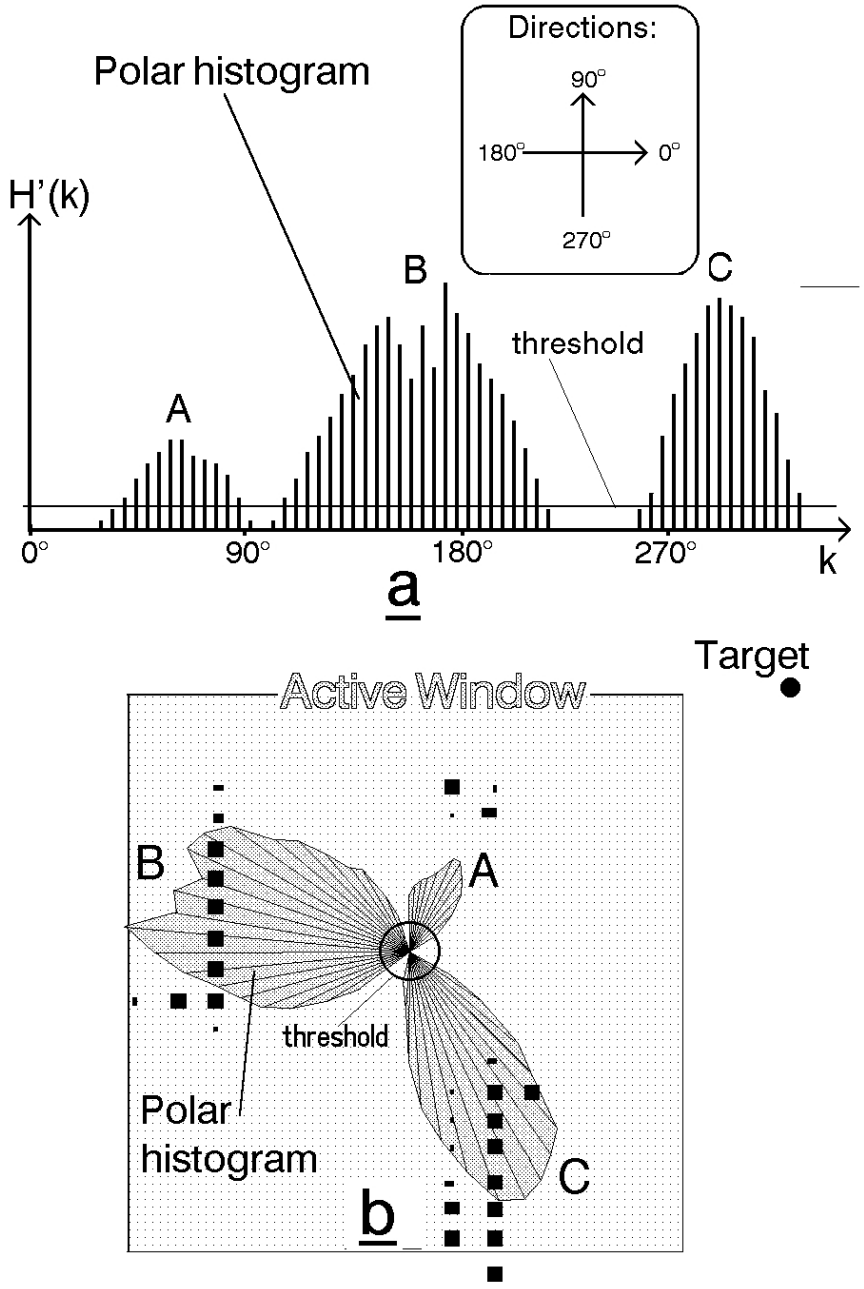

Figure 2.1: Vector Field Histogram Collision Avoidance [1]

requires a look-ahead function which modifies the cost of the occupancy grid based on the estimated future positions of the vehicles within the sensor field of view [44]. This process is often computationally intensive.

2.4.2 Potential Fields

Artificial potential fields are a scalable method for simultaneously avoiding collisions while navigating towards a goal. This is achieved by modeling goals as attractive forces and obstacles as repelling forces [45][46]. The superposition of these forces gives rise to a continuous field wherein the host vehicle can navigate by following the steepest slope towards the attractive forces. The applicability of potential fields to UAS guidance is demonstrated by Ruchti et. al. who use heuristics to correct the issues that typically plague potential field approaches, namely local minima and oscillations [46][47]. For example, the deadlock scenario (when two aircraft approach each other on a co-linear path) is addressed by forcing a 15 degree heading shift to the right in both aircraft then resuming normal operations once the collision is resolved. Local minima have similar resolution methods where in an algorithm will detect the repeating circular flight path caused by a local minima then modify the flight path accordingly. The potential-field method was considered for use in this research, but was ultimately rejected due to the problems with local minima. As described above, there exist a number of ways of detecting and escaping from a local minima condition. However, in the absence of a high level path planner, the current methods require the vehicle to be trapped in the local minima prior to initiating an escape maneuver. In a highly dynamic environment typical of high-density airspace, such oscillations are highly undesirable due to the amount of time consumed in their detection.

2.4.3 Linear Programming

Linear programming is often used to optimize a linear cost function given a set of linear constraints. Richards et. al. demonstrated the applicability of linear programming to UAV path planning [48]. In their implementations, the linear constraints include closest approach values, maximum and minimum velocities and minimum turning radii for the aircraft in question. These constraints are implemented by modeling the aircraft as a point mass then applying force vectors to it with the finite value of the force and its direction serving to generate the desired dynamics. Although linear programming provides efficient paths for the aircrafts in question to follow, calculating these paths is computationally intensive with the computation time increasing exponentially as the number of constrains/aircraft increases. There are methods for dealing with this complexity as demonstrated by Bellingham where in linear programming is applied using model predictive control [49]. This sacrifices the optimality of the solutions obtained by linear programming in order to decrease processing time. Linear programming, however, still requires significant computing power. This, combined with the exponential processing time increases while computing paths for multiple agents, results in this algorithm not being suited for real-time collision avoidance in the context of this research.

2.4.4 Genetic Algorithms

Conde et al. demonstrate an efficient collision detection method coupled with a genetic algorithm for conflict resolution [50]. Detection is first performed by surrounding each aircraft with two nested bounding boxes. Collisions are detected when there exists any overlap between the boxes corresponding to any two aircraft.

Conflicts are resolved using a genetic algorithm that minimizes a cost function comprised of the length of the collision evasion path and any penalties for a collision. This method was successfully evaluated utilizing a homogeneous fleet of quadrotor UAS.

Rathbun and others approach the topic in a slightly different fashion.[51] They "seed" the path planning algorithm with an initial set of 20 random paths which are then mutated to produce 40 potential trajectories. These paths are mutated using two more operators than the method utilized by Conde in an attempt to avoid local minima. In an environment with dynamic obstacles, the seed, mutate, and search processes are repeated utilizing the previous solution as the initial seed for subsequent operations.

While genetic algorithms are capable of finding appropriate paths, in a highly dynamic environment, the computing time suffers due to the need to re-execute the mutation iteration process as the aircraft / obstacles move.

2.4.5 Geometric Methods

There are a number of so called "geometric methods" for detecting and resolving collisions between UAVs. In [52], a solution they call "vector sharing resolution" is proposed. Their methodology first detects collisions using the Point of Closest Approach (PCA) method described by Krozel [53]. Collisions are resolved by shifting the flight direction vector away from the region in which a collision would take place by moving along a shared vector. This shared vector is generated by first taking the cross product of the relative distance vector and the relative velocity unit vector. The cross product of the resulting vector and the relative velocity vector then yields the shared vector. The collision avoidance maneuvers proposed by Krozel, et.al. involves

one UAV modifying its heading along the positive shared vector direction and the other aircraft traversing along the negative shared vector direction with the goal of maximizing the minimum distance between any two aircraft.

Alternatively, geometric collision avoidance can be performed using a method known as *Velocity Obstacles*, or *Collision Cones*. This method, proposed in [54], consists of surrounding each vehicle and obstacle with an exclusion region. The collision cone method then transforms the geometry such that opposing obstacles are represented in the *velocity configuration space* of the host vehicle. This involves enlarging the obstacle's exclusion region by adding the host's exclusion region to it and representing the host vehicle as a single point. Tangent lines are then constructed between the point representing the host vehicle and the obstacle's enlarged exclusion region. If the relative velocity vector between the host vehicle and the obstacle falls between the tangent lines, a collision will occur. Collision evasion maneuvers therefore must push the relative velocity vectors outside the region containing the obstacle and bounded by the tangent lines.

The work done in this dissertation is based on the collision cone methodology. This is due to the relatively low computational requirements. This dissertation extends the collision cone concept by providing a means with which the identity of the opposing aircraft can be determined and the size of the exclusion region altered accordingly.

Chapter 3

RADAR Hardware

The hardware developed over the course of this research can be divided into two generations. The first generation hardware is used to demonstrate the feasibility of micro Doppler (spectral bands generated by vibration or rotation of the target's sub-components) identification of small (MTOW $<$ 10kg) UAS and to investigate some critical aspects of miniaturizing a RADAR system, e.g. signal to noise ratio, computing platforms, packaging, antenna design, etc... The second generation RADAR system improves upon the first generation hardware through the addition of range detection and azimuth scanning functions.

3.1 RADAR Design Considerations

There are a number of critical design decisions that must be made regarding the RADAR architecture. These decisions have a direct impact on operating parameters such as maximum range, minimum range, range resolution, power requirements,

required timing resolution, etc... This section will detail the critical design decisions and provide justifications for each.

3.1.1 Continuous Wave vs. Pulsed Operation

RADAR systems can generally be divided into two broad categories depending on the nature of the transmit energy: Pulsed, and Continuous Wave (CW). In a pulsed RADAR architecture, the transmitter generates RF pulses of a specified duration and transmits this energy towards the region under observation. These pulses then reflect off an object (if present) and a portion of the energy returns to the receive antenna. The range to the target object is determined by Equation 3.1.

$$R = \frac{cT}{2} \tag{3.1}$$

where the range, R, is defined in terms of the speed of light, c, and the elapsed time between the transmission of an individual pulse and its reception, T.

The rate at which these pulses are transmitted is referred to as the Pulse Repetition Frequency (PRF). In pulsed RADAR systems, any subsequent pulse must be transmitted after the arrival of the previous pulse. Failing to do so will lead to range ambiguities. Therefore, the PRF has a direct impact on the maximum distinguishable range (otherwise known as the unambiguous range), R_{unamb}, which is described by Equation 3.2.

$$R_{unamb} = \frac{c}{2(PRF)} \tag{3.2}$$

Pulsed RADARs are typically limited in the minimum detectable range as the receive circuitry is deactivated during the transmit pulse, since close range reflections

(i.e., high power reflections) would saturate and possibly destroy the highly sensitive receiver electronics. The lower bound on this minimum detectable range is defined by Equation 3.3

$$R_{min} = \frac{c(T_{tx} + T_{config})}{2} \tag{3.3}$$

where T_{tx} is the duration of the transmit pulse, and T_{config} is the time required to enable the receiver. Thus, for moderate pulse widths, the minimum detectable range can easily be in the region of tens of meters.

The range resolution of pulsed RADARs, ΔR_{min}, (in the absence of more advanced techniques, e.g. intra-pulse modulation, pulse compression, etc...) is shown in Equation 3.4

$$\Delta R_{min} = \frac{cT_{tx}}{2} \tag{3.4}$$

Given the equations above, a theoretical RADAR system with a minimum T_{tx} of 500 ns, a T_{config} of 11ns, and a PRF of 20kHz will have the properties described in Table 3.1.

Parameter	Value (meters)
Unambiguous Range	7494.8
Range Resolution	79.6
Minimum Range	74.9

Table 3.1: Example Pulsed RADAR performance

There are a large number of UAS with dimensions significantly smaller than the critical parameters: minimum range and range resolution. Furthermore, the design of a pulsed RADAR system with acceptably small minimum range and resolution

characteristics is prohibitively expensive. This is due to the high power needed during the short pulses, and the fast timing requirements of such a system.

Continuous Wave (CW) RADARs operate by continuously illuminating a target object with RF energy. Unlike pulsed RADAR systems, CW RADARs tend to operate using lower overall power levels (up to three magnitudes lower power for similar range performance [55]), and determine range to objects using some form of frequency modulation as opposed to pulse timing. This allows for simpler circuitry due to the elimination of tight timing requirements. Additionally, CW RADARs are capable of providing arbitrary range resolutions and no limit on the theoretical minimum range.

The simplest CW RADAR configuration, Doppler RADAR, broadcasts a continuous signal towards the area of interest. If an object is present in the area of interest, a portion of the transmit energy is reflected back towards the receiver where it is then down-converted (multiplied in the frequency domain) to produce the frequency of interest, otherwise known as the "beat frequency" or "Intermediate Frequency" (IF) and is described by Equation 3.5

$$F_{beat} = F_{tx} - F_{rx} \tag{3.5}$$

where F_{rx} is the frequency of the received signal, and F_{tx} is the frequency of the transmitted signal. F_{rx} is determined by the radial velocity v of the target object relative to the RADAR system (assuming co-located transmit and receive antennas). F_{rx} is generally defined by Equation 3.6.

$$F_{rx} = F_{tx}(\frac{1 + \frac{v}{c}}{1 - \frac{v}{c}}) \tag{3.6}$$

Simplifying 3.6 for terrestrial applications where generally, $v << c$, results in 3.7

$$F_{beat} \approx 2v\frac{F_{tx}}{c} \tag{3.7}$$

Unmodulated CW RADARs have no means to determine the range between the RADAR antenna and the target object. Furthermore, unmodulated CW RADARs are incapable of detecting stationery targets as F_{beat} results in a Direct Current (DC) signal which is lost due to the Alternating Current (AC) coupling between the RF front end and the amplifier stages. Furthermore, most CW RADAR front ends typically produce a DC signal regardless of the presence of a target due to leakage between the the receiver and transmitter.

Nevertheless, a number of methods exist for range measurement in CW RADARs and are generally divided into two categories: Frequency Modulated Continuous Wave (FMCW) and Stepped Frequency Continuous Wave (SFCW) (of which Frequency Shift Keyed Continuous Wave (FSKCW) is a narrowband subset). FMCW RADARs operate by modulating the transmit frequency, typically in a triangular fashion. Due to the finite speed of light, F_{tx} will be offset from F_{rx} by an amount proportional to the range. In general terms, the range between the RADAR antenna and the target object is defined by Equation 3.8

$$R = \frac{2cTF_{beat}}{BW} \tag{3.8}$$

where T is period of the frequency modulation and BW is the bandwidth. Unlike unmodulated CW RADARs, FMCW RADARs are capable of detecting both the presence and range of stationary targets. However, background clutter such as the terrain is also present in the output data.

FSKCW RADARs address this issue by replacing the linear, triangular modulation of FMCW RADARs with a square wave modulation of the transmit frequency. F_{beat} is then sampled synchronously with the modulation. The transmit frequency modulation combined with the synchronous sampling of the received signal effectively produces two unmodulated CW RADAR channels separated by a few MHz (BW): IF_A and IF_B. Equation 3.7 indicates that for any given moving target F_{beat} will be marginally different for IF_A and IF_B. This marginal difference in frequency appears the same when used for velocimetry purposes, but is fundamental for ranging as it manifests itself as a phase shift in the time domain. The range to the target object can then be inferred from the phase difference between IF_A and IF_B, see Equation 3.9 where ϕ_n is the phase of the IF_n [56].

$$Range = \frac{c(\phi_A - \phi_B)}{4\pi BW} \tag{3.9}$$

FSKCW RADARs offer the same benefits of other CW RADAR types namely: no minimum range and excellent range resolution, in addition to the benefits offered by unmodulated CW RADAR types (excellent ground clutter rejection and low overall transmit power requirements). However, the maximum practical range (in the absence of transmit power and receiver sensitivity limitations) is defined by the range corresponding to a 180° phase shift. As with pulsed RADAR systems, this range is defined as the unambiguous range and is described, in this case, by Equation 3.10 [56].

$$R_{unamb} = \frac{c}{2BW} \tag{3.10}$$

A comparison of the various CW RADAR types discussed in this section is shown in Table 3.2.

Parameter	Doppler	FMCW	FSKCW
Range Measurement	-	Yes	Yes
Velocity - Range Ambiguity	-	Yes	No
# of Receiver Channels	1	1	2
Bandwidth Requirements	Single Frequency	500MHz	5MHz
Modulation Type	-	Triangular or Sawtooth	Square

Table 3.2: CW RADAR Comparison

3.1.2 Transmit Frequency Selection

The transmit frequency, F_{tx} is selected based on a compromise between the following parameters: atmospheric absorption, ratio between the wavelength and the target object size, availability of components, desired range resolution, desired antenna size, and processing speed requirements of the intermediate frequency.

Atmospheric absorption of microwave frequencies, see Figure 3.1, plays a role in frequency selection since absorption increases dramatically as a function of frequency. Countering this effect requires a substantial increase in power and consequently the size of most RADAR components. A cursory examination of Figure 3.1 indicates that an X-Band RADAR system (center frequency 10.5 GHz) will have a round trip atmospheric absorption of 0.2dB/km while a comparable K-Band RADAR system (center frequency 24.0 GHz) will have an absorption figure of over 2dB/km. This effectively means that if all other system parameters are equal, then an X-Band RADAR system will have a range 10 times greater than a comparable K-Band RADAR. In practice, however, there are more contributing factors.

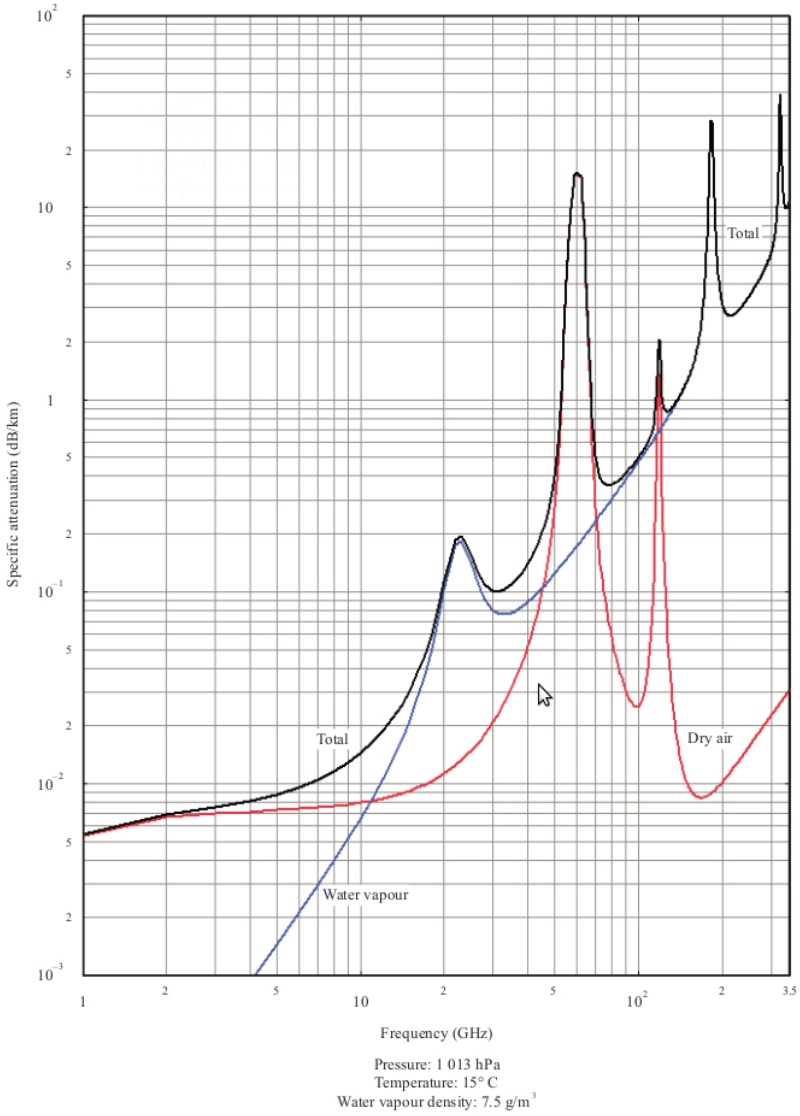

Figure 3.1: Atmospheric Absorption of RF Energy [2]

The ratio of the wavelength to the target object dimensions plays a role in the manner in which the target object scatters the incident radiation, see Figure 3.2 for details. The selection of higher frequencies increases the probability that any given target will fall within the optical scattering region. Within this region, the Radar

Cross Section (RCS) becomes well characterized and free from the RCS oscillations present in the Mie/Resonant scattering region.

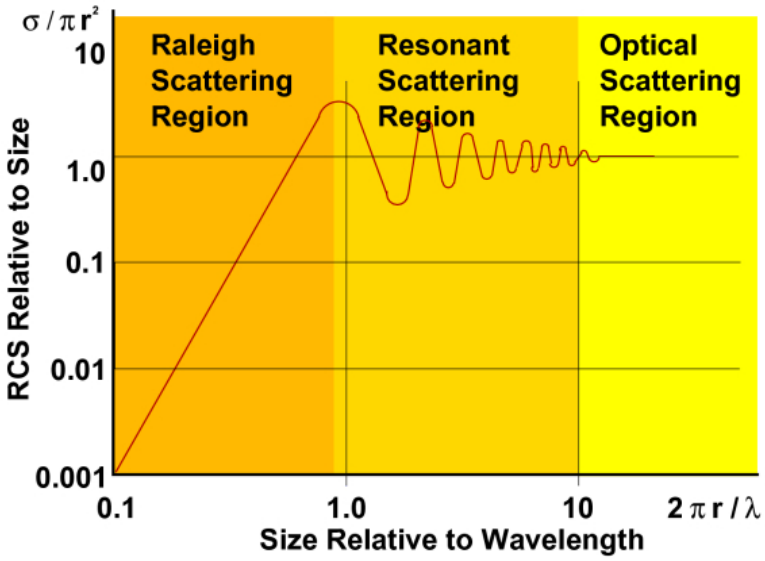

Figure 3.2: RCS vs Wavelength[3]

Transmit frequency selection also has a direct impact on the velocity resolution and data acquisition time. As characterized by Equation 3.7 the Doppler shift, F_{beat}, is directly proportional to F_{tx}. If F_{tx} increases, maintaining the same velocity resolution requires that the ADC sampling rate also increase by the same proportion. This has the effect of reducing the time required to acquire the relevant signal samples required for processing the RADAR data.

Microwave antennas sizes are also highly dependent on F_{tx}. A RADAR system designed for a mobile platform typically has limits placed on the amount of electrical power available and the overall volume and mass allocated to the RADAR payload. To reduce the required RF transmit power while maintaining the same range performance, an antenna with a narrow main lobe must be selected. However, to reduce

the size of the main lobe, the physical antenna size must increase. An example of this relationship (in the case of a parabolic antenna) is described by Equation 3.11.[57]

$$\Theta_{-3dB} = \frac{k\lambda}{diameter} \approx \frac{70\lambda}{d} \tag{3.11}$$

Where Θ_{-3dB} is the -3dB main lobe beam width, k is the steepness taper constant (typically 70 for parabolic antennas), λ is the operating wavelength, and d is the diameter of the antenna's reflector. Therefore, to achieve the same beamwidth, a RADAR operating at 10.5 GHz must have an antenna diameter approximately 2.3 times larger than a comparable RADAR operating at 24GHz.

3.2 Generation 1 RADAR Sensor

The first generation RADAR system developed for this dissertation, see Figure 3.3, is based on an X-Band (10.5GHz), unmodulated, continuous wave architecture. The hardware specifications are elucidated in Table 3.3.

System Mass	230 grams
System Dimensions	15.5 x 10 x 9 (cm)
Power Consumption	4.5 Watts
Input Voltage Range	10 to 15 VDC
RF Transmit Frequency	10.5 GHz
RF Transmit Power	10mW

Table 3.3: Generation 1 RADAR Hardware Specifications

The generation 1 RADAR system can be divided into several sub-components, see Figures 3.4 and 3.5. Figure 3.4 shows a selection of the key subcomponents (displayed clockwise from top): XMOS XC-1A processor development board, 10.5GHz Gunnplexer, analog filtering and amplification board, and finally the power condi-

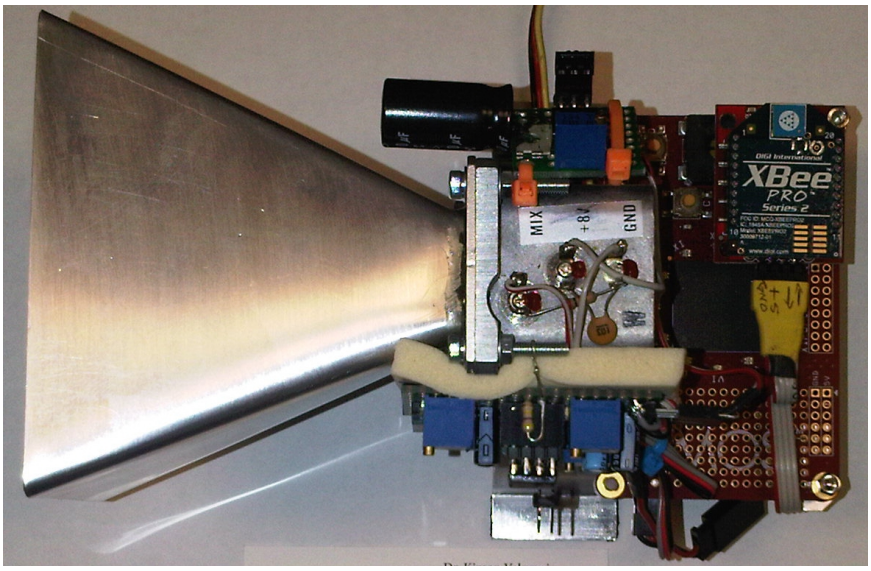

Figure 3.3: Complete Generation 1 RADAR System

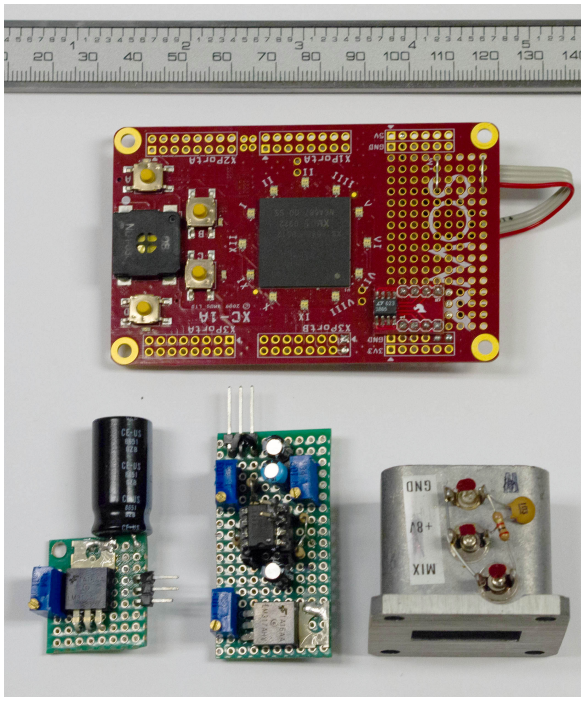

Figure 3.4: Generation 1 RADAR System Sub-Components

tioning circuitry while Figure 3.5 provides a block diagram describing how these components interact.

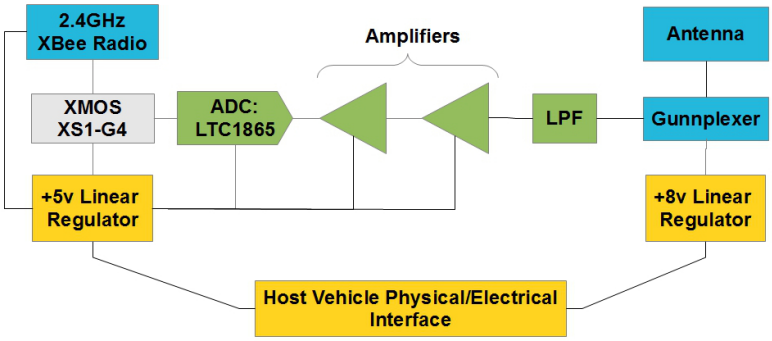

Figure 3.5: Generation 1 RADAR System Block Diagram

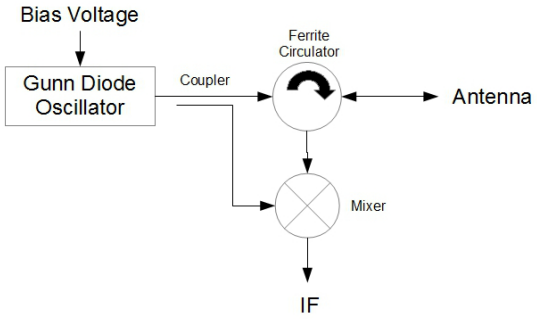

Figure 3.6: Gunnplexer Block Diagram

3.2.1 Generation 1 Microwave Section

The first generation prototype utilizes a Gunnplexer as the complete microwave front end, see Figure 3.4 The Gunnplexer used in this research consists of a Gunn diode mounted within a WR-90 size resonant waveguide cavity along with a ferrite circulator and a mixing diode.

The application of a DC bias voltage (in this case 8v) causes the Gunn diode to generate radiation at a wavelength stabilized by the dimensions of the resonant cavity. A portion of this energy is coupled to the mixing diode (located $\frac{\lambda}{4}$ wavelength

away from the Gunn diode) while the remainder of the power (10mW in this design) is directed to the antenna, which is mounted at the open end of the waveguide [58]. Signals that are reflected from targets within the radiation pattern of the antenna are then multiplied in the frequency domain by the mixer, thus, giving rise to a spectral output described by Equation 3.12.

$$F_{mixer} = n(F_{tx} - F_{rx}) + n(F_{tx} + F_{rx}) + (nF_{tx}) \tag{3.12}$$

Where $n = 1, 2, 3...$ and represents the n^{th} harmonics that result from the mixing process.

The frequency of interest however, is described by Equation 3.13 for $n = 1$ and it is essentially the lowest order harmonic of the signal originally described by Equation 3.5.

$$IF = n(F_{tx} - F_{rx}) \tag{3.13}$$

3.2.2 Generation 1 Antenna

The generation 1 prototype directs signals to and from the Gunnplexer by means of an antenna whose functions include: determining the transmit and receive radiation pattern and matching the impedance of the waveguide to the 377Ω impedance of free space. During development, numerous antenna designs were evaluated including: phased array patches, pyramidal horn, parabolic, yagi-uda, end-fire helical, and log periodic. The use of a Gunnplexer resulted in a pyramidal horn antenna being selected for the initial prototype. The antenna selection was driven by the following criteria:

Low Loss

To simplify fabrication the antenna-Gunnplexer coupling should be simple in order to reduce the possibility of impedance missmatches that would lead to power loss due to reflections. A pyramidal horn antenna couples microwaves directly to the Gunnplexer resonant cavity and avoids free space to coaxial/microstrip/stripline conversions.

High Gain

Horn antennas provide excellent directivity given their size and simplicity.

Low Mass

Horn antennas generally provide excellent performance with relatively low mass. There are a number of options for reducing the mass as horn antennas can be formed from nearly any base material, provided that a conductive layer thicker than the skin depth at the transmit frequency forms the primary geometry of the horn [59].

Horn antennas do have a number of drawbacks, however. On this scale, horn antennas have relatively high volumes compared to other antenna types (helical, paths, planar array, etc...). Furthermore, the shape of horn antennas are not aerodynamic and thus require a raydome. For the first generation prototype, volumetric and aerodynamic considerations are not paramount as RADAR testing takes place while the RADAR is ground-based and on board a hovering rotorcraft.

Selection of the antenna type provides the general framework for further design. However, as the RADAR system is designed for use on miniature UAS, there are a number of constraints on the antenna main lobe size.

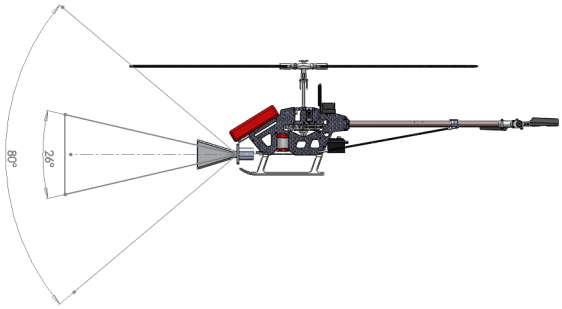

Figure 3.7: Interaction Between Vehicle Propulsion System and Antenna Main Lobe Angle

Figure 3.7 shows an example UAS with a possible RADAR antenna location and two main lobe angles: 26 ° and 80 °. The former represents an acceptable main lobe angle, while the latter should be avoided as the signal reflected from the host vehicle's propulsion system will most likely be substantially larger than the signals reflected from any targets of interest in the airspace. While the example in Figure 3.7 is greatly exaggerated, this antenna radiation pattern evaluation must be completed for each vehicle/antenna combination to ensure acceptable performance.

Once the desired antenna gain (and consequently the beam width) is determined, the antenna's critical dimensions are designed using the *Antenna Magus* software package. The critical dimensions are then used to create a CAD model in *Solidworks*. The CAD design is also verified against a CAD model of the host UAV to verify items such as mass distribution, antenna main lobe angles, potential antenna gimbal angles, etc...

Upon completion of the verification step, the CAD design of the antenna is then divided into two sections to ease fabrication. The first section consists of the WR-90 type waveguide flange, while the second consists of the pyramidal horn form. The flange was machined from aluminium while the pyramidal horn form was folded from

a single sheet of aluminium. The two were then joined with conductive adhesive and strengthened using epoxy. The final specifications of the generation 1 antenna are displayed in Table 3.4.

Material	Aluminium 6061-T6
Main Lobe Angle (-3dB)	26 Degrees
Gain	17dBi

Table 3.4: Generation 1 Horn Antenna Specifications

3.2.3 Generaton 1 Electronics

The generation 1 prototype analog electronics, see Figure 3.4, serve to condition the analog signal described by Equation 3.12 prior to digitization. The analog electronics can be broken down into several modules as follows:

DC-Block, and 1st Stage LPF

As Equation 3.12 describes, in particular the IF term, $n(F_{tx} - F_{rx})$, there exists a DC value corresponding to the portion of the transmit signal that returns to the Gunnplexer without a Doppler frequency shift. In practice, this is approximately 20mV. However, this DC bias must be removed prior to amplification to prevent saturation of the output. Equation 3.12 also describes higher order terms and the portions of the transmit and receive frequencies that are present in the mixer output. These higher order terms must also be removed prior to amplification. Failing to do so (given the final sampling rate) will introduce noise in the system.

1st Stage Amplifier

The 1st stage amplifier serves to increase the apparent input impedance to the

system and provide the initial gain to prevent excessive signal loss prior to the subsequent filtering. The gain of this stage is relatively low, approximately $11\frac{v}{v}$.

2nd Stage BPF, and 2nd Stage Amplifier

The final analog stage consists of a Band Pass Filter (BPF) and the main gain stage. The BPF is necessary to prevent the small DC offset of the 1st stage from saturating the amplifier output. Additionally the BPF serves to increase the attenuation of the higher order mixer terms. The 2nd stage amplifier then provides the bulk of the overall gain ($6267\frac{v}{v}$). When combined with the 1st stage, the overall gain becomes $68,937\frac{v}{v}$ ($96.77dB$). Saturation of the analog section is tolerated due to the fixed analog gain and the limited dynamic range of the analog section. Subsequent filtering in DSP addresses the clipping exhibited by a strong return signal.

In an effort to reduce the effects of noise by shortening cable lengths, the analog electronics are mounted directly to the Gunnplexer. This results in a combined microwave/analog section mass of 137 grams (compared with an all up mass of 230 grams.

The exceptional lightweight and identification capabilities (described in Section 4.3) provided grounds for pursuing intellectual property rights to the technology developed for the RADAR up to this point. As a result, the generation 1 hardware and software arrangement is protected under United States provisional patent number 61/478,681.

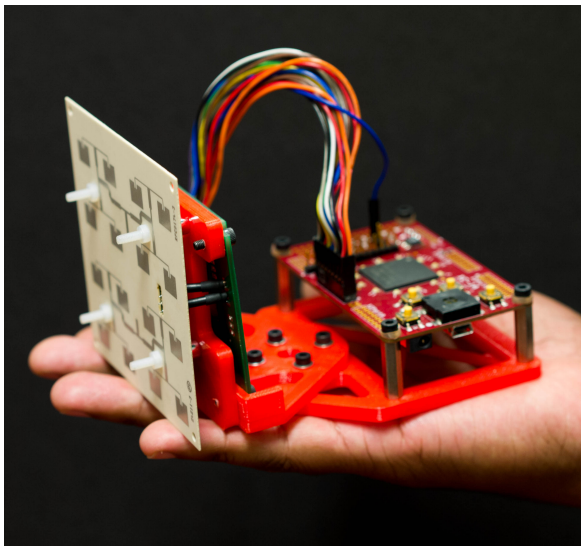

Figure 3.8: Generation 2 RADAR sensor

3.3 Generation 2 RADAR Sensor

The second generation RADAR prototype, see Figure 3.8, makes several of significant improvements over the first generation with the most important improvement being the addition of FSKCW range detection. Other important improvements include the addition of variable gain amplifiers to expand the dynamic range of the analog section, variable cut-off frequency filters to facilitate a wide range of target velocities, and improved noise rejection due to revisions in the analog section layout. The specifications of the complete generation 2 RADAR sensor are shown in Table 3.5.

3.3.1 Generation 2 Microwave Section

The microwave section of the generation 2 RADAR sensor is comprised of a commercially available, FSKCW microwave front end and antenna module (Microwave Associates MDU4210) [6]. This module is based on a Dielectric Resonant Oscillator

System Mass	150 grams
System Dimensions	10 x 10 x 10 (cm)
Power Consumption	4.5 Watts
Input Voltage	5 to 6 VDC
Transmit Frequency	10.587 GHz
Transmit Bandwidth	5MHz
Transmit Power	0.4mW

Table 3.5: Generation 2 Specifications

(DRO) and is electronically tunable using a Varactor diode. In many commercial applications, these modules are used for motor vehicle traffic detection.

3.3.2 Generation 2 Analog Section

The generation 2 analog electronics, see Figure 3.9, is comprised of three separate printed circuit boards of two categories: signal switching, and signal amplification as shown in Figures 3.11, and 3.10, respectively.

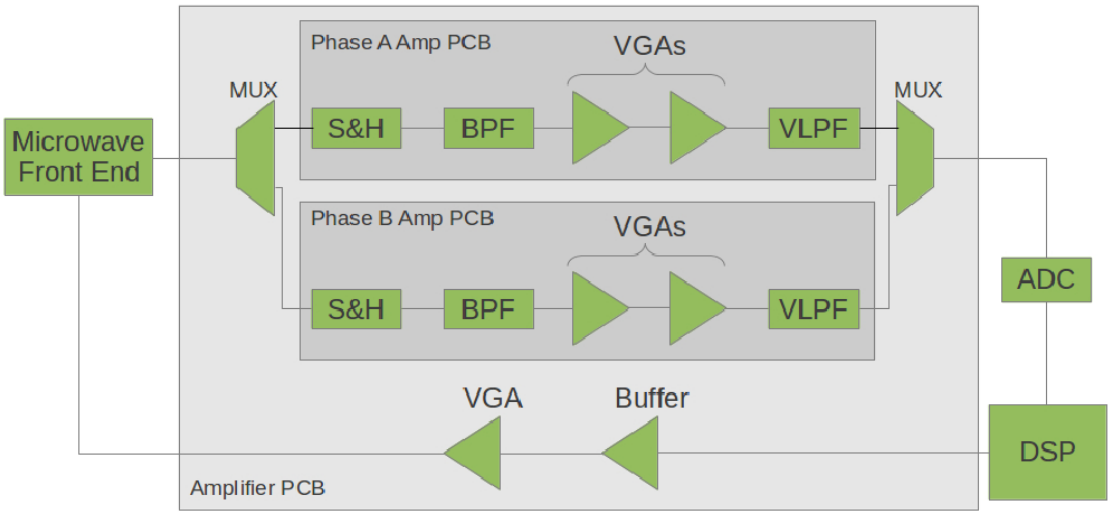

Figure 3.9: Generation 2 Electronics Block Diagram

Since FSK modulation requires rapid switching between two adjacent frequencies (typically separated by less than 5 MHz) two amplifier trains are required due to the finite bandwidth of the electronics. These amplification chains (located on separate PCBs to aid in serviceability and cross-talk reduction) function as follows: The RADAR IF signal first passes through a bandpass filter to strip away the higher order mixing harmonics and the DC offset. The relatively weak IF signal is amplified by an operational amplifier-based non-inverting amplifier with a digital potentiometer feedback element. The output of this amplifier is AC coupled with another identical variable gain amplifier. This output signal is then passed through a variable cutoff frequency low pass filter tuned by a digital potentiometer.

The amplifier topology was evaluated in LTSpice IV to determine gain and phase characteristics. The simulated circuit is shown in Figure 3.12 while the simulation results are shown in Figure 3.13. The PCB layout was designed in Eagle CAD 6.2.0 and the production schematics for the amplifier and multiplexing boards are shown in Figures 3.15 and 3.14.

3.4 Generation 2a RADAR Sensor

Up to this point, the hardware described, generations 1 and 2, is capable of obtaining target information while the target is within the antenna main lobe which is fixed relative to the RADAR sensor. The fixed main lobe of the first two generations is problematic since they are not able to scan an area to provide a wider field of view. More importantly, they are not able to provide information regarding the relative bearing of any objects of interest.

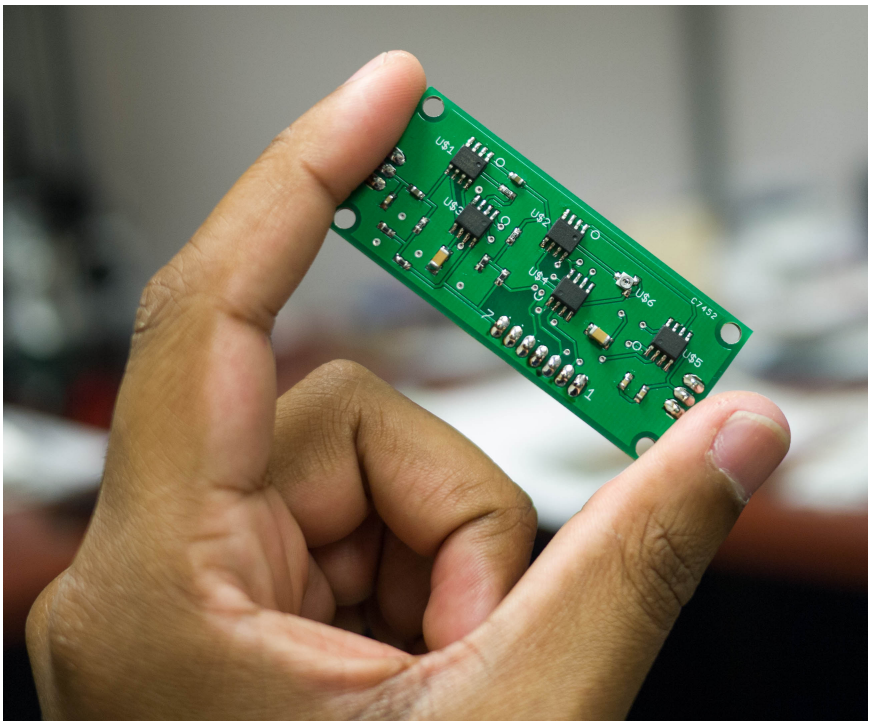

Figure 3.10: Generation 2 Analog Processing Board

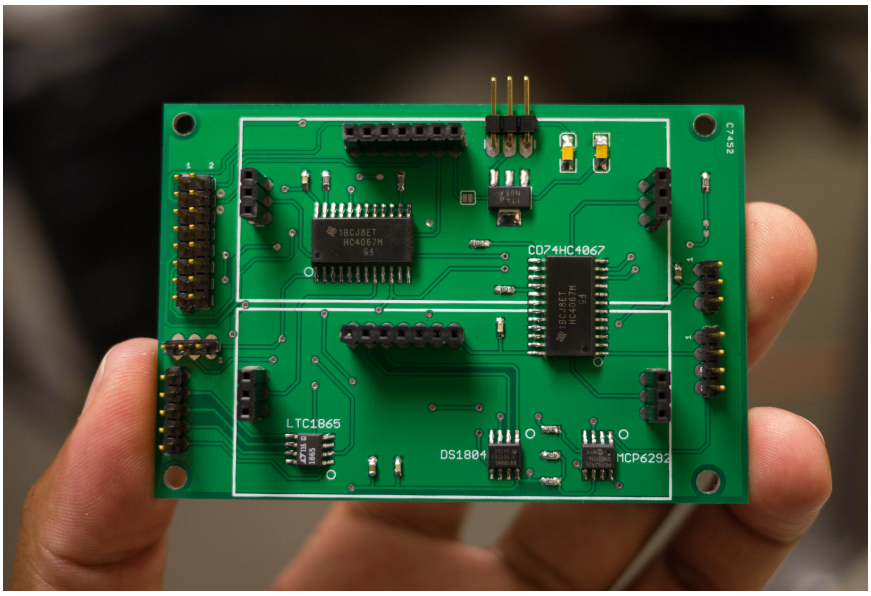

Figure 3.11: Generation 2 Multiplexing Board

There are a number of popular methods for obtaining target bearing information using RADAR systems including: electronic beam steering, monopulse, interferometry, mechanical scanning, etc... Electronic beam steering, see Figure **??** utilizes an array of emitters with variable phase shifters to electronically vary the direction of the antenna main lobe. While there are a variety of methods that can be used to accomplish this, electronic beam steering is typically the most complex and most expensive solution for obtaining relative bearing information on RADAR targets [4].

The second method, Amplitude Comparison Monopulse (ACM) RADAR, is constructed using between 2 and 4 receive antennas arranged in a row for single axis measurement or quadrant for dual axis measurement, respectively. The target bearing information manifests as a difference in received signal strength in the antenna array. ACM RADAR types can obtain very accurate relative bearing information, but typically have limited observation angles due to high antenna gain. Therefore, ACM RADARs are most often used to track targets which have already been acquired with a search RADAR. The third method, Phase Comparison Monopulse (PCM), is similar to the ACM architecture in that it requires an array of receive antennas. However, while ACM measures the difference in received signal strength, PCM RADARs measure the phase shift caused by the difference in the free space path length between the antenna array elements and the target of interest. Larger off-boresight angles increases the difference in the path length. A diagram of the PCM RADAR operation is shown in Figure 3.17 [4].

The final method, mechanical scanning, is when the entire antenna system is mechanically rotated throughout the observation angles in order to obtain target bearing information. Mechanical scanning may be used in combination with any of the above methods or may be used by itself. The primary disadvantage is the increased time

required to obtain target bearing information. An additional disadvantage is the addition of a moving component (the antenna, and the antenna gimbal/servo assembly). However, mechanical scanning allows the RADAR hardware developed during this research to be utilized without completely re-designing the antenna, microwave, electronic, and software components. Mechanical scanning has an additional advantage in that narrow-beam (and consequently high gain) antennas can be used without decreasing the sensor's field of regard as would be necessary using interferometry or monopulse architectures.

Given the above, mechanical scanning is used throughout this research for obtaining target azimuth information. The result is the generation 2a hardware shown in Figures 3.18 and 3.19. The antenna, microwave, and computing hardware of the generation 2a RADAR sensor is identical to the generation 2 hardware. The only addition being the mechanical components and electrical modifications required for mechanical scanning.

Mechanical scanning is accomplished by first separating the XMOS processor board (XMOS XC-1a) from the antenna, microwave, and analog components. This reduces the reciprocating mass by 50 grams and improves antenna pointing agility. Additional benefits include the physical separation of the high gain electronics from the high frequency digital signals present on the XC-1a board.

The antenna, microwave, and analog components are then mounted on a plastic structure (henceforth refereed to as the antenna mount) which provides mechanical stability and maintains the relative positions of the aforementioned components. This plastic structure is then directly attached (using two M3 screws) to a Hobbico CS-80 servo [60] which serves to physically rotate the antenna mount through a 90°

range in as little as 0.29 seconds. The addition of the servo increases the overall sensor mass by 150 grams and the total power consumption by 1.3 Watts.

As with most Radio Control (RC) type servos, the position feedback in the CS-80 is internal to the servo and users provide position commands to the servo using Pulse Position Modulation (PPM) signals with no feedback regarding the servo's actual position. Allowing the RADAR processor to monitor the position of the servo using the servo's own position encoder eliminates the need for an additional, external antenna position encoder and reduces the system complexity and overall mass. The CS-80 servo, as with most RC servos, utilizes a potentiometer directly coupled to its mechanical output shaft. The potentiometer is configured in such a way to produce an analog voltage directly proportional to the physical position of the shaft. Extracting this signal involves drilling a hole through the servo case then routing a wire from the potentiometer's wiper to the RADAR processor's Analog to Digital Converter (ADC). The 16-bit LTC1865 ADC used in this research has a voltage resolution of $76\mu V$ which results in an antenna position resolution of $0.01°$.

3.5 Remarks

In this chapter, two generations of prototype RADAR sensors are described. A comparison of the two generations is shown in Table 3.6.

The first generation prototype is constructed utilizing waveguide technology and operates purely in the Doppler mode (i.e. without modulation of the transmit frequency) and is therefore incapable of determining the range to any objects of interest. Nevertheless, the first generation is of great utility in that measurements of an object's micro Doppler signature can be obtained using the Doppler operating mode.

Generation	1	2	2a
Mass (g)	250	150	360
Dimensions (cm)	15.5x10x9	10x10x10	13x10x17.5
Power Consumption (W)	4.5	4.5	5.8
Input Voltage (VDC)	10-15	5-6	5-6
Transmit Frequency (GHz)	10.5	10.5	10.5
Transmit Bandwidth (MHz)	-	5MHz	5MHz
Transmit Power (mW)	10	0.4	0.4
Modulation	-	FSKCW	FSKCW

Table 3.6: RADAR Prototype Comparison

The second generation of RADAR sensors (generations 2 and 2a) support the original operating modes of the first generation and improve upon it in three important ways: range measurement, variable gain amplifiers, and azimuth measurement in the 2a version. The next chapter provides more information on the origin of the micro Doppler signals that allow for identification, in addition to the software methods utilized in conjunction with the various RADAR sensor generations. Finally, the RADAR sensors are be evaluated using rotorcraft and mobile vehicles equipped with RADAR reflectors.

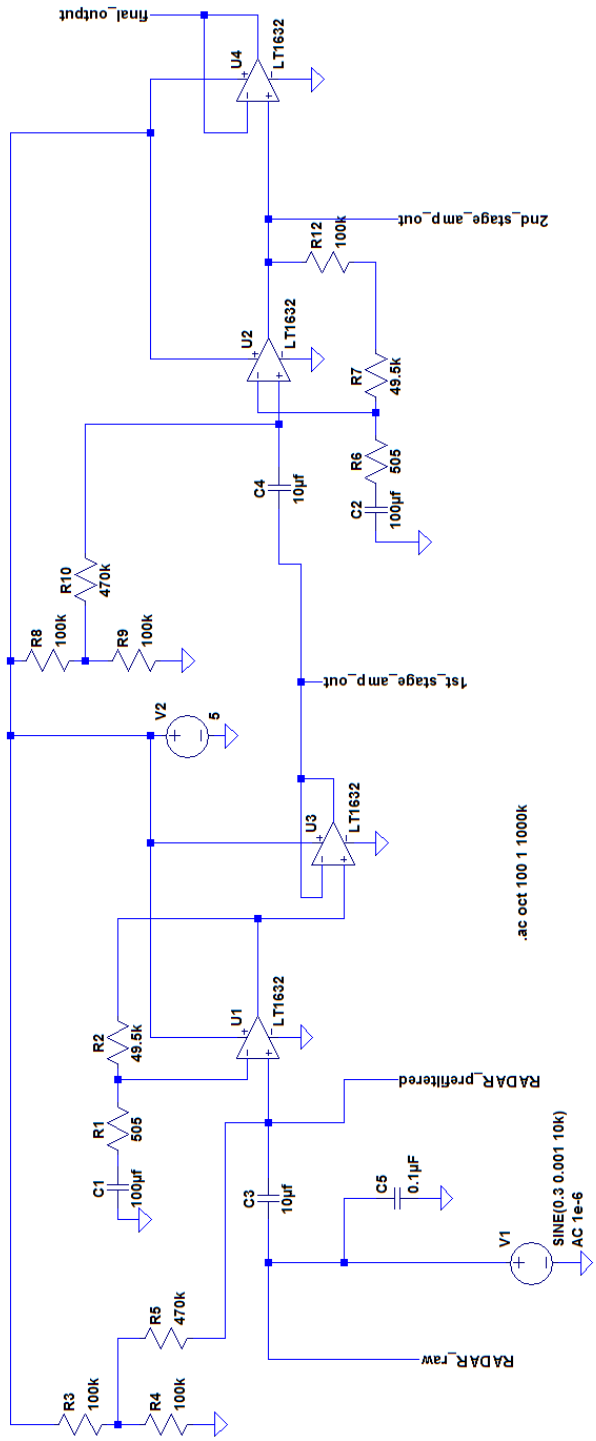

Figure 3.12: Generation 2 IF Amplifier Simulation Schematic (Maximum Gain Configuration)

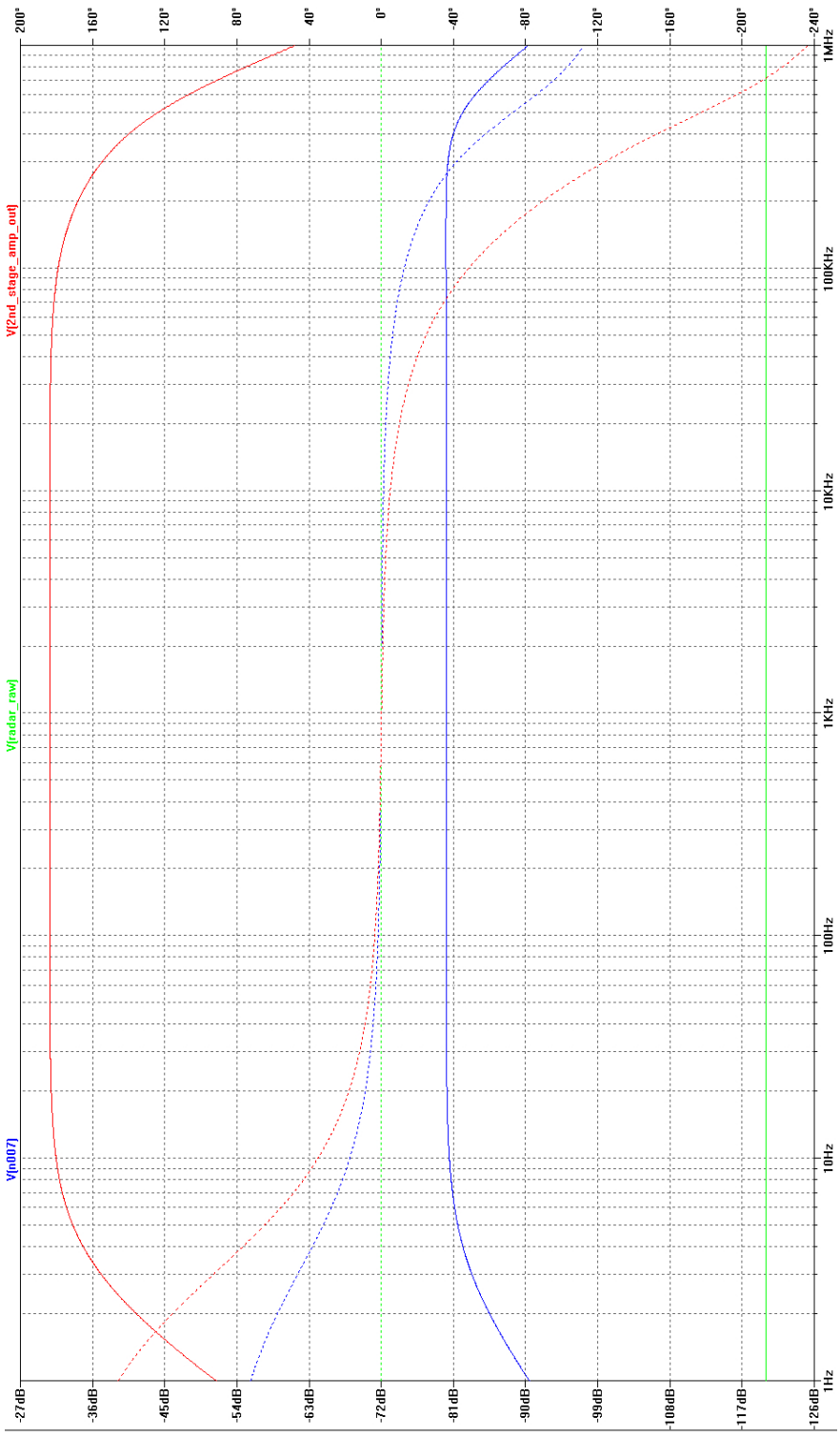

Figure 3.13: Generation 2 IF Amplifier Gain and Phase

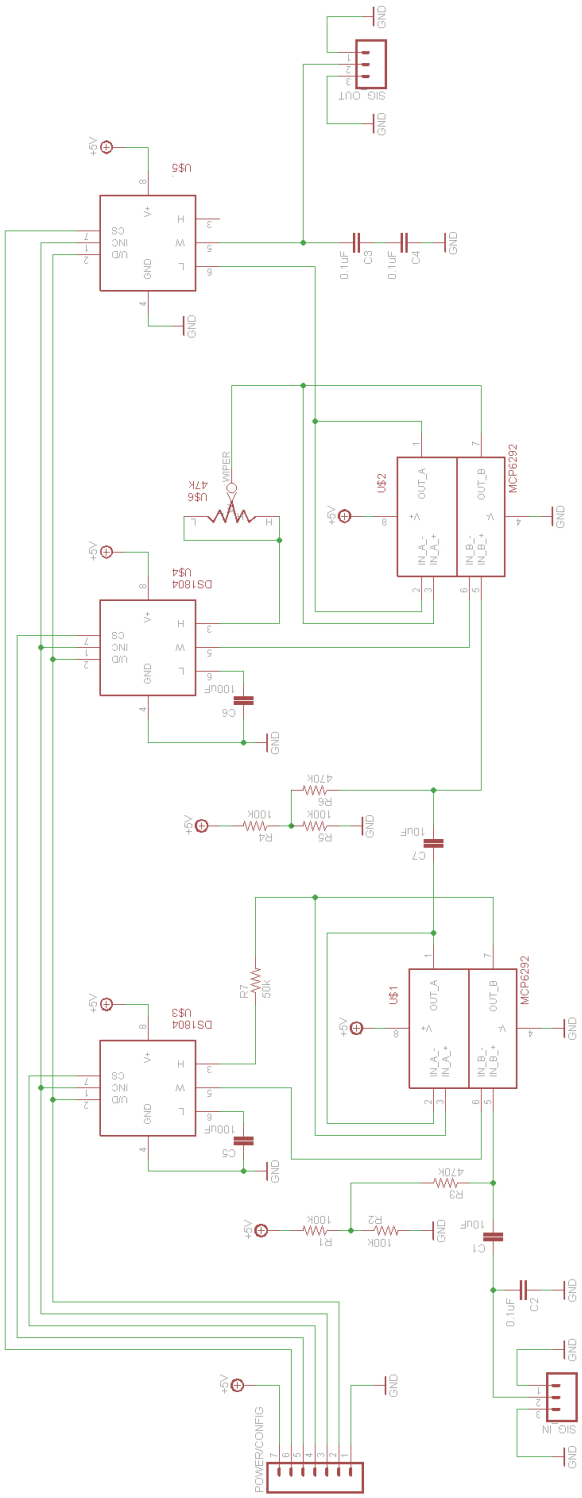

Figure 3.14: Generation 2 IF Amplifier PCB Schematic

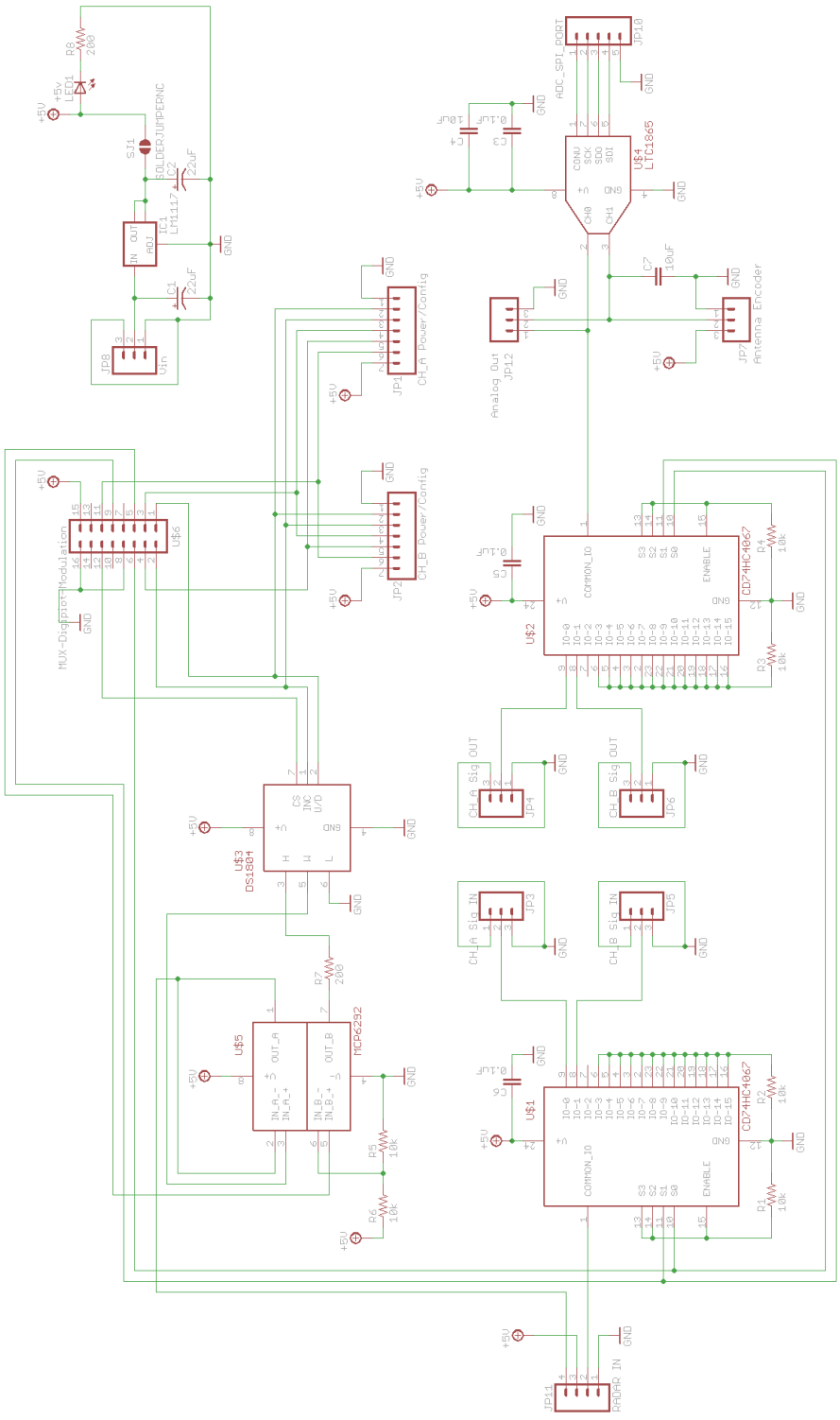

Figure 3.15: Generation 2 Multiplexer PCB Schematic

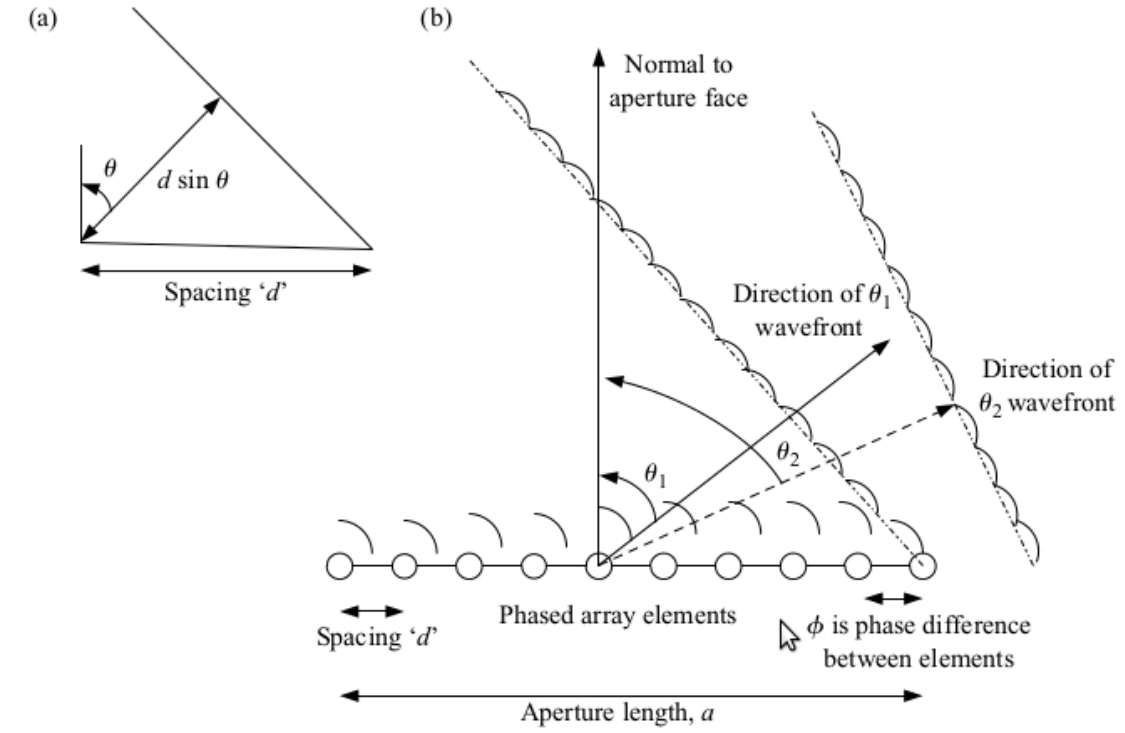

Figure 3.16: Phased Array Diagram [4]

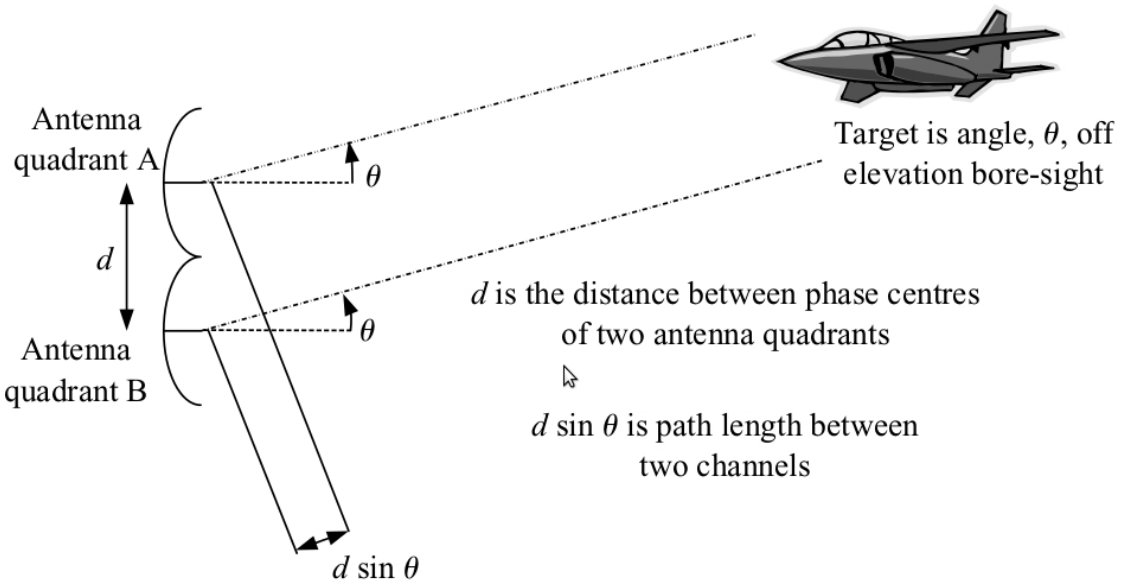

Figure 3.17: Phase Comparison Monopulse Diagram [4]

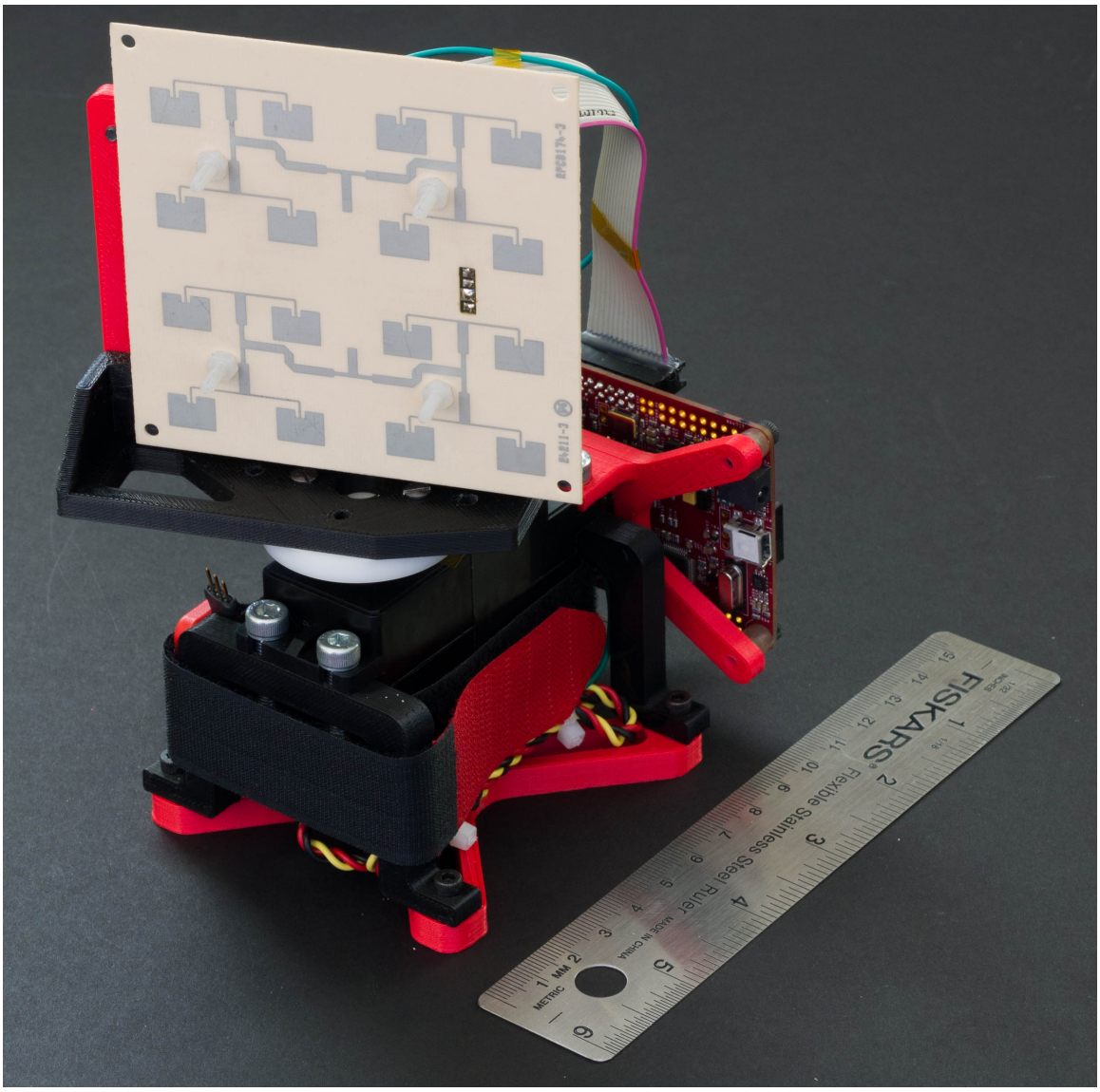

Figure 3.18: Generation 2a RADAR Sensor Front View (with a 6" (15.2cm) size reference)

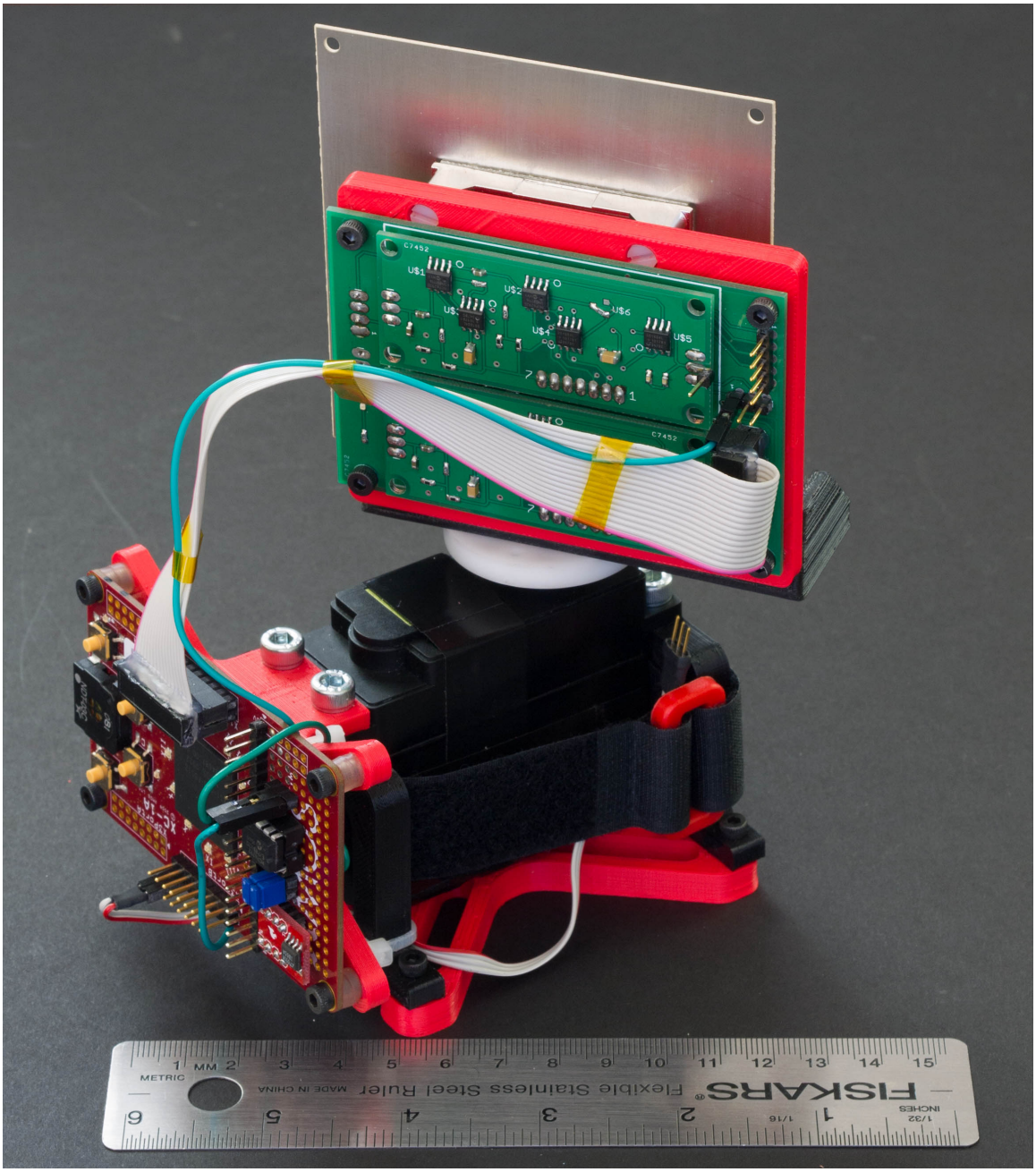

Figure 3.19: Generation 2a RADAR Sensor Rear View (with 6” (15.2cm) size reference)

Chapter 4

Rotorcraft Modeling and Experimental Evaluation

One of the goals of this research is to demonstrate that UAVs can be differentiated from each other with an acceptable degree of certainty based solely on their RADAR signatures. While not strictly required for all collision avoidance methods the collision avoidance algorithm described in chapter 5 utilizes this information to determine an appropriate avoidance maneuver. This chapter aims to describe the origin of micro Doppler signatures and present experimental results to verify the practicality of such identification. Additionally, experimental results

4.1 Origin of Unique RADAR Signatures

The monostatic, subluminal case of the Doppler effect as described in Section 3.1.1 may be applied to more complex targets wherein the output spectra is the superposition of the Doppler shifts of the individual moving parts. The Doppler shifts

of these individual moving parts can be considered to be a continuous frequency distribution between the slowest and fastest sections of the component (this arrangement is typically encountered in rotating machinery wherein the section of the object closest to the rotational axis traverses space slower than the sections further from the axis). However, for the sake of simplicity, this example shall only consider the peak frequencies.

A typical aircraft consists of a number of rotating components, which are usually found within the propulsion system, e.g., turbine blades, propellers, rotor systems, fans, etc... One of the essential assumptions of this work is that the variation between different aircraft types (and occasionally even variations within a single aircraft type) are sufficient to enable practical and reliable identification based solely on the micro Doppler signature. This is a reasonable assumption since it is unlikely that different UAVs (with similar flight characteristics) will utilize identical drive systems, e.g., identical rotor/propeller diameters, rotor/propeller rotation rates, main/tail rotor gear ratios, etc...

An application of the single point micro Doppler target approach to the rotation components of a typical miniature (900g flying weight, 715mm main rotor diameter) helicopter system such as the one in Figure 4.1 results in the peak spectral content as described by Equation 4.1.

Figure 4.1: Align TRex450 Helicopter

$$Spectrum_{peak}(T) = \left(\frac{2F_{tx}}{c}\right)\left[\frac{\pi d_{mr}}{T} + \frac{\pi d_p}{T} + \frac{\pi d_{tr}}{T/\delta} + Aux(T)\right] \tag{4.1}$$

Where T is the rotational period of the main rotor, d_{mr} d_p and d_{tr} are the diameters of the main rotor, stabilizing paddles, and tail rotor respectively, δ represents the gear ratio between the main and tail rotor (which in this case is 4.24), and $Aux(T)$, which represents rotating components with smaller RCS than the aforementioned components.

It is important to note that while it is possible to calculate the spectral lines for any given propulsion system, doing so is largely impractical (due to the wide variation in UAS types) and unnecessary for identification. Rather, a training-based approach is used in this dissertation wherein the algorithms focus on identifying aircraft using *a priori* knowledge of the frequency domain signature.

4.2 Blade RCS and Identification Range Limit

Given that the ability to identify aircraft based on its micro Doppler signature depends on the RCS of the rotating components, the practical range limit for identification (as opposed to detection) can be determined by measuring the RCS of the identifying structures. Calculating the RCS for any practical aerodynamic structure can be challenging. However, a simplified model of helicopter rotors is available in the literature, see Equation 4.2 [29].

$$\sigma = \left(\frac{4\pi L^2 H^2}{\lambda^2}\right)\left(\frac{\sin(\frac{2\pi}{\lambda})\sin\theta}{(\frac{2\pi}{\lambda})L\sin\theta}\right)^2 \cos^2\theta \tag{4.2}$$

Where σ, λ, H, L, and θ are the RCS, RADAR wavelength, blade thickness, length, and incident angle, respectively. Equation 4.2 models the blades as metalic ribbons with the above parameters, but in reality, many small scale aircraft have plastic, or composite rotor blades, which may not necessarily be efficient RADAR reflectors. Depending on the material used and assuming a single reflection geometry, one can use the reflection coefficient Γ to scale the results of Equation 4.2 as shown in 4.3 to account for the incomplete reflections at the blade-air interface, where Γ is the reflection coefficient as described in Equation 4.4, Z_B and Z_A are the characteristic impedances of the blade material (unknown), and air (377Ω), respectively.

$$\sigma = \left(\frac{4\pi L^2 H^2 \Gamma}{\lambda^2}\right)\left(\frac{\sin(\frac{2\pi}{\lambda})\sin\theta}{(\frac{2\pi}{\lambda})L\sin\theta}\right)^2 \cos^2\theta \tag{4.3}$$

$$\Gamma = \frac{Z_B - Z_A}{Z_B + Z_A} \tag{4.4}$$

Throughout this dissertation, it will be assumed that the rotorcraft blades are of a ribbon geometry and are made from a conductive material thereby setting $|\Gamma| = 1$ The main rotor RCS for a number of small scale aircraft ranging from the Trex 250 (0.45 meter rotor diameter) to the Maxi Joker (1.8 meter rotor diameter) is displayed in Table 4.1.

Vehicle	L (m)	H (m)	Blades	RCS Each (m^2)	RCS Flash Max(m^2)
Trex 250	0.20	0.003	2	0.0003	0.0060
Trex 450	0.32	0.005	2	0.0213	0.0426
Lama v4	0.15	0.004	4	0.0092	0.0367
Arducopter	0.12	0.008	8	0.0077	0.0614
Maxi Joker II	0.81	0.010	2	0.5465	1.0929

Table 4.1: Main Rotor RCS

The monostatic RADAR range equation, see Equation 4.5, can be used to calculate the identification ranges for various aircraft (based solely on the main rotor micro Doppler signature) where P_r is the received power, G_t is the gain of the antenna, A_r is the effective aperture, σ is the RCS, F is the pattern propagation factor, and R is the range to the target [29].

$$P_r = \frac{P_t G_t A_r \sigma F^4}{(4\pi)^2 R^4} \tag{4.5}$$

Utilizing the generation 2 RADAR system specifications, the identification ranges for the vehicles shown in Table 4.1, can be determined. The results are presented in Table 4.2. However, it should be noted that the detection ranges in practice will be much lower due to a number of factors but mainly due to problems of geometry and the fact that $|\Gamma| \neq 1$

Vehicle	Maximum Identification Range (m)
Trex 250	7.89
Trex 450	12.88
Lama v4	12.48
Arducopter	14.11
Maxi Joker II	28.98

Table 4.2: Main Rotor Identification Range with Gen 2 RADAR (Theoretical)

4.3 Micro Doppler Signal Acquisition And Identification

The on-board processing software for the micro Doppler identification mode is composed of several discrete modules, see Figure 4.2. The architecture of the XMOS processor used in this research allows software to be cleanly organized as different

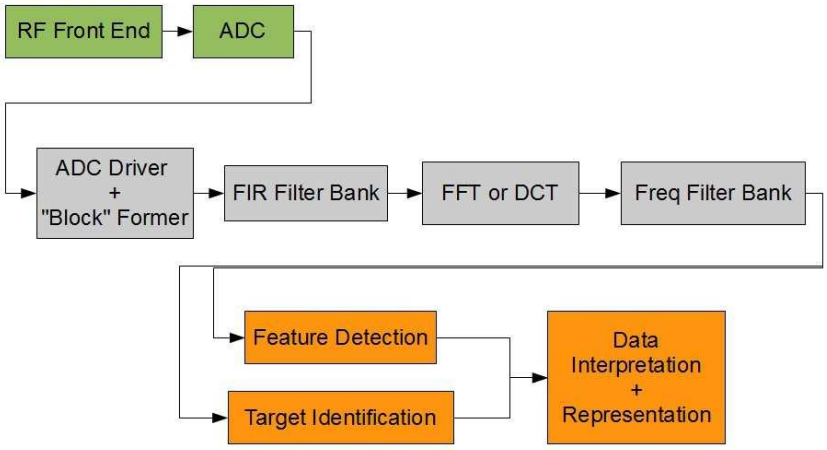

Figure 4.2: Target Identification Data Flow

tasks with high-performance (3.2 Gbps) communication channels between them. In Figure 4.2, the first two (green) rectangles represent the hardware modules described in Chapter 3. The rectangles in the remaining rows are implemented on the XMOS processor as tasks, with the arrows between them representing unidirectional data channels. The use of channels for inter-task communication obviates the need for sophisticated (and error prone) synchronization to protect shared global memory, and allows for each task to perform blocking I/O on the ports or channels it is concerned with, again resulting in clean, well-organized software. Each module is executed, in parallel, as a distinct task.

The in-hardware scheduler on the XMOS ensures that all tasks are scheduled fairly and with great regularity (round-robin among the active tasks for a single instruction). The ADC Driver module samples the ADC continuously and generates data packets that are forwarded to the other modules. While the size of the data packets is variable as a function of the desired frequency resolution and velocity range, for the prototype, a fixed size of 512 samples per data packet is used. The

second module consists of a set of FIR filters. These filters serve to eliminate variable noise that is not attenuated by the IF amplifier module. This approach is particularly effective as digital filters can provide steep rolloff rates, and can be implemented within the XMOS as dictated by application requirements. For example, if the UAV is operating near power lines, a 60Hz FIR notch filter can be introduced to enable successful operation. The third module consists of a Fast Fourier Transform (FFT) operation which serves to convert the time domain signals from the previous operations into frequency domain signals. The fourth module is an additional digital filter block used to filter the frequency domain signal representation. This filtering is used to eliminate erroneous target information and increases the reliability and simplicity of subsequent processing blocks (feature detection and target identification). The result of these first four software modules depicted in Figure 4.2 is a 256-sample frequency-domain signature (the bottom 256 samples from the FFT are discarded as they are simply a mirror of the ones utilized by the algorithm). This signature is now ready for use in target detection and identification.

Examination of Figure 4.4 shows that the majority of signal energy is present in the lower frequencies. While the signals generated by the down-conversion process bear higher frequency components, these higher frequencies are filtered by the IF amplifier module leaving their lower frequency harmonics. This characteristic of the system is advantageous in that it can be used to determine the velocity of the target relative to the RADAR. This is achieved by reducing the number of samples that comprise a signature from 256, and sliding this truncated target signature along the 256-sample scene signature, determining the match quality at each point. If the best match occurs at a non-zero offset, then the target bears a radial velocity corresponding to the offset. This process is shown in Figure 4.3

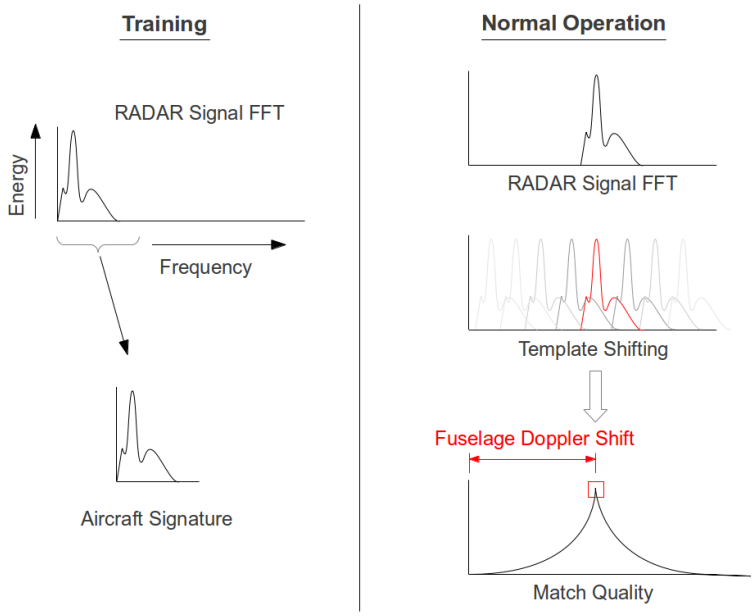

Figure 4.3: Target Identification and Velocimetry Process

In order to detect the presence of a target of interest, one must be able to differentiate a given signature from the background scene within the range of the RADAR. In order to identify different targets, it must be determined that a given signature matches one from a database of prerecorded signatures of vehicle classes of interest. Fundamentally, both of these operations involve comparing a given live signature, with a library of prerecorded signatures and determining which is the best match. Both the background signature and vehicle signatures are represented within this signature library, and are, then, able to perform detection and identification in the same computational step (i.e., if the live signature matches the background signature the best, then there is no target of interest within range).

This approach is utilized to great effect during the static tests wherein the RADAR itself is motionless. Dynamic testing is somewhat more complicated with

the RADAR requiring more information regarding the pointing direction and the host aircraft's velocity. This information is utilized to determine an appropriate background signal profile. This background signal profile consists of the clutter expected due to the Doppler shift corresponding to the host vehicle's motion including main and side-lobe observations.

As described above, one of the fundamental computational operations performed by the RADAR system is to match an incoming live signature against a library of prerecorded vehicle signatures. In order to evaluate different algorithms efficiently, the data collection mode of the RADAR is utilized to record 160, 256-sample signatures for the three vehicles whose signatures are depicted in Figure 4.4. During development, a simple user interface to the RADAR is implemented over a bi-directional serial link that enables it to operate in either data collection mode or target matching mode. In the first, the data collection mode is used to gather a large number of live samples of different vehicles in order to evaluate different matching algorithms offline. The second evaluation performed is to determine whether the RADAR system can successfully implement the matching logic on board in a real-time scenario with live targets.

For these experiments, the RADAR system and target vehicles are placed inside a reinforced concrete room. Throughout the experiments, the range between the RADAR system and target vehicles is fixed at 3 meters (10 feet). The linear separation distance between each vehicle was 0.6m resulting in an angular separation of 11.31°, see Figure 4.5.

No effort was made to reduce or account for multi-path signals or reflections from the background. The vehicle signatures are recorded by fixing the vehicle to the floor of the test room and throttling the rotor system to typical flight speeds.

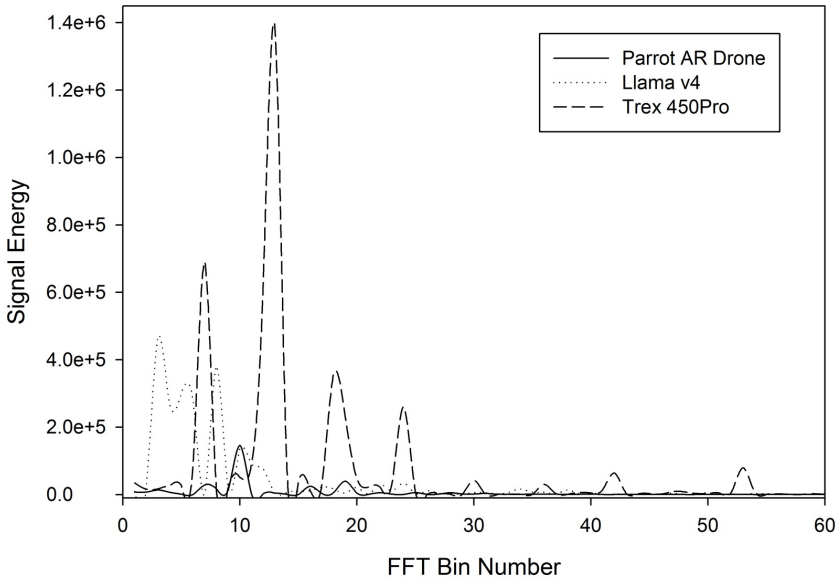

Figure 4.4: Miniature Rotorcraft Micro Doppler Signatures

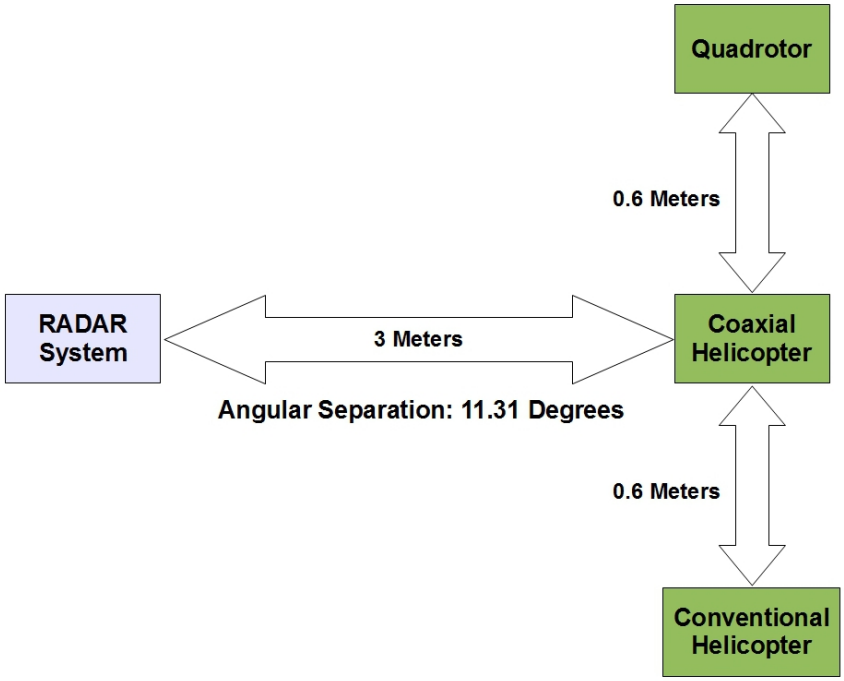

Figure 4.5: Micro Doppler Identification Validation Setup

The RADAR system is then pointed at the target vehicle and a series of signatures are streamed back to the attendant PC over the dedicated (wired) serial link; 160 of these signatures are gathered per vehicle and saved into a log file. Due to the presence of noise in the signatures, a filtered signature is generated by averaging a varying number of raw signatures into a library signature, using a simple arithmetic average per sample position. For example, when averaging 10 signatures, all 10 values in the first of 256 buckets is combined to give the average value for the first bucket. For each such library signature, a comparison is made between it and all other signatures created by averaging the same number of raw signals across the three vehicles. Identification is performed by calculating the best match across all vehicles using the algorithms described below. If the best match comes from the correct vehicle, it is counted as a successful match.

Each algorithm computes a single match value when executed on a library signature and live signature pair. The vehicle corresponding to the library signature that exhibits the best match with the live signature is selected. The following simple algorithms were evaluated.

Sum of Absolute Differences (SAD)

The total difference between the two signatures is calculated by adding the absolute value of differences between the 256 samples. The match with the smallest total difference is taken as best.

Sum of Squared Differences (SSD)

The total difference between the two signatures is calculated by adding the square of differences between the 256 samples. The match with the smallest total difference is taken as best.

Euclidean Distance (ED)

The total distance between the two signatures is calculated by taking the square root of the sum of squared differences. The match with the smallest total difference is taken as best.

Correlation (C)

The correlation between the two signatures is calculated by taking the average pairwise product of the 256 samples. The match with the maximum correlation is taken as the best.

The results of this evaluation are depicted in Figure 4.6. The vertical axis of this figure denotes the algorithm efficacy, while the horizontal axis indicates the number of sample windows averaged in time to generate the live signature. Note that the Euclidean and SSD algorithms have same efficacy, their therefore overlap.

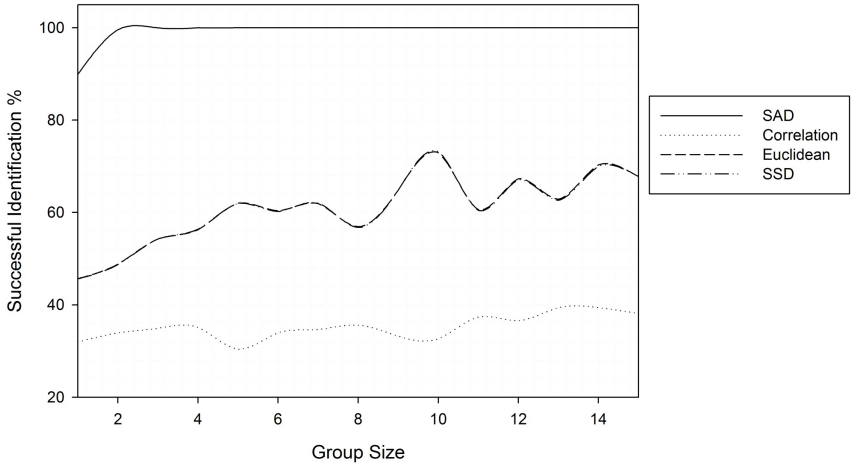

Figure 4.6: Target Identification Algorithm Comparison

4.4 FSKCW Simulation and Ranging Experiments

The first generation RADAR system described in this dissertation is incapable of determining the range to any objects of interest since it operates in the Doppler mode without any modulation of the transmitted energy. This functionality is added in the second generation in which ranging capabilities are provided by means of FSKCW modulation as introduced in Section 3.1.1. Range to the target is determined by comparing the phase of the two IF signals at the peak frequency. This process is illustrated in Figure 4.7.

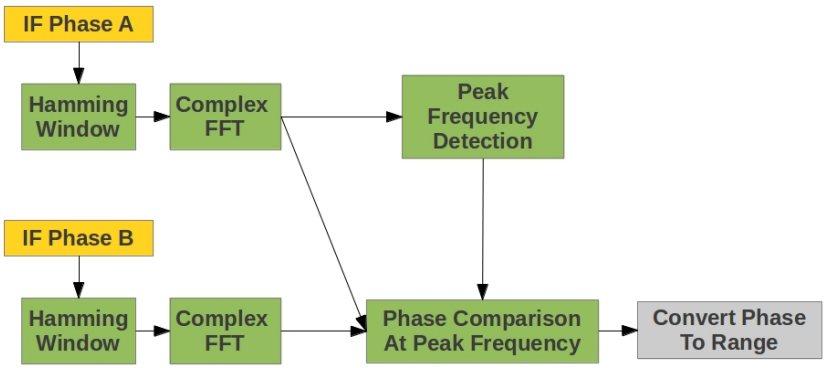

Figure 4.7: FSKCW Ranging Methodology

In practice, however, the phase measurements output by the RADAR hardware are noisy and, therefore, must be filtered prior to use. The targets of interest typically appear to be constricted by Newtonian mechanics and a simple scalar Kalman filter can be used to filter the phase measurements. Prior to hardware implementation, some amount of information regarding the sensor noise parameters, must be determined. This is done through repeated executions of a non-iterative MATLAB simulation of the FSKCW ranging process. The simulation aims to simulate the processing that must be performed on the IF signals to determine the range.

The simulation begins by generating two sine waves representing the IF output corresponding to a point target. The frequency is determined by the target velocity and the phase difference is determined by the target range. These signals are digitized and a Hamming window is applied to suppress side lobes. The resulting signals are shown in Figure 4.8. Additive White Gaussian Noise (AWGN) is then introduced to both phases such that the Signal to Noise Ratio (SNR) is 3dB. The result is shown in Figure 4.9.

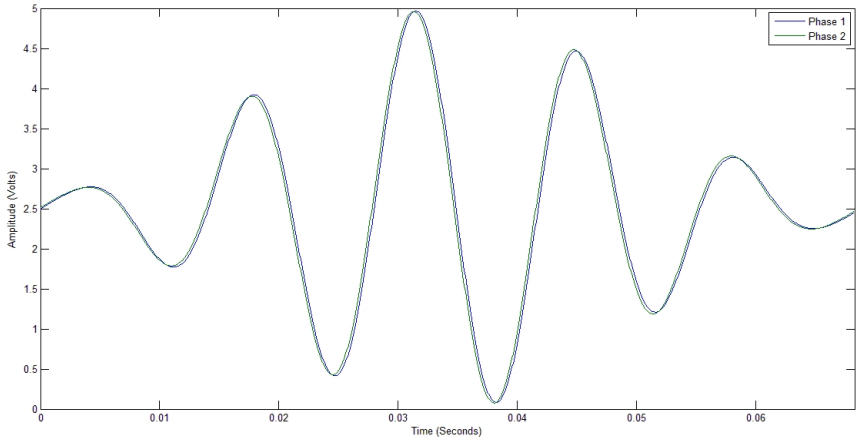

Figure 4.8: Simulated IF Signal Without Noise

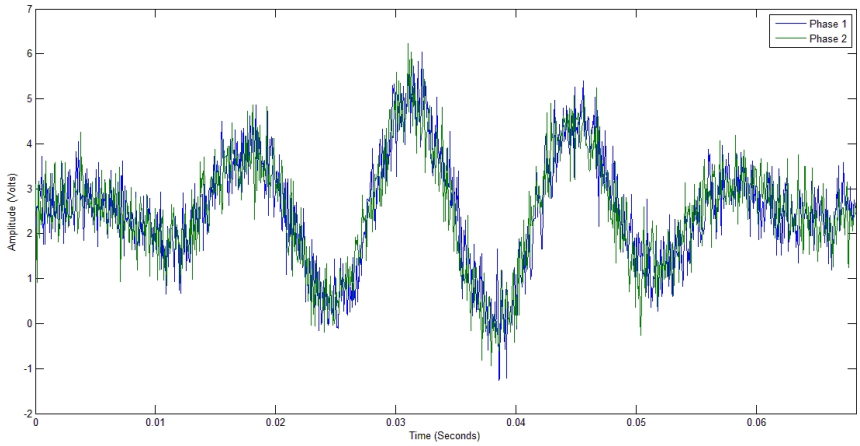

Figure 4.9: Simulated IF Signal With Noise

The methodology described in Figure 4.7 is applied and the resulting data is analysed over a number of non-iterative simulation runs to determine the variance of the measured phase noise. This value is used to tune the gains of an online scalar Kalman filter running in-line with the FSKCW simulation. Figure 4.10 shows comparison of the filtered (green) and unfiltered (blue) phase data for 60 simulation runs. The filter converges after 8 phase measurements, if the IF signal is sampled at 15kHz this would take approximately 0.55 seconds. After convergence, the typical phase error is -0.00536 radians. This is equivalent to a range error of 0.26 meters.

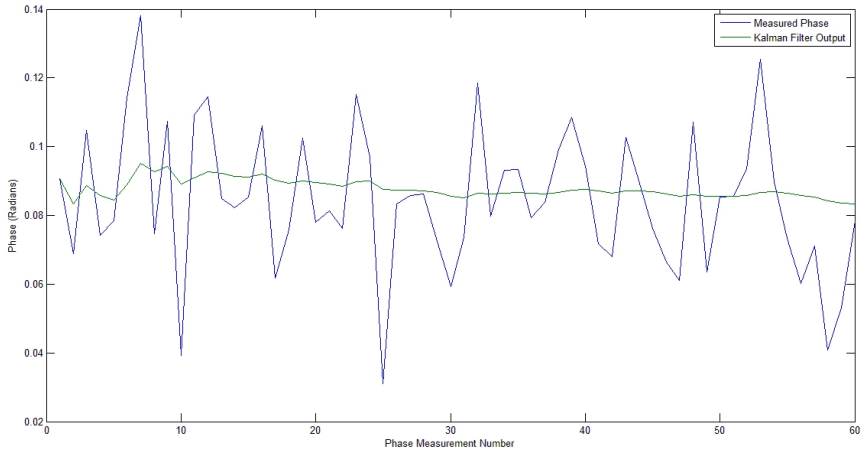

Figure 4.10: Simulated Phase Data

Experimental validation of the ranging method involves the use a moving target as relative motion of the target is a requisite of FSKCW ranging. In this case an aluminium dihedral reflector with an RCS of $2m^2$ is mounted on an O-scale model train, see Figure 4.11 The train traverses along an oval track while the RADAR is arranged such that the main lobe illuminates a linear section of the track. The test setup is illustrated in Figure 4.12.

The test scenario is complicated by the presence of multi-path reflections from objects within the testing room and the detection of the target by both the main

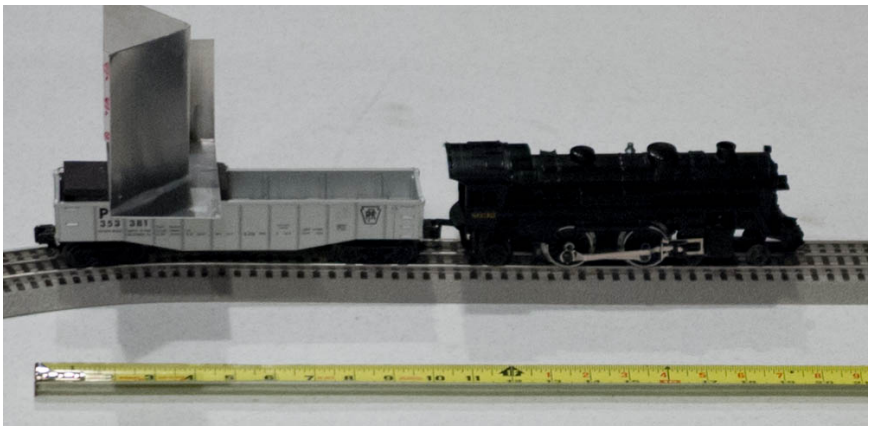

Figure 4.11: O-Scale Train with Doppler Target for FSKCW Experimental Validation

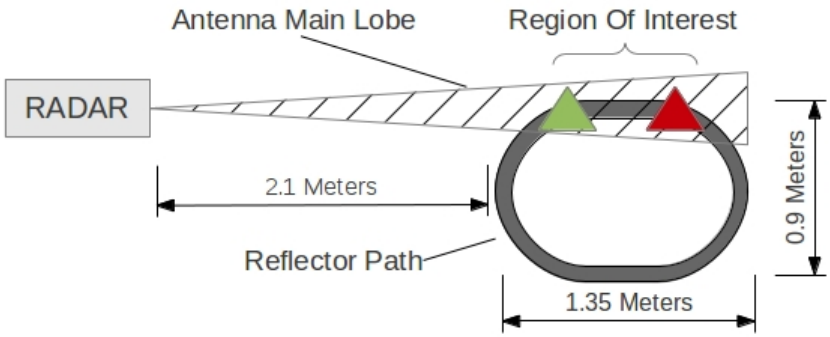

Figure 4.12: FSKCW Ranging Experimental Validation: Test Setup

and side lobes when the target is outside the area of interest. These conditions necessitates the use of target discrimination to pre-select the phase samples that are admitted into the Kalman filter. This target discrimination process consists of two primary metrics: target direction and velocity.

Throughout the testing, the train target traverses the track in a clockwise fashion. From the RADAR's perspective, the target is always heading away from the antenna. This receding motion gives rise to a negative phase measurement (while the converse will give rise to a positive phase shift). This filter effectively eliminates the half of the track through which the train is heading towards the RADAR.

Velocity filtering further reduces the measurement selection to periods in which the target's Doppler shift falls within a particular FFT bin. This condition is met when the target is traversing the region of interest and the antenna Poynting vector is co-linear with the target motion vector.

The test begins by configuring the train's drive system to move the train and target assembly at 0.5m/s, the velocity is then verified by a stopwatch. The RADAR system is then aligned to view the region of interest. The filtered phase data is then collected and stored for further analysis.

Figure 4.13 shows 36 range measurements gathered using this measurement setup. The region of interest bounds (represented as phase) are displayed as green and blue horizontal lines. The red trace is the measured phase data after the real-time target discrimination and range filtering process. The sinusoidal behavior of the measurement is explained by the target discrimination process. When the target enters the region of interest, the measured phase is relatively low. The target then moves away from the RADAR thus causing the range to increase monotonically. This process ends when the target leaves the region of interest. The target goes around the track and the phase measurements are rejected due to the target discrimination process. When the target completes its circuit and re-enters the region of interest the measured phase value is low again and the filtered value is pulled down to reconcile the filter output with the new measurements before following the target's increasing range again.

It should be noted that as the region of interest is small, the prediction stage of the Kalman filter is omitted in these tests. This essentially assumes a stationary target. When transitioning to targets of a more dynamic nature, the Doppler shift in addition to the measurement timestamp can be used to provide a more accurate

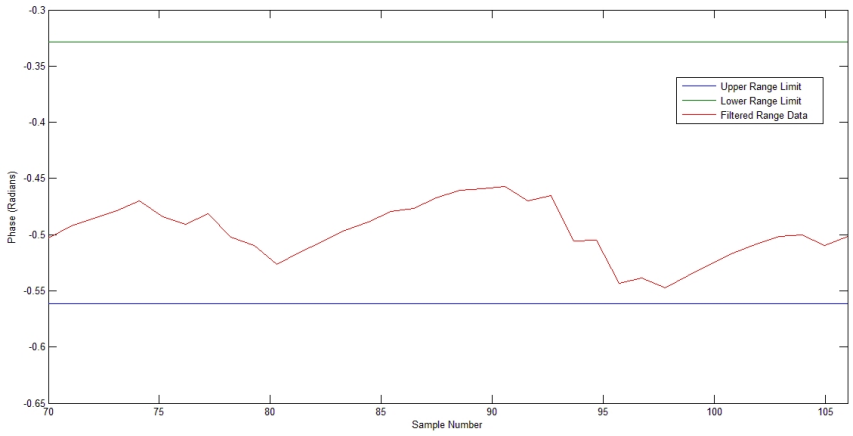

Figure 4.13: FSKCW Ranging Experimental Validation: Results

estimate of the target's current range. The phase estimate would then be of a form described by Equation 4.6.

$$\hat{\phi} = \frac{4\pi(R_{(k-1)} + c(\frac{F_{IF}}{2F_T})(T_k - T_{(k-1)}))}{c} \tag{4.6}$$

where $\hat{\phi}$ is the predicted phase shift and $R_{(k-1)}$ represents the previous range value taken at time $T_{(k-1)}$ ($R_{(k-1)}$ is obtained from the output of previous time steps).

4.5 Azimuth Enabled RADAR Evaluation

Previous sections within this chapter have detailed the hardware and software methods utilized for performing FSKCW ranging against moving targets. However, relative bearing information is unavailable without one of the methods discussed in section 3.4. This section first describes the hardware developed to test the Generation 2a RADAR sensor. The software methods for determining target azimuth are then discussed. Finally, the accuracy of the RADAR is quantified.

4.5.1 RADAR Targets

The evaluation performed in section 4.4 demonstrates the FSKCW concept, however, more accurate evaluation benefits from the use of RADAR targets with a more concentrated distribution of reflecting surfaces (By comparison, the reflecting surface of the train target is distributed over the length of the target which is approximately 0.53 meters long). To address these issues and to evaluate the RADAR using multiple targets, two quad-dihedral reflectors are used, see Figure 4.14

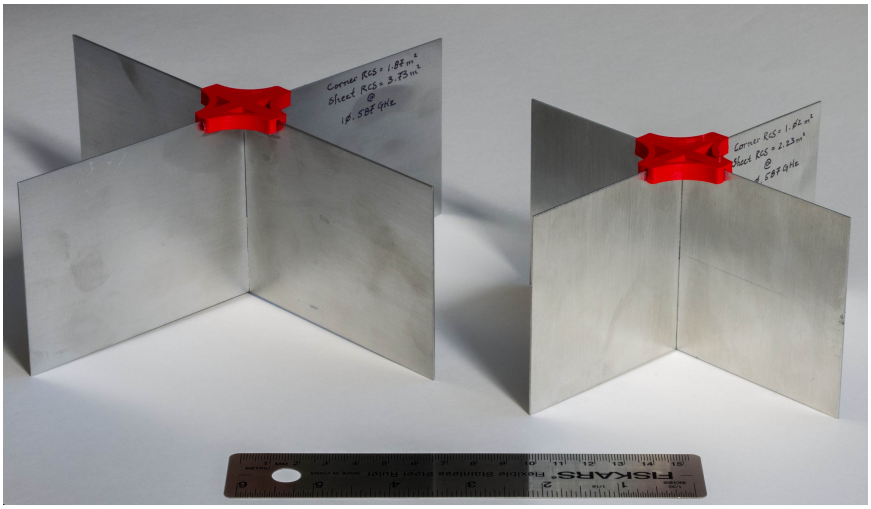

Figure 4.14: Quad-Dihedral RADAR Reflectors (with 6 inch (15cm) size reference)

The use of well documented geometries, see Figures 4.15 and 4.16, in the construction of these reflectors allows for the application of standardized formulas to determine the reflector RCS, see equations 4.7 and 4.8 [5].

$$\sigma_{panel} = \frac{4\pi a^2 b^2}{\lambda^2} \tag{4.7}$$

$$\sigma_{dihedral} \frac{8\pi a^2 b^2}{\lambda^2} \tag{4.8}$$

Where a is the width of the panels, b is the height, λ is the wavelength of incoming radiation, and σ is the RCS.

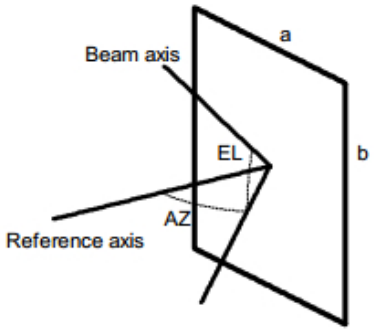

Figure 4.15: Panel RCS Geometry [5]

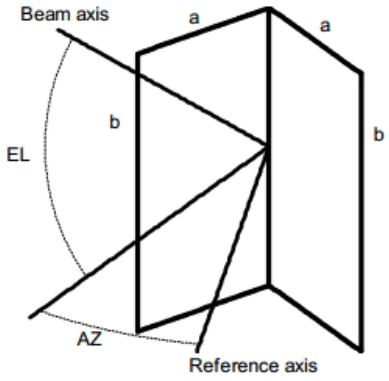

Figure 4.16: Dihedral RCS Geometry [5]

Applying equations 4.8 and 4.7 to the reflectors shown in Figure 4.14 produces the RCS values shown in Table 4.3.

	Large Reflector	Small Reflector
Panel Peak RCS (m^2)	3.73	2.23
Dihedral Peak RCS (m^2)	1.87	1.02

Table 4.3: RADAR Reflector RCS

Since FSKCW RADARs can only detect objects with some motion relative to the RADAR antenna, the reflectors in Figure 4.14 are mounted on a Pololu "3pi" line following robot, see Figure 4.17. This arrangement allows for reflector motion paths to be created using any high contrast line, which the vehicle follows using optical sensors at speeds up to $0.9\frac{m}{s}$ [61]

Within this research, two oval tracks are created using 19mm wide electrical tape on a white posterboard substrate. The dimensions of the tracks are shown in Figure 4.18

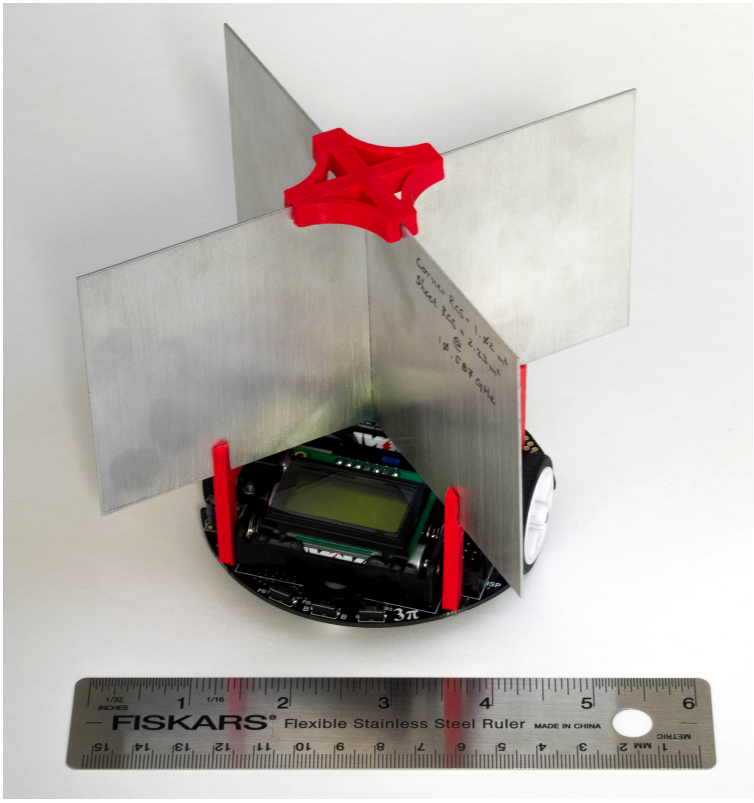

Figure 4.17: Line Following RADAR Target (with 6 inch (15cm) size reference)

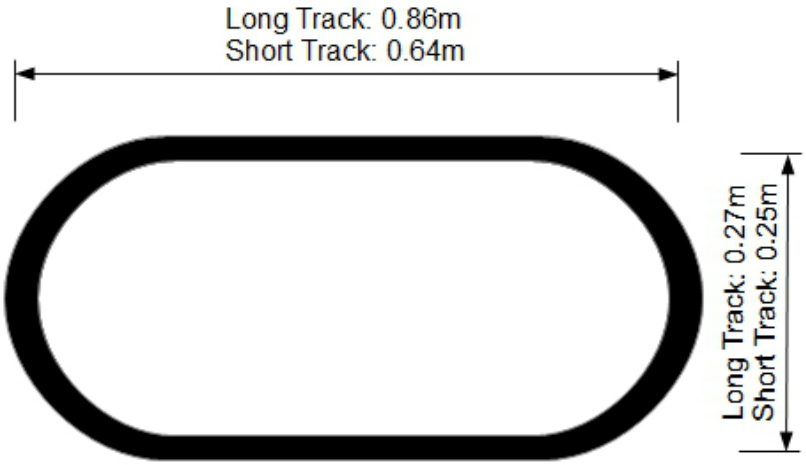

Figure 4.18: RADAR Reflector Path Dimensions

4.5.2 Azimuth Measurement Methodology and RADAR Interface

The Generation 2a RADAR hardware uses mechanical scanning to direct the main lobe of the antenna. Throughout the research, the angular width of the path swept by the antenna is 90° with the period of the sweep being set to 2 seconds. RADAR range measurements are not synchronized with the motion of the antenna, and samples are continually gathered at the RADAR's maximum rate. The maximum range measurement rate is limited by the FSKCW processing method which requires the use of floating point FFTs. Unfortunately, the XMOS hardware does not possess a floating point unit and floating point operations are emulated using the XMOS' fixed point hardware. This causes a performance reduction thus limiting the RADAR sample update rate to approximately 7 Hz (a measurement period of 0.14 seconds). As a result, during each measurement period, the antenna rotates 6.3° and each 90° antenna sweep has, on average, 14.3 range measurements. Before and after each range measurement period, the antenna position is sampled and the range measurement is associated with the linear interpolation of these angles.

Each range measurement also has an associated "activity metric" which is simply the sum of the FFT bin magnitudes (excluding bin 0 with represents the DC component of the IF signal). When the activity metric values are arranged spatially and plotted, the local maxima of the plot represents individual targets if the local maxima amplitude exceeds the noise threshold for the activity metric values. The noise threshold is determined experimentally by directing the RADAR towards an area with no Doppler activity and increasing the threshold value to eliminate false detections. For the purposes of this research, each local maxima is associated with

a particular target and the azimuth values are filtered using a scalar kalman filter in the same manner that the FSKCW phase values are filtered.

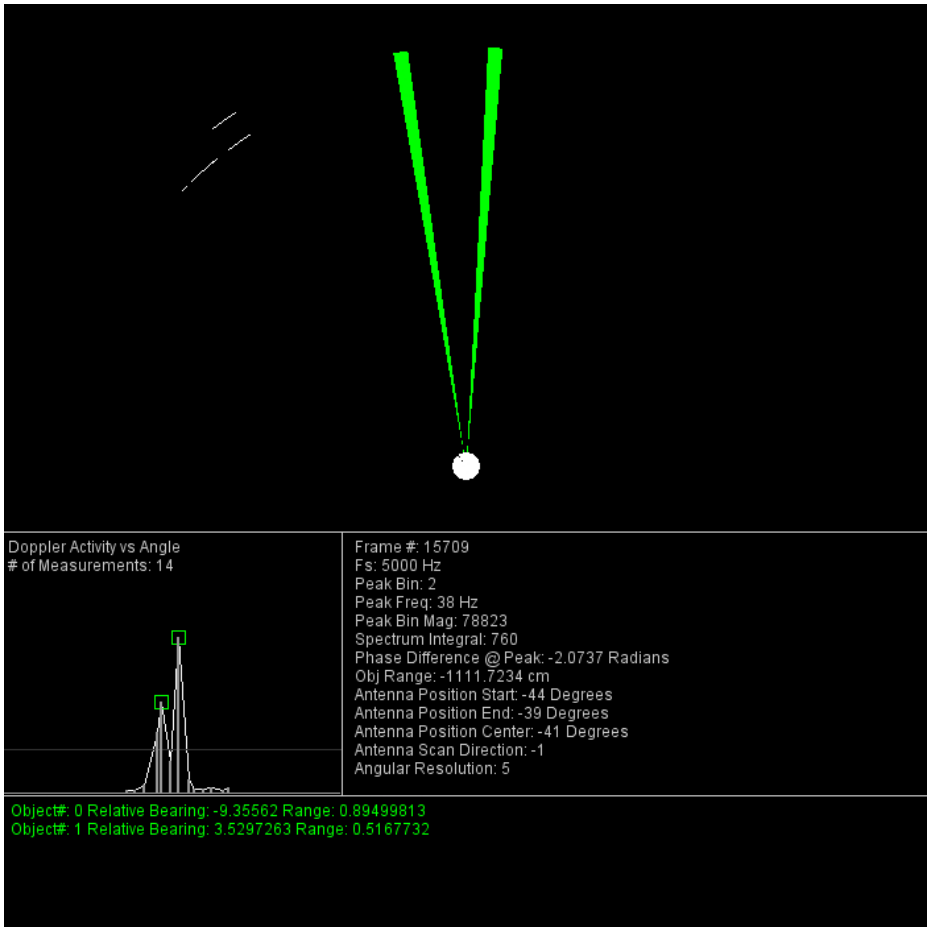

Figure 4.19: RADAR Interface Screenshot

Figure 4.19 is a screen capture of the laptop-based RADAR interface developed for this research and shows a plot (in the lower left) of the activity metrics for a scenario with two targets. Written in the *Processing* programming language, the RADAR interface software serves to provide a real-time visual representation of the RADAR data and record the RADAR data to a file for off-line analysis.

4.5.3 Combined Range and Azimuth Measurement

Combined range and azimuth measurements are made using a series of small scale scenarios in which the target vehicles described in subsection 4.5.1 are arranged then set in motion about oval tracks also described in subsection 4.5.1. Throughout all scenarios, the target vehicle velocity is approximately $0.5\frac{m}{s}$ and is measured by using a quartz chronograph (Seiko SDNA57) to determine the time the target vehicles require to make a circuit of their respective tracks.

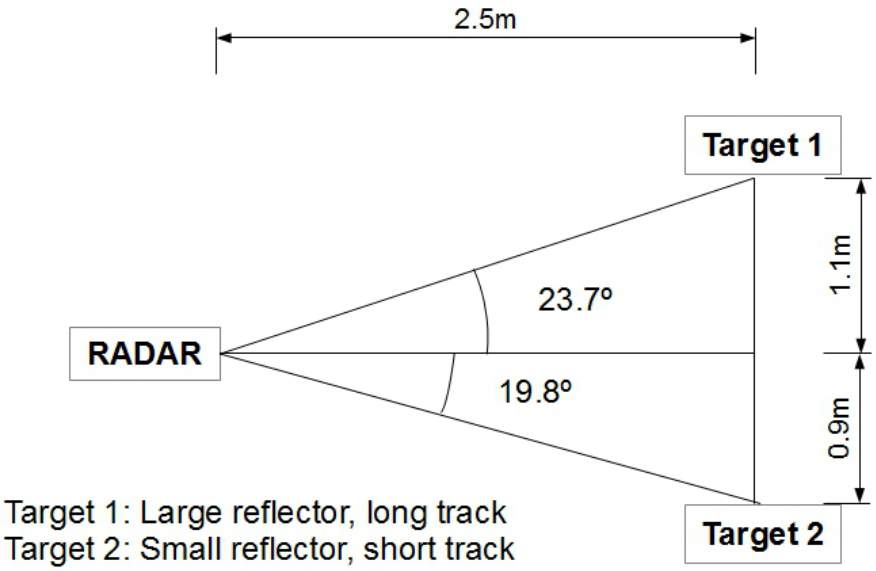

Figure 4.20: Generation 2a Test Scenario 1

Figure 4.20 shows the physical layout of the RADAR and the target vehicles during the first evaluation scenario. Scenario 1 is performed with all test elements located in a reinforced concrete room with no effort to reduce multi-path reflections. For this scenario three tests are performed. First, target 1 is placed within the environment and data is gathered for 5 minutes while target 1 is traversing the track in a clockwise direction. The second test is performed by introducing target 2 into the

environment along with target 1. Throughout the second test, target 1 is stationary and target 2 is moving around its track in a counter clockwise direction. As with the first test, data is gathered for 5 minutes. The third and final test is performed with both target 1 and target 2 moving. As with the previous tests, data is gathered for 5 minutes.

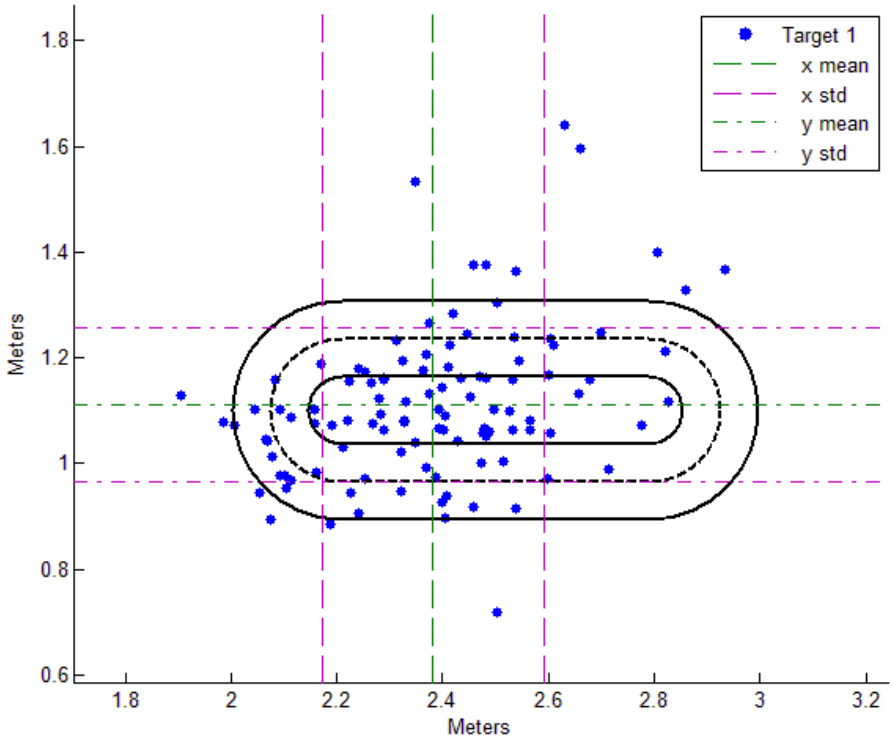

Figure 4.21: Scenario 1, Target 1 Only (The RADAR is positioned at the origin, (0,0))

Figure 4.21 displays the results from scenario 1, test 1 with the view centered around target 1. The path made by the target vehicle is indicated by the dashed oval. However, the reflector is not a point target and physically sweeps the area bounded by the two solid ovals. The RADAR measurements are shown (after filter convergence) as a scatter plot with each measurement being the result of a single

90° antenna sweep. The mean and standard deviation of the measurements are also plotted with the X and Y axis mean values shown in green and the standard deviation shown in magenta and presented numerically in Table 4.4.

Parameter	Physical Layout	RADAR Measurement	Error
X Axis Mean (m)	2.50	2.38	0.12
X Axis Std. Dev.	-	0.21	-
Y Axis Mean (m)	1.10	1.11	0.01
Y Axis Std. Dev.	-	0.15	-
Mean Relative Bearing	23.70°	25.03°	−1.33°
Mean Line of Sight Range (m)	2.73	2.63	0.1

Table 4.4: Scenario 1, Test 1: Numerical Analysis

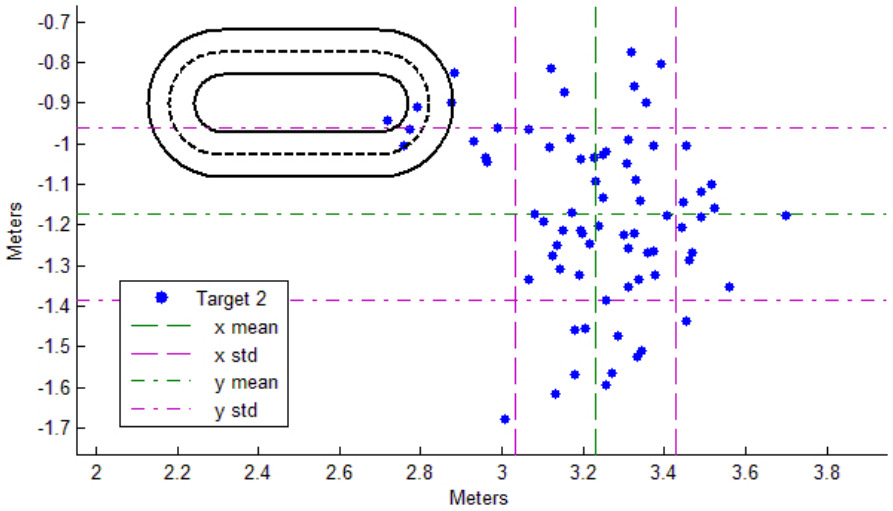

Figure 4.22: Scenario 1, Target 2 Moving, Target 1 Stationary

Figure 4.26 displays the results from scenario 1, test 2, with the view centered around target 2. A numerical analysis of the test is shown in Table 4.9. Figure 4.23 shows the results for scenario 1, test 3, which involves both target vehicles moving simultaneously. A numerical analysis is shown in Table 4.6.

Parameter	Physical Layout	RADAR Measurement	Error
X Axis Mean (m)	2.50	3.23	0.73
X Axis Std. Dev.	-	0.20	-
Y Axis Mean (m)	-0.9	-1.17	0.27
Y Axis Std. Dev.	-	0.21	-
Mean Relative Bearing	$-19.80°$	$-19.91°$	$0.11°$
Mean Line of Sight Range (m)	2.25	3.44	-1.21

Table 4.5: Scenario 1, Test 2: Numerical Analysis

Parameter	Physical Layout	RADAR Measurement	Error
Target 1:			
X Axis Mean (m)	2.50	3.63	-1.13
X Axis Std. Dev.	-	0.32	-
Y Axis Mean (m)	1.10	1.56	-0.46
Y Axis Std. Dev.	-	0.35	-
Mean Relative Bearing	$23.7°$	$23.35°$	$0.35°$
Mean Line of Sight Range (m)	2.73	3.971	-1.24
Target 2:			
X Axis Mean (m)	2.50	2.18	0.32
X Axis Std. Dev.	-	0.18	-
Y Axis Mean (m)	-0.9	-0.73	-0.17
Y Axis Std. Dev.	-	0.11	-
Mean Relative Bearing	$-19.8°$	$-19.62°$	$-0.18°$
Mean Line of Sight Range (m)	2.25	2.18	0.07

Table 4.6: Scenario 1, Test 3: Numerical Analysis

Scenario 1 demonstrates the sensitivity of the FSKCW ranging technique to multipath signal propagation. Multipath signal propagation is defined within this research as any signal path not of the same length and direction as the LOS vector between the RADAR antenna and any given target. Within scenario 1, the primary cause of multipath errors is the addition of another RADAR reflector within the area swept by the antenna. As Tables 4.4 through 4.6 show, the average angular measurement error is $0.49°$ and the majority of the position measurement error is due to range measurement inaccuracies. For scenario 1, test 1, the average range measurement

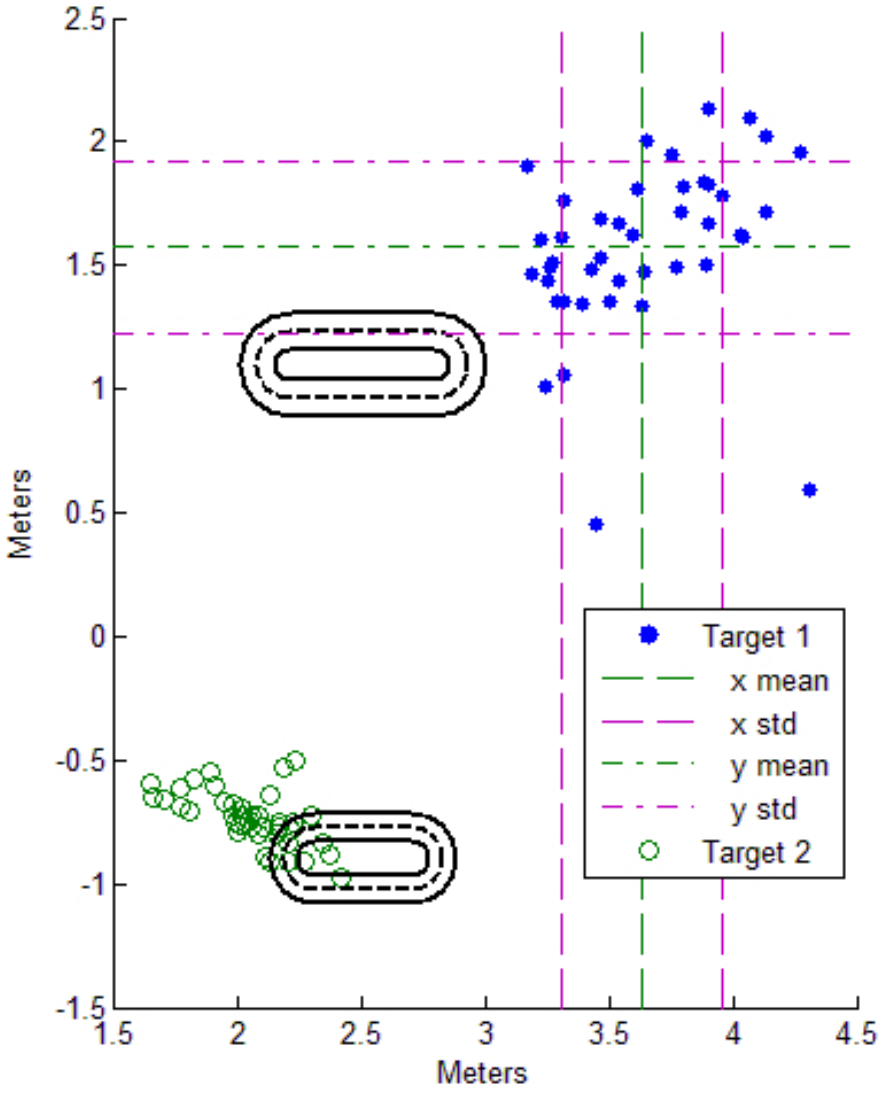

Figure 4.23: Scenario 1, Both Targets In Motion

error is 0.1m. Throughout the test, the transmit frequency modulation bandwidth is 4.45MHz, thus a 0.1m error is equal to a phase error of 0.5329°, which is, in turn, 0.3% of the 180° unambiguous range limit. Table 4.7 shows the range error analysis for the tests performed in scenario 1. While range measurement errors are ideally 0%, the range measurement errors throughout scenario 1 are comparable with other sensor

technologies. For example, the Hokuyo URG-04LX-UG01 scanning laser rangefinder has a rated accuracy of ±3% the measurement range [62].

Data Set	Range Error (m)	Phase Error	% of R_{unamb}
Test 1	0.10	0.5329°	0.3%
Test 2	1.21	6.4659°	3.6%
Test 3, Target 1	1.24	6.6262°	3.7%
Test 3, Target 2	0.07	0.3741°	0.2%

Table 4.7: Scenario 1 Range Error Analysis

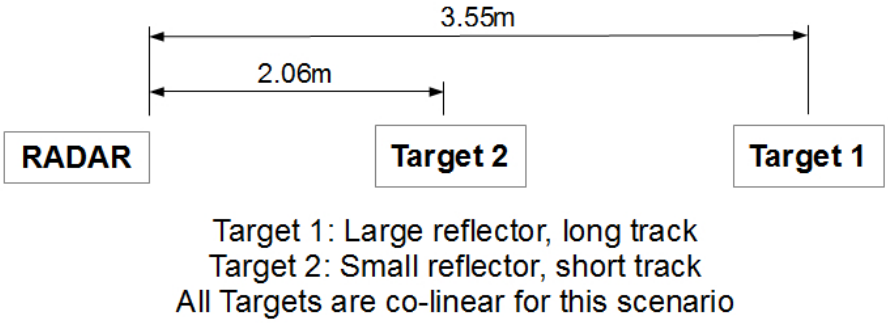

Figure 4.24: Generation 2a Test Scenario 2

Figure 4.24 shows the physical layout of the RADAR and the target vehicles during the second evaluation scenario. All measurements in scenario 2 are made within a steel hanger and no multi-path mitigation steps are taken. For this scenario, two tests are performed. For the first test, target 2 is placed within the environment and RADAR measurements are made for 5 minutes (0.5Hz update rate). During the second test, target 1 is introduced and RADAR measurements are made in an attempt to gather position information regarding both targets. A graphical representation of the scenario 2, test 1 RADAR measurements is shown in Figure 4.25 while a numerical analysis of the test results is shown in Table 4.8. Figure 4.26 and Table 4.9 provide the same information for scenario 2, test 2. As with scenario 1, the RADAR is located at the origin throughout scenario 2 (coordinate 0,0).

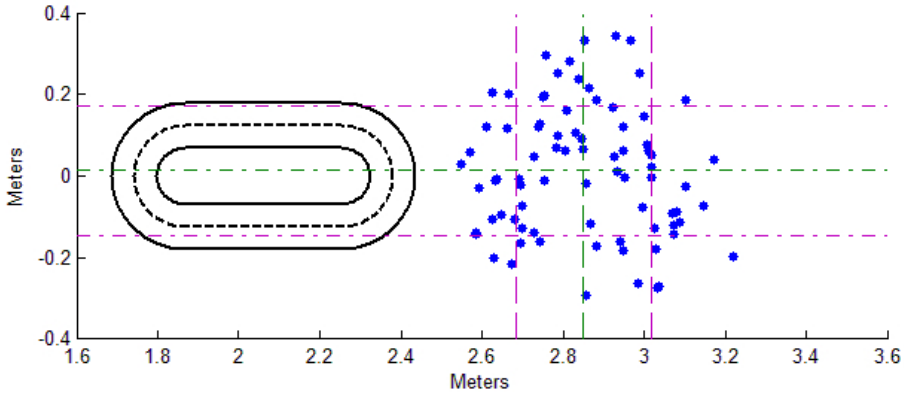

Figure 4.25: Scenario 2, Target 2 Only

Parameter	Physical Layout	RADAR Measurement	Error
X Axis Mean (m)	2.06	2.851	0.79
X Axis Std. Dev.	-	0.17	-
Y Axis Mean (m)	0.00	0.01	0.01
Y Axis Std. Dev.	-	0.16	-
Mean Relative Bearing	0.00°	0.28°	0.28°
Mean Line of Sight Range (m)	2.06	2.86	0.78

Table 4.8: Scenario 2, Test 1: Numerical Analysis

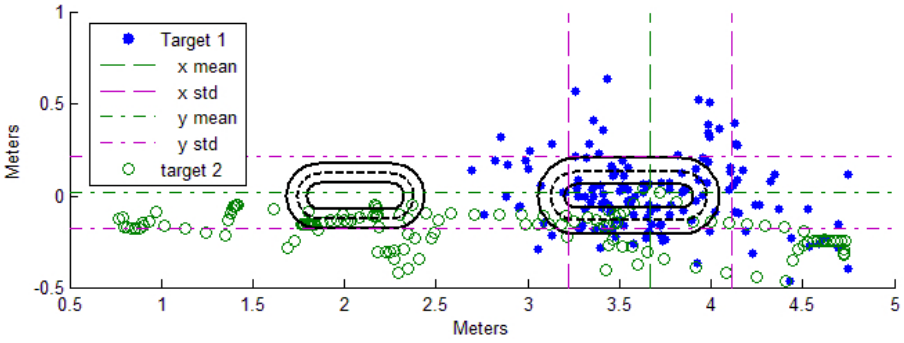

Figure 4.26: Scenario 2, Both Targets

Scenario 2 demonstrates another vulnerability of FSKCW RADARs: target masking. During test 2, target 1 is masked by target 2 in that the target 2 interrupts the line of sight path between the RADAR and target 1. Due to the longer measurement

Parameter	Physical Layout	RADAR Measurement	Error
Target 1:			
X Axis Mean (m)	3.55	3.67	-0.12
X Axis Std. Dev.	-	0.45	-
Y Axis Mean (m)	0	0.02	-0.02
Y Axis Std. Dev.	-	0.20	-
Mean Relative Bearing	0.00°	0.33°	−0.33°
Mean Line of Sight Range (m)	3.55	3.67	-0.12
Target 2:			
X Axis Mean (m)	2.06	2.87	-0.81
X Axis Std. Dev.	-	1.22	-
Y Axis Mean (m)	0	-0.20	0.20
Y Axis Std. Dev.	-	0.12	-
Mean Relative Bearing	0.00°	−4.50°	4.50°
Mean Line of Sight Range (m)	2.06	2.89	-0.83

Table 4.9: Scenario 2, Test 2: Numerical Analysis

range, target 1 returns less power to the RADAR than target 2 despite target 1 having a larger RCS. Nevertheless, the range filter converges for target 1 rather than target 2. This is due to the more rapid phase reversals observed for target 2 that are not as prevalent in target 1; Explained differently, the sign of the phase difference between the two IF channels used for FSKCW ranging depends on whether or not the target is heading towards or away from the RADAR. When utilizing the oval tracks described in Figure 4.18 this phase reversal occurs twice for every lap of the target vehicle. Since both target vehicles are traveling at the same speed, and target 2 utilizes a shorter track, the RADAR measurements of target 2 contain more phase reversals which serve to corrupt the range measurement and prevent convergence of the range filter. An analysis of the range errors for scenario 2 is shown in Table 4.10.

Data Set	Range Error (m)	Phase Error	% of R_{unamb}
Test 1	0.78	8.4298°	4.68%
Test 2, Target 1	0.12	1.2969°	0.72%
Test 2, Target 2	0.83	8.9702°	4.98%

Table 4.10: Scenario 2 Range Error Analysis

4.6 Remarks

Within this chapter a number of key techniques are presented and experimentally validated. First, the origins of micro Doppler signatures are explored and their use as an identifying characteristic of miniature aircraft is experimentally demonstrated. Furthermore, the theoretical range within which various miniature aircraft can be identified is calculated. It should be noted that these ranges are calculated under the assumption that the rotor blades of the vehicle in question are of a metallic ribbon geometry as described in section 4.1. However, this is rarely, if ever, the case with the vehicles utilized. For example, many 450 to 600 size RC aircraft make extensive use of Glass Fiber Reinforced Plastic (GFRP) and plastic in their construction. Other comparable aircraft, such as the Parrot AR drone, use very few microwave reflecting components in their construction. The Parrot's fuselage is comprised of expanded polypropylene foam while the rotors and power transmission assemblies are constructed using nylon plastic. This construction method gives rise to an exceedingly small RCS, thus the detection and identification processes used in this research, while not untenable, require high power levels to be practical. For example, the Parrot AR drone can be detected and identified utilizing the generation 1 hardware. However, the same aircraft is undetectable utilizing the generation 2 and 2a hardware which transmits $\frac{1}{25}^{th}$ the RF power of the generation 1 hardware.

In addition to detection and identification, target range and relative bearing information can also be obtained using the RADAR. However this is not without certain constraints. the FSKCW ranging process within this research is first simulated in section 4.4 wherein simulations indicate that with a 3dB SNR, the range errors should be, on average, 0.26 meters. Throughout the hardware evaluation process the average measured range error is 0.62 meters or 138% of the range error encountered during the simulation. While there are a number of factors that cause this discrepancy, there are three dominant causes: multi-path error, frequency setting error, and the direction reversals of the RADAR targets. As multi-path errors are adequately explained above, this section will provide more in depth information regarding frequency setting and direction reversals.

Frequency setting error is, in itself, comprised of two parts: the unmodulated carrier error, and the frequency modulation error. The first item, unmodulated carrier error, is defined as an error in the assumed transmit frequency of the RADAR without the square wave modulation used for determining the range to the target. For the RADAR front end used in the generation 2 and 2a prototypes, the unmodulated carrier frequency is 10.587 GHz. However, due to the construction technology, this frequency is temperature dependent and can vary by up to 6.5 MHz throughout the operating temperature range. Assuming a linear relationship between frequency and temperature, this equates to approximately $230\frac{kHz}{^{\circ}C}$ and is a relatively minor error source accounting for no more than 0.06% of the unmodulated carrier error [6].

The frequency modulation error is markedly more important and is defined as the error between the expected and actual frequency shifts caused by the modulation process. The maximum frequency modulation range of the RADAR front end is theoretically as 5MHz (at room temperature) and is obtained by applying a square

wave between 0 and 5v to the tuning pin of the RADAR front end [6]. However, during the initial evaluation the actual frequency range was determined to be 4.45 MHz. This value was obtained by assembling a test scenario with a moving RADAR reflector which passes through a marker located a specific distance from the RADAR. An oscilloscope then used to measure the relative phase between the two IF signals as the RADAR target passes the marker. Since the speed of light, measured phase, and range to the target are known quantities, the modulation bandwidth is be determined by rearranging equation 3.9 to the form shown in equation 4.9 and solving for the bandwidth, BW.

$$BW = \frac{c(\phi_A - \phi_B)}{4\pi Range} \tag{4.9}$$

The dependence of the accuracy of the range measurements on the accurate knowledge of the modulation bandwidth is demonstrated by noting that for an object with a measured phase difference of 20° the calculated range is 1.87 meters for a modulation bandwidth of 4.45 MHz. If however, the modulation bandwidth is 5 MHz, the calculated range is 1.67 meters. This is an error of 0.2 meters or 10% of the original measurement and is therefore a more significant source of range measurement errors than the unmodulated carrier error mentioned above.

In addition to errors caused by the uncertainty in the microwave section, there exist errors caused by the nature of the motion of RADAR targets used throughout this research. In order to simplify the experimental validation of the RADAR prototypes it is necessary to have RADAR targets whose average location is a known constant. By definition, this conflicts with the need for the mobile targets required by the FSKCW ranging method. Therefore, throughout the evaluation process, the

RADAR reflectors travel about oval tracks. Circular tracks would allow more convenient error measurement metrics to be used, however, their use would exacerbate the phase reversal problem briefly mentioned during the analysis of scenario 2.

Since the sign of the phase difference between the two IF signals used for FSKCW ranging is dependent on the direction of the target motion, a reversal of the apparent target motion direction results in a phase reversal. Figure 4.27 shows an oscilloscope capture of both RADAR IF signals while a target within the RADAR's field of view undergoes three direction reversals. The phase reversal is indicated by the regions with low signal amplitudes.

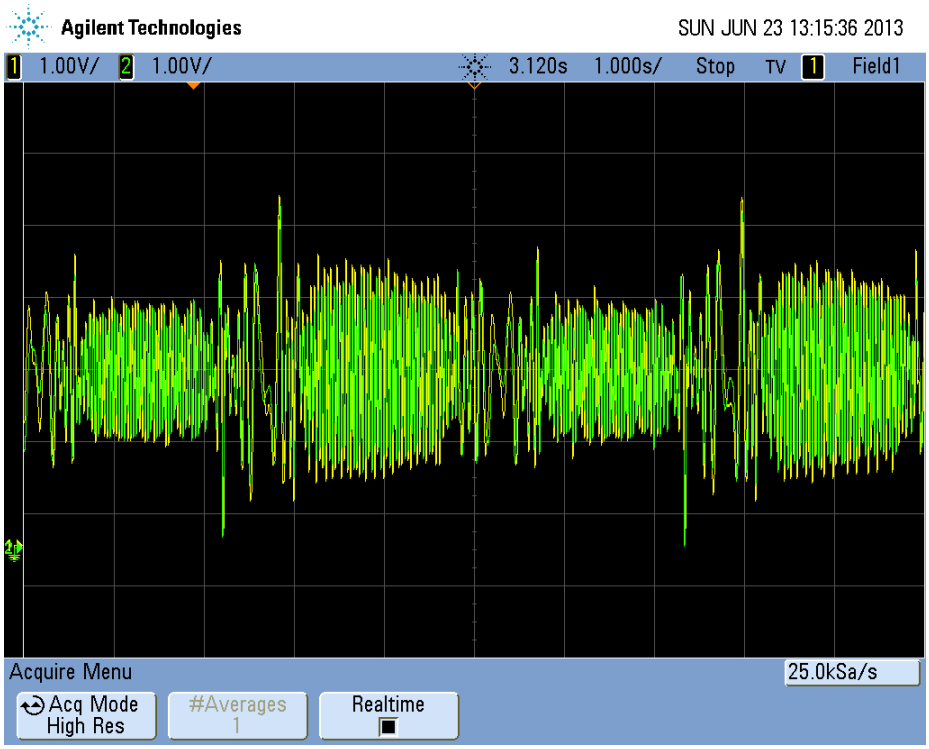

Figure 4.27: Oscilloscope Capture of Both IF Signals For Three Target Direction Reversals

Figure 4.28 shows an enlarged view of a phase reversal. On the left side of the image, the green trace is leading the yellow trace, while on the the right side,

the yellow trace is leading the green trace. The figure shows 1 second of IF data, however, the RADAR system is sampling at 512 samples at a time at 5 kHz giving rise to a data packet length of 0.1024 seconds. Thus, over Figure 4.28 the RADAR would make roughly 10 phase measurements (ignoring the 7Hz processing speed limit). The phase reversal of the signals take approximately 300ms to complete and therefore for the data set shown in Figure 4.28, 30% of the phase measurements are erroneous. The use of oval tracks (as opposed to circular) reduce the percentage of erroneous measurements by increasing the percentage of time the RADAR reflector spends traveling either towards or away from the RADAR. Nevertheless, the routine phase reversals are the driving factor behind the gathering of data for 5 minutes for each test within the scenarios. This allows adequate time for the range filters to converge and filter the noise caused by phase reversals. Furthermore, the data is only analyzed after the convergence of the filters, which on average, require 10 samples to converge on a useful range value.

Besides range, the other measurement required to localize targets is the target relative bearing. Throughout scenarios 1 and 2, the average relative bearing error is 1.01°. However, it should be noted that for all but two of the tests, the angular errors are below 0.36°. This is achieved by not synchronizing RADAR sampling with the motion of the antenna. The lack of synchronization serves to dither the angle measurements and reduce the measured angular error over time.

Also important is the horizontal antenna beam width, see Figure 4.29, which shows the generation 2 / 2a antenna radiation patterns. The vertical pattern is shown on the left while the horizontal pattern is shown on the right. The -3dB beamwidths are 36° and 18°, respectively. Throughout each measurement, the antenna rotates 6.3°. Since this is less than the horizontal -3dB beamwidth, the entire 90° sector

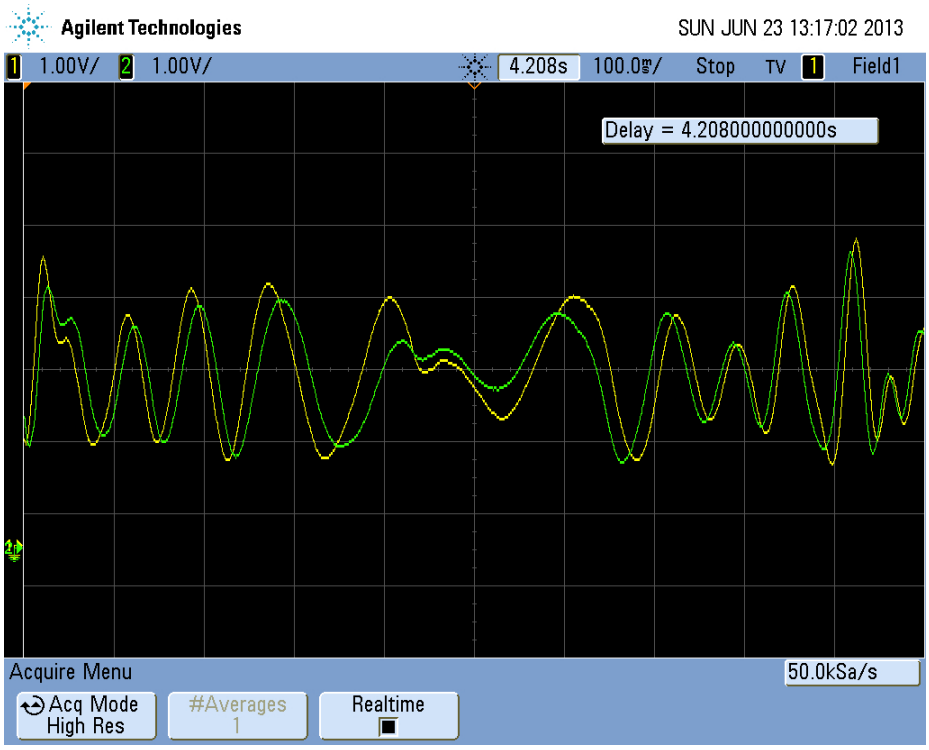

Figure 4.28: Enlarged View of IF Signals During A Target Direction Reversal

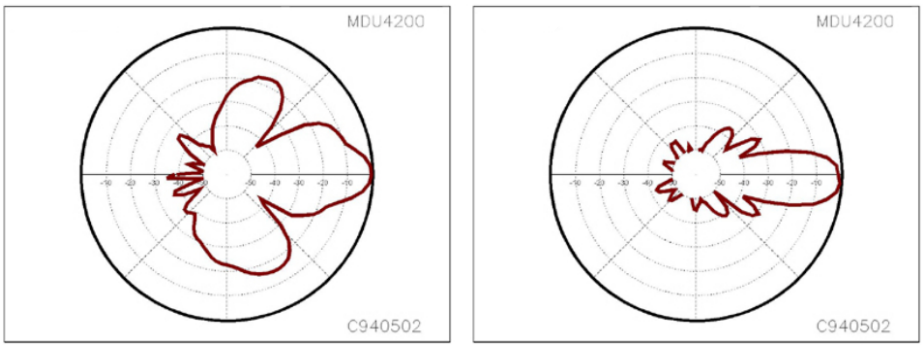

Figure 4.29: Generation 2/2a Antenna Radiation Pattern [6]

swept by the antenna is covered by the main lobe with no gaps. If the antenna main lobe beam width were to be narrower than the angle traversed during the measurement period, there would be gaps in the main lobe coverage throughout any

given antenna sweep and targets that would otherwise be detectable would remain undetected.

This chapter evaluates the hardware developed in chapter 3 and provides a number of metrics regarding the RADAR's accuracy. While the hardware developed is not suited for flight testing due to the low transmit power, limited range, and the slow scan speed, it does provide a valuable proof of concept. In the next chapter, a collision avoidance algorithm that is capable of utilizing the RADAR's identification functionality is presented and evaluated.

Chapter 5

Collision Detection and Evasion

There exist a number of different methods for avoiding collisions between aircraft. This chapter first describes the method this research uses for detecting collisions. Collision avoidance maneuvers are then divided into two categories and a method for determining the lower energy maneuver is presented. Finally, this chapter describes the method this research uses to calculate collision avoidance maneuvers and an empirical evaluation of the method is performed.

Stated differently, the collision mitigation process consists of a number of operations: target detection, target identification, collision detection, and host motion planning. The first two operations are described in Chapter 4. This chapter is concerned with the remaining two: collision detection and host motion planning.

5.1 Collision Detection

Collisions between two objects can be described in terms of relative bearing and range. A perfect collision between two point objects involves maintaining a constant

relative bearing while the range between the two objects decreases. Aircraft have a non-zero volume and cannot be considered to be point objects. Furthermore, there exists a region around most aircraft that should remain free from other aircraft due to both safety and aerodynamic concerns. Throughout this dissertation, the shape of this exclusion region is assumed to be circular as viewed along the gravity vector. The dimensions of these regions are defined in terms of their radii, r_n. Figure 5.1 illustrates an arrangement involving two aircraft.

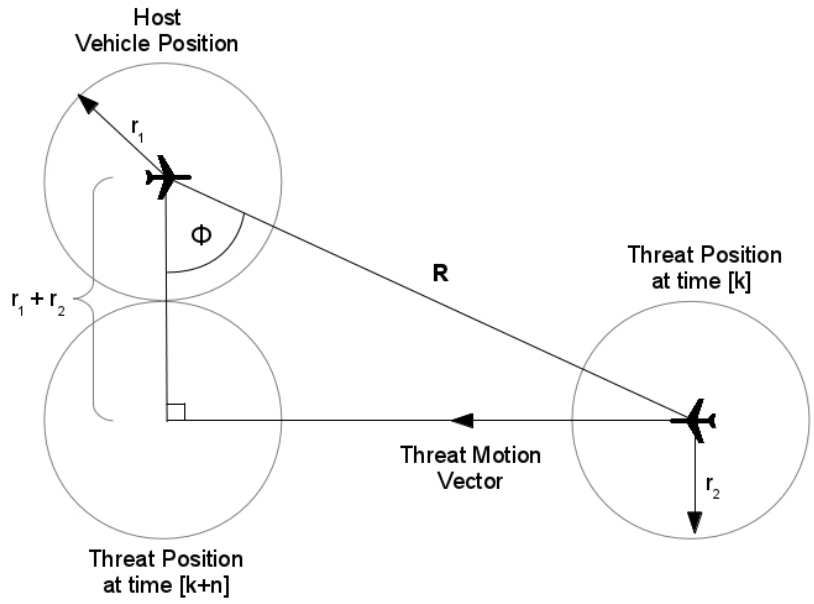

Figure 5.1: Collision Geometry

A minimum distance miss is achieved when the exclusions regions intersect at a single point and is defined as $r_1 + r_2$. The boundary dividing a collision condition and safe trajectories is defined in Equation 5.1. where Φ is the line of sight (LOS) angle, R is the LOS range. Figure 5.2 displays the collision boundary for $r_1 = 5$ meters and $r_2 = 10$ meters.

$$\frac{d\Phi}{dR} = \frac{r_1 + r_2}{R^2\sqrt{|1 - \frac{(r_1+r_2)^2}{R^2}|}} \tag{5.1}$$

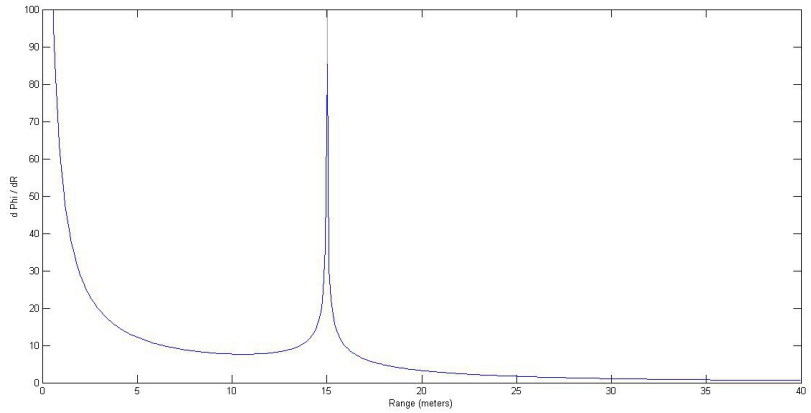

Figure 5.2: $\frac{d\Phi}{dR}$ Plot for $r_1 = 5$ meters and $r_2 = 10$ meters

This plot is divided into several regions. The first region is the area of the plot in which the LOS range is less than or equal to $r_1 + r_2$. For values within this region, a collision has already occurred and Equation 5.1 is invalid. Likewise, for $R = r_1 + r_2$ the required change in angular rate approaches infinity. The second region is represented by the region above the collision boundary for all $R > r_1 + r_2$. Within this region, $\frac{d\Phi}{dR}$ is high enough to avoid a collision. The final region is the region below the collision boundary for all $R > r_1 + r_2$. Within this region, $\frac{d\Phi}{dR}$ is low enough to cause a breach of the clearance regions.

For every timestep, R, r_1, and r_2 are entered into Equation 5.1 to determine a value of $d\Phi$ against which the RADAR data is compared. If the measured $d\Phi$ value is below the calculated threshold $d\Phi$, then a collision is detected.

5.2 Collision Avoidance Maneuver Classes

Once a collision has been detected using the methodology described in section 5.1, some action by the host vehicle is required to avoid the collision. This research divides collision avoidance actions into two categories: purely vertical maneuvers (altitude changes) and horizontal maneuvers with no vertical component (heading changes). Complex paths, incorporating both vertical and horizontal maneuvers are not investigated in an effort to simplify the analysis. Furthermore, as the currently implemented transponder technology discussed in chapter 1 prescribes vertical collision avoidance maneuvers, this research aims to examine the efficacy of collision avoidance maneuvers within the horizontal plane when the energy consumed in such a maneuver is less than or equal to the energy consumed in a vertical maneuver.

There are two key assumptions made for this analysis. First, it is assumed that the host vehicle maintains a constant forward velocity throughout the scenario, i.e. throughout the analysis, the rate at which the vehicles follow their trajectories is a constant. This is because smaller vehicles are able to rapidly vary their velocity while, larger, faster moving, vehicles are unable to adjust their velocities on similar timescales. Furthermore, rapidly varying forward velocities while maintaining a constant altitude makes poor use of a vehicle's available energy by not trading kinetic energy (velocity) for potential energy (altitude).

The second assumption is that collision avoidance maneuvers in the horizontal plane require more physical separation than maneuvers in the vertical plane. This is representative of not only the physical dimensions of most aircraft which are typically wider and longer than they are tall, but also of Federal Aviation Administration (FAA) regulations (Order JO 7110.65U) which requires more vertical separation

than horizontal separation. In some cases under IFR and RADAR guidance rules, 1000 feet vertical separation or 3 miles lateral separation is required [63].

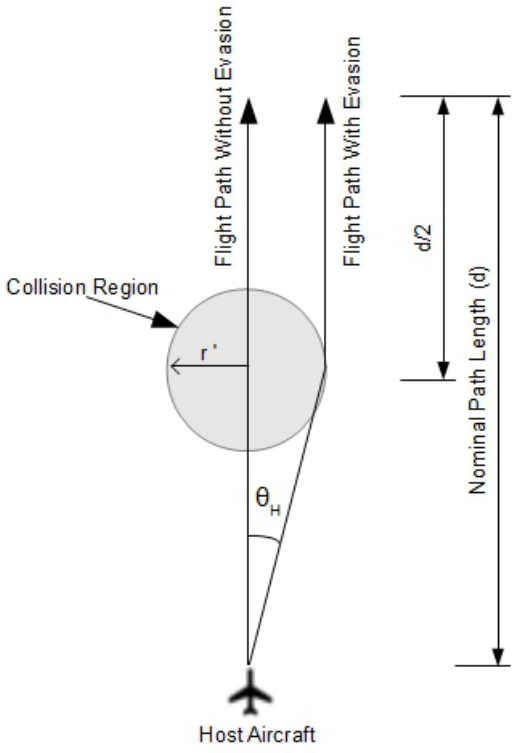

Figure 5.3: Horizontal Evasion Geometry (Top Down View)

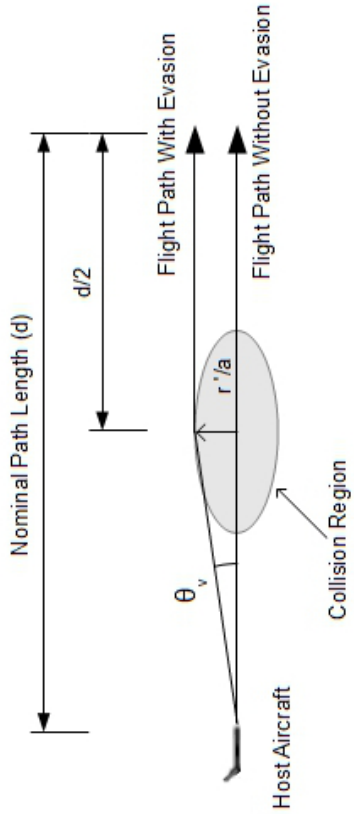

Figure 5.4: Vertical Evasion Geometry (Side View)

A collision avoidance scenario for a single host and a single opposing aircraft, for both horizontal and vertical avoidance maneuvers is shown in Figures 5.3 and 5.4, respectively. The host aircraft is shown on the bottom of the figures with the goal of traversing towards some goal at the top of the figures. Between the current host aircraft location and the goal is a region where, at some point in the future, a collision will occur between the host aircraft and some airborne threat. This "collision region" is modeled as an oblate spheroid with a minor semi-diameter equal to $r^{'}/a$

and a major semi-diameter equal to $r^{'}$. a therefore determines the aspect ratio of the collision region and may be made to conform to arbitrary dimensions on a case by case basis.

The energy required for the vehicle to perform a horizontal maneuver is described by Equation 5.2, while the energy required for a vertical maneuver is described by Equation 5.3.

$$E_H = b\left(0.5d + \frac{0.5d}{\cos(\arctan(\frac{2r^{'}}{d})}\right) \tag{5.2}$$

$$E_V = b\left(0.5d + \frac{0.5d}{\cos(\arctan(\frac{2r^{'}}{da}))}\right) + mg\left(\frac{r^{'}}{a}\right) \tag{5.3}$$

where E_H and E_V are the energies required for horizontal and vertical evasion, respectively. b is the baseline energy consumed by the aircraft for every unit of distance traveled and is determined by dividing the engine output power while cruising by the aircraft cruising velocity. d is the nominal path distance as shown in the figures, a is the aspect ratio of the collision region, m is the mass of the vehicle, g is acceleration due to gravity, and $r^{'}$ is the lateral or vertical displacement required to avoid the collision region.

For any given aircraft, equations 5.2, and 5.3, can be used to determine when a vertical maneuver is superior from an energy standpoint, to a horizontal maneuver. Furthermore, this comparison allows practical limits to be placed on horizontal maneuvers so that the energy consumed in an in-plane horizontal maneuver will not exceed the energy of a vertical maneuver. Figure 5.5 shows the energy required for a horizontal maneuver with a heading change up to 30° compared with an equivalent vertical maneuver.

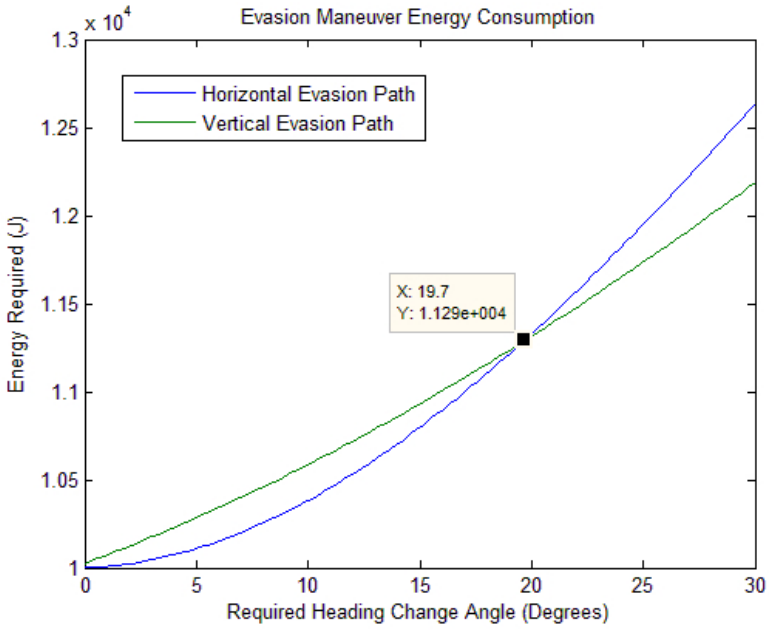

Figure 5.5: Horizontal vs. Vertical Collision Avoidance Energies for a Theoretical Aircraft

The parameters used to obtain Figure 5.5 are for a theoretical aircraft are shown in Table 5.1. For comparison, the baseline energy of a 1.5kg radio controlled aircraft (Eflite Ultra Stick 25e) is approximately $18\frac{J}{m}$ [64]

Parameter	Value
Vehicle Mass (m)	5 kg
Baseline Energy (b)	100 $\frac{J}{m}$
Aspect Ratio (a)	2
Nominal Path Distance (d)	100 m
Gravitational Acceleration (g)	9.8 $\frac{m}{s^2}$

Table 5.1: Parameters for a Theoretical Aircraft. See Figure 5.5

In the case described by Figure 5.5, horizontal collision avoidance maneuvers are more energy efficient than their vertical counterparts, provided that the heading is not modified by more than 19.7 degrees.

Figure 5.6 shows the same analysis performed for a Cessna 172 fixed wing airplane, given the parameters in 5.2. The parameters are selected under the assumption that the aircraft is equipped with a standard Lycoming IO-360-L2A engine operating at 75% of its maximum power rating. This results in the aircraft cruising at 122 knots ($62.76\frac{m}{s}$) at an altitude of 8000ft [65]. As shown in Figure, 5.6, horizontal maneuvers are more energy efficient than vertical maneuvers for heading changes up to 28°.

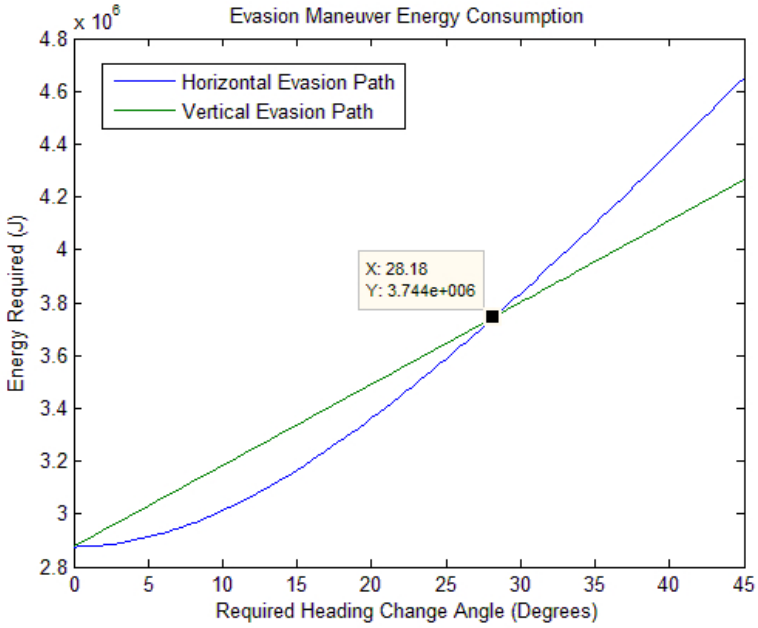

Figure 5.6: Horizontal vs. Vertical Collision Avoidance Energies for a Cessna 172

Parameter	Value
Vehicle Mass (m)	1,111 kg
Baseline Energy (b)	1438 $\frac{J}{m}$
Aspect Ratio (a)	15.8
Nominal Path Distance (d)	2000 m

Table 5.2: Parameters for a Cessna 172.

Compared with fixed wing aircraft, helicopters have higher baseline energy consumption rates. Due to the longer path length, horizontal collision avoidance ma-

neuvers require lower energies only over a narrower angle than fixed wing aircraft. Figure 5.7 displays the results of an evasion maneuver energy analysis for a Bell 206 helicopter. The analysis specifications are shown in Table 5.3 [66]. In this case, horizontal collision avoidance maneuvers require lower energies for heading modification angles up to 12°.

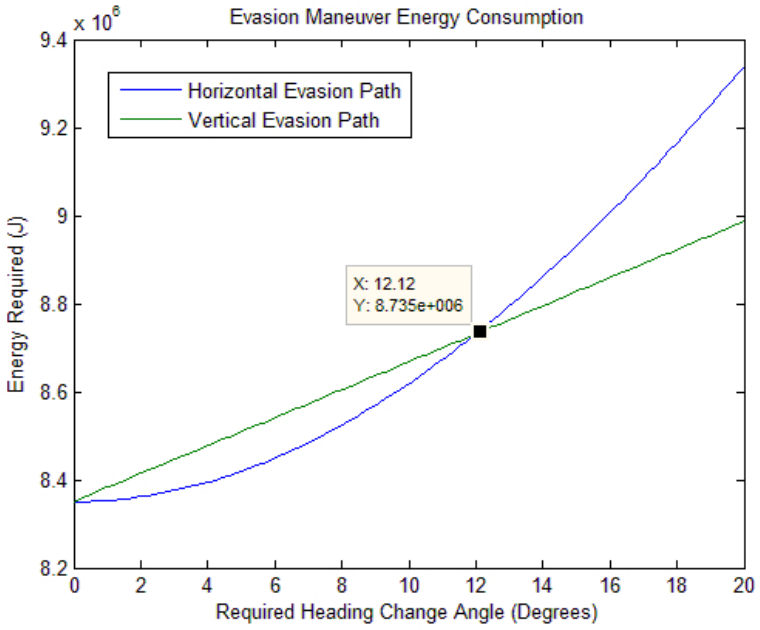

Figure 5.7: Horizontal vs. Vertical Collision Avoidance Energies for a Bell 206

Parameter	Value
Vehicle Mass (m)	1,400 kg
Baseline Energy (b)	4175 $\frac{J}{m}$
Aspect Ratio (a)	15.8
Nominal Path Distance (d)	2000 m

Table 5.3: Parameters for a Bell 206 Helicopter.

5.3 Collision Avoidance Maneuver Planning

As mentioned earlier, this research focuses on investigating the efficacy of collision avoidance maneuvers in the horizontal plane. Section 5.2 demonstrates that such maneuvers are only more energy efficient over an specific angle whose size is dependent on the host vehicle properties, and the aspect ratio of the collision region. This section describes the collision avoidance method used in this research. The description begins with a single opposing aircraft, then the method is generalized for an arbitrary number of threats.

Section 5.1 describes a geometric method for detecting collisions. Where a collision is detected when the Line Of Sight (LOS) vector's rate of change as a function of range is not greater than the boundary described by equation 5.1. This condition occurs when the angular separation between the LOS vector and the relative velocity vector between the host and any given threat is not sufficiently large. Such a condition is illustrated by Figure 5.8. Where Ψ is the angular distance between the LOS and relative velocity vectors.

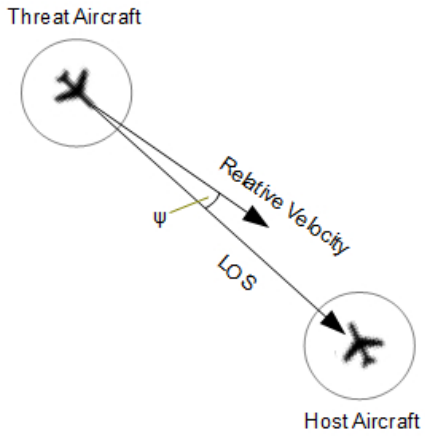

Figure 5.8: Collision Geometry

The collision avoidance algorithm begins by creating a series of alternate LOS vectors for each threat. This is accomplished by rotating the LOS vector about the threat in uniform increments throughout an angular range centered about the current LOS vector known as the "search range". The alternate LOS vectors are shown in Figure 5.9. Where the alternate LOS vectors are displayed in red, the original LOS vector is shown in green, and the relative velocity vector is shown in blue.

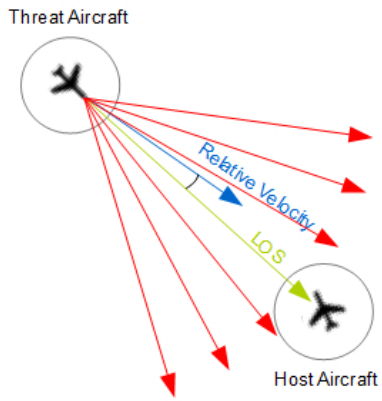

Figure 5.9: Collision Geometry With Alternate LOS Vectors

The absolute magnitude of the angular distances between each alternate LOS vector and the relative velocity vector is then calculated and stored in an array, henceforth referred to as the "vector_distance" array. This has the effect of creating an array where each element represents one possible host vehicle heading change. As Figure 5.9 shows, the alternate vectors are generated from the opposing aircraft's reference frame. This is transformed to the host aircraft reference frame by shifting the vector_distance array element values to the left for threats on the left side of the host vehicle (relative to the host longitudinal axis) and to the right for threats on the right side of the host vehicle. The magnitude of this shifting operation is such that the angular displacement of the threat LOS vector from the host vehicle

boresight vector is equal to the shift distance multiplied by the angular resolution of each element. The vector_distance array element magnitudes are then weighted so that the magnitudes are inversely proportional to the range between the host and the opposing aircraft.

A plot of the vector_distance array for a single opposing aircraft is shown in Figure 5.10. Figure 5.11 shows the vector_distance array evolution over time for a threat on a collision course. For both figures, The opposing aircraft's relative LOS angle is 296.7° and the relative velocity vector angle is 297.3°.

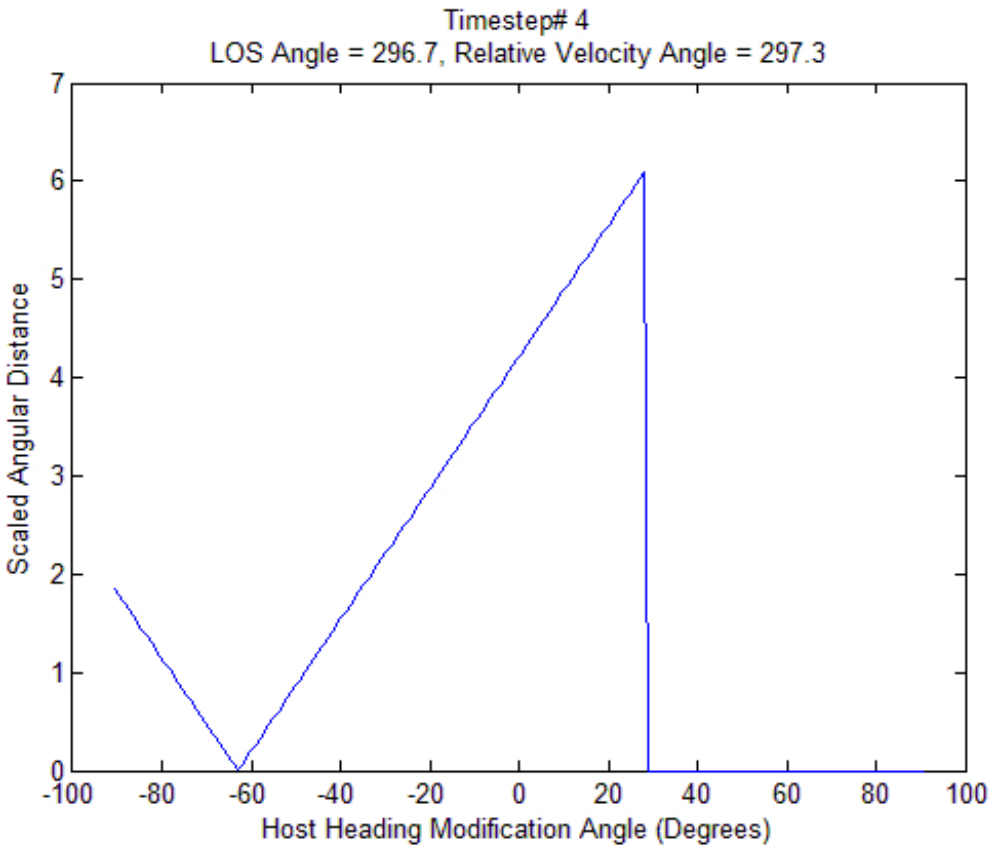

Figure 5.10: Plot of "vector_distance" Array After The Shifting And Weighting Operations

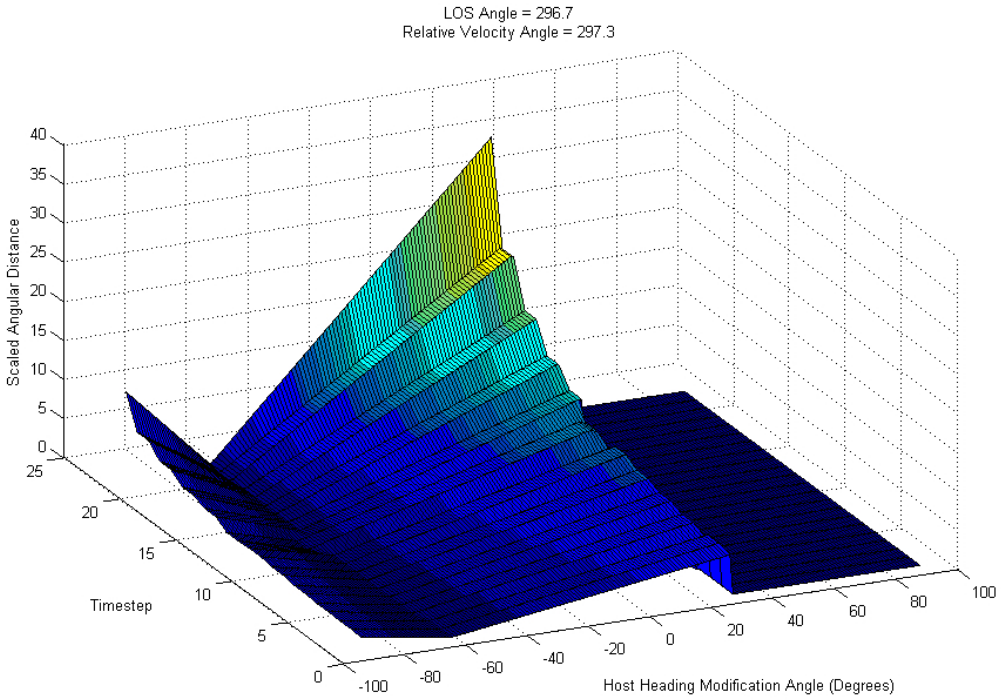

Figure 5.11: Plot of "vector_distance" Displayed Over Time

Once a vector_distance array is created for a particular opposing aircraft, it is added to a global array (known as the global_heading_distance array) which incorporates the vector_distance array values for all detected opposing aircraft (regardless of whether or not the aircraft in question is on a collision course). The heading modification angle is determined by finding the index of global maximum of the global_heading_distance array multiplied by the angular resolution of the generated alternate LOS vectors.

Throughout this research, 180 alternate LOS vectors are utilized for each opposing aircraft. The alternate LOS vectors are uniformly distributed throughout a 180° range resulting in an angular resolution of 1°.

The collision avoidance algorithm used in this research is described by the following pseudocode:

Require: Opposing Aircraft Velocity Vectors, LOS Vectors, Range

while $n < number\_of\_opposing\_vehicles$ **do**
  $global\_heading\_distance[all] \leftarrow 0$
  $Generate\_Alternate\_LOS\_Vectors\_For\_Vehicle\_n(n)$

  while $i < number\_of\_alternate\_LOS\_vectors$ **do**
    $vector\_distance[all] \leftarrow 0$
    $vector\_distance[i] \leftarrow abs(\angle alternate\_LOS[i] - \angle velocity\_vector)$
    $i = i + 1$
  end while

  if $\angle LOS[n] >= 0° and \angle LOS[n] <= 180°$ **then**
    $shift\_vector\_distance\_array\_right(\angle LOS[n])$
  else
    $shift\_vector\_distance\_array\_left(\angle LOS[n])$
  end if

  $vector\_distance[all] \leftarrow vector\_distance[all] \left(\frac{scaling\_factor}{range(n)}\right)$
  $global\_heading\_distance[] + vector\_distance[]$
  $n = n + 1$
end while

while $j < size(global\_heading\_distance[])$ **do**
  if $global\_heading\_distance[j] = global\_maxima$ **then**
    $break$
  end if
  $j = j + 1$
end while
$required\_heading\_modification\_angle = jxalternate\_LOS\_vector\_resolution$

The algorithm performance is evaluated by translating the method into *C* then executing the algorithm on the XC-1A development board used for RADAR control, as described in chapter 3. Execution time is indicated by setting an I/O pin to *logic 0* before execution of the algorithm then setting the same I/O pin to *logic 1*

upon completion of the algorithm. Execution time is measured by observing the state of the I/O pin using an oscilloscope (Agilent DSO5012A). The execution time measurement is performed for up to 20 opposing aircraft with 180 alternate LOS vectors per aircraft. The results are shown in Figure 5.12.

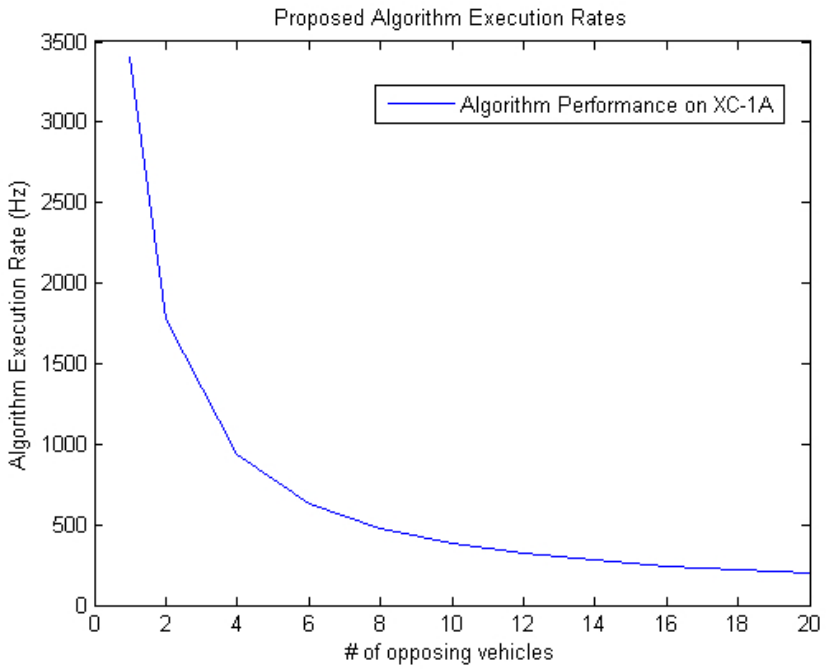

Figure 5.12: Algorithm Execution Rate On The RADAR Processor Hardware

5.4 Airspace Simulation Software

Due to the expense and difficulty of evaluating mid-air collision scenarios in hardware, algorithm evaluation takes place in simulation environment. To this end, a custom simulation software package was written in *Processing*, a branch of the Java programming language. This simulation software is comprised of a number of modules each responsible for a certain portion of the simulation. The modules each act

on a global state matrix that stores information on all aircraft within the simulation such as current coordinates, destination coordinates, velocity, exclusion region size, and aircraft maneuverability. The modules acting upon this data are as follows:

Initialization

The *initialization* module is executed upon the start of any given simulation sequence. While the module is routinely executed, the effect of the module is selectable to provide randomization of the positions, destinations, sizes, and velocities of all aircraft within the simulation.

Motion

The *motion* module's primary function is to update the current positions of all aircraft within the simulation based on the destination waypoint and the current velocity. As the global state matrix describes the vehicle position using latitude and longitude with precision of 0.111 meters, relatively fine positioning control over the various simulated aircraft is possible

Pilot Input

At any point in the simulation, a pilot may take control of the host aircraft using keyboard inputs. This has the effect of updating the "destination waypoint" for the host aircraft. Updates to this parameter are effected during the next simulation timestep.

RADAR Track Generator

This module serves to simulate the data as gathered by the RADAR sensor by sampling the global state matrix and generating RADAR track data. This module is capable of simulating the real-world parameters including: limited range, azimuth and range errors etc...

Performance Monitoring

The primary metric used for evaluating the effectiveness of the collision avoidance algorithms is the minimum distance between the host aircraft and any other aircraft in the simulation. This module records this parameter for further investigation.

Graphical Representation

As the name implies, the *graphical representation* module is responsible for parsing the global state matrix and displaying a graphical representation of the airspace. Also represented are pertinent values regarding the host vehicle parameters and the performance of the collision detection and avoidance software, see Figures 5.13. Due to the additional computational overhead involved in the rendering process, this module is only active during debugging when visual feedback is beneficial.

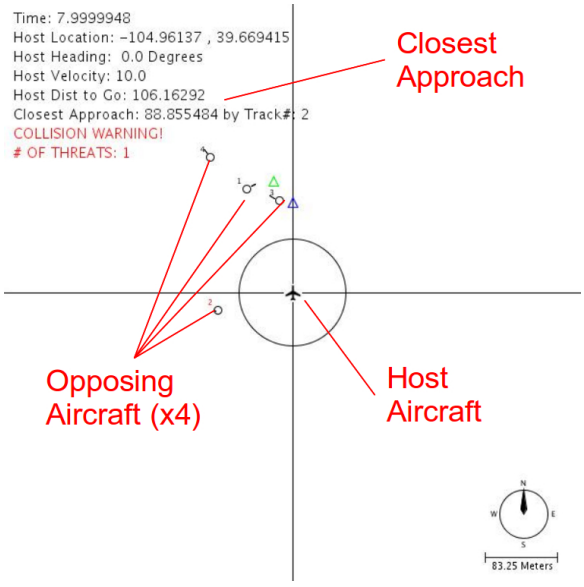

Figure 5.13: Airspace Simulation Software Screenshot

5.5 Collision Avoidance Algorithm Evaluation

The collision avoidance algorithm described in section 5.3 is evaluated using the collision avoidance simulation software described in the previous section. The goal of this evaluation is to examine the efficacy of collision avoidance maneuvers in the horizontal plane. There are, however, a number of key constraints placed upon the simulation environment. They are as follows:

Opposing Vehicle Initial and Final Range

Throughout the algorithm, the *initialization* module is configured to generate opposing aircraft with random initial locations and destinations. The random generation is constrained such that, upon initialization, the latitude or longitude of the start and end points are no closer than 200 meters and no further than 300 meters from the host aircraft. Thus, the initial LOS range between any aircraft and the host is between 282.8 meters and 424.3 meters. This prevents the spawning of opposing vehicles co-located with the host, additionally it provides time for the host vehicle to effect a collision avoidance maneuver.

Opposing Vehicle Dispersion Time

Due to the constraints place upon the locations of opposing aircraft, initial simulations indicated that opposing aircraft's starting locations may sometimes be generated closely together. Therefore, upon initializing any given scenario, collision avoidance maneuvers are inhibited for 2 seconds thus allowing the opposing aircraft to disperse. Failure to do so artificially improves the performance metrics of the algorithm since there are large swaths of empty airspace.

Vehicle Collision Radii

Throughout the simulation, all aircraft have a collision avoidance radii of 10 meters. This results in a collision being registered when the range between the host and any opposing aircraft within the simulation is less than 20 meters, see Figure 5.1. 10 meters is justified as a collision avoidance radius since it provides adequate clearance between many small UAVs and the maximum dimension of the Cessna 172 which has an 11 meter wingspan [65]. The Cessna 172, while not the most challenging threat to evade, is the most likely opposing aircraft in many municipalities since more Cessna 172s have been built than any other manned aircraft (more than 43,000 examples have been produced) [67].

Single Collision Avoidance Maneuver

Throughout the evaluation process, a single collision maneuver is permitted. This is to avoid a meandering, in-plane path which would consume more energy than a vertical maneuver.

Throughout the evaluation process, the simulated area represents a horizontal slice of extremely high density airspace. In this research, the slice is a square with an area of $0.36km^2$, although airspace density values are normalized to represent $\frac{aircraft}{km^2}$. For every major parameter variation, a batch of simulations are run to determine the effect for various airspace densities up to $55.6\frac{aircraft}{km^2}$. For each incremental increase in airspace density, the simulation is executed 10,000 times (10,000 random scenarios). A scenario is defined as lasting from the end of the randomization process used during the beginning of the simulation to the time when all aircraft have reached their destination waypoints. Although the duration of any given scenario will vary due to the random nature of the waypoints and the velocities of the aircraft involved, the

average duration of a scenario is 36.76 seconds. The results presented below represent 2.09 million scenarios (approximately 21,341 hours of simulated flight time). For all efficacy plots, the vertical axis represents the probability of a collision while the horizontal axis represents the airspace density.

Figure 5.14 displays the probability of a collision with and without the collision avoidance algorithm. Throughout the simulation, the velocities of all opposing aircraft are $20\frac{m}{s}$. Furthermore, the maximum heading modification angle is limited to 20° to approximate the theoretical vehicle described in table 5.1.

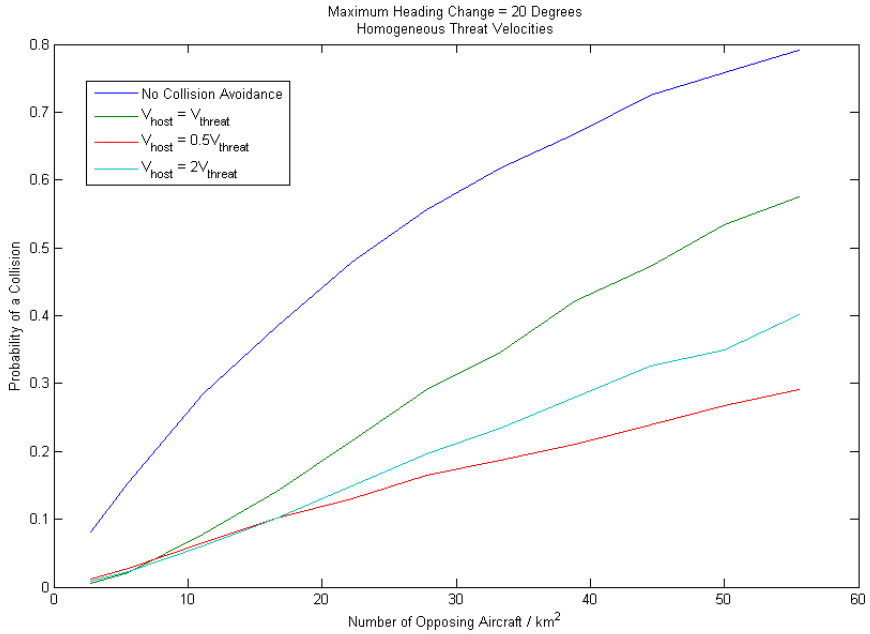

Figure 5.14: 20 Degree Heading Modification Angle

Figure 5.15 displays the effect of varying the maximum heading modification angle from the 20° used in figure 5.14. All vehicle velocities are $20\frac{m}{s}$.

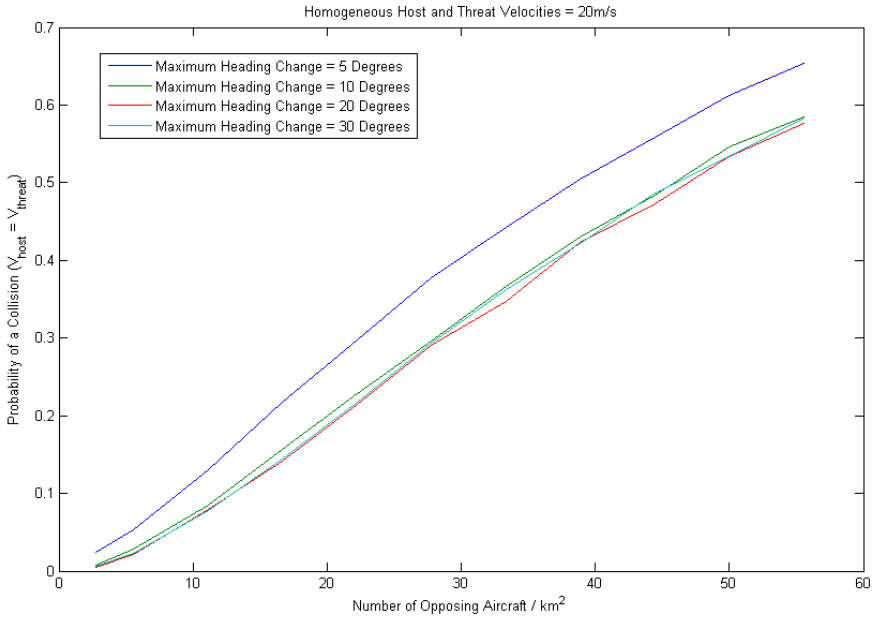

Figure 5.15: Various Heading Modification Angles

Figure 5.16 shows the efficacy of the algorithm utilizing a range of homogeneous opposing aircraft velocities and a fixed host aircraft velocity. The maximum heading modification angle is 20°.

Figure 5.17 shows the efficacy of the algorithm with a maximum heading modification angle of 20° and randomized opposing aircraft velocities between $10\frac{m}{s}$ and $40\frac{m}{s}$.

Figures 5.18, 5.19, 5.20, and 5.21 show the data from Figure 5.17 with and without collision avoidance enabled.

5.6 Remarks

Within this chapter, a geometric collision detection and evasion method is proposed and evaluated for a non-trivial number of random scenarios. Throughout the

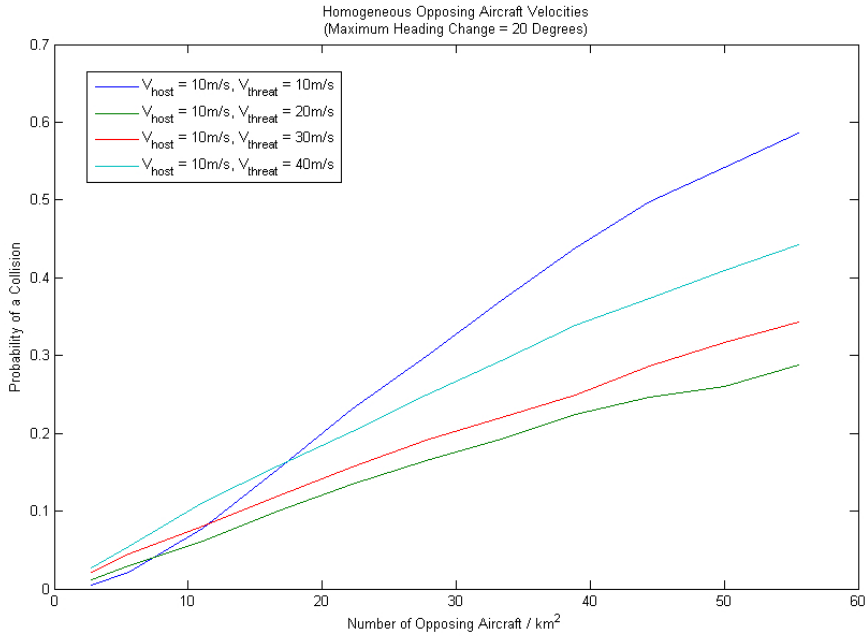

Figure 5.16: Various Homogeneous Opposing Aircraft Velocities with Constant Host Velocity

evaluation process, a number of key parameters are varied for each sweep of airspace densities: the maximum heading modification angle, velocities of both the host and the threat, and whether or not the scenario utilizes homogeneous or random opposing aircraft velocities.

Figure 5.15 shows the efficacy of the algorithm as a function of various maximum heading modification angles. The best performance within this data set occurs when the maximum heading modification angle is 20°. For values below 20° the host aircraft is unable to avoid flying into the collision region described in Figure 5.3. For values greater than 20° the host aircraft is able to clear the original collision region, but often initiates a collision with another aircraft in the process.

The efficacy of the algorithm is also affected by the velocities of the vehicles involved and the opposing aircraft velocity distribution. With homogeneous opposing

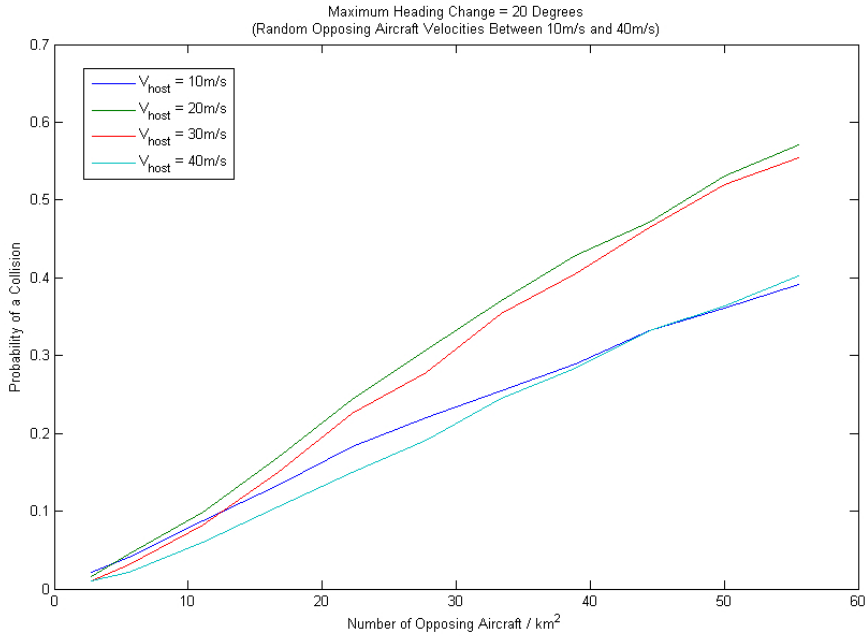

Figure 5.17: Random Opposing Aircraft Velocities with Host Velocity Sweep

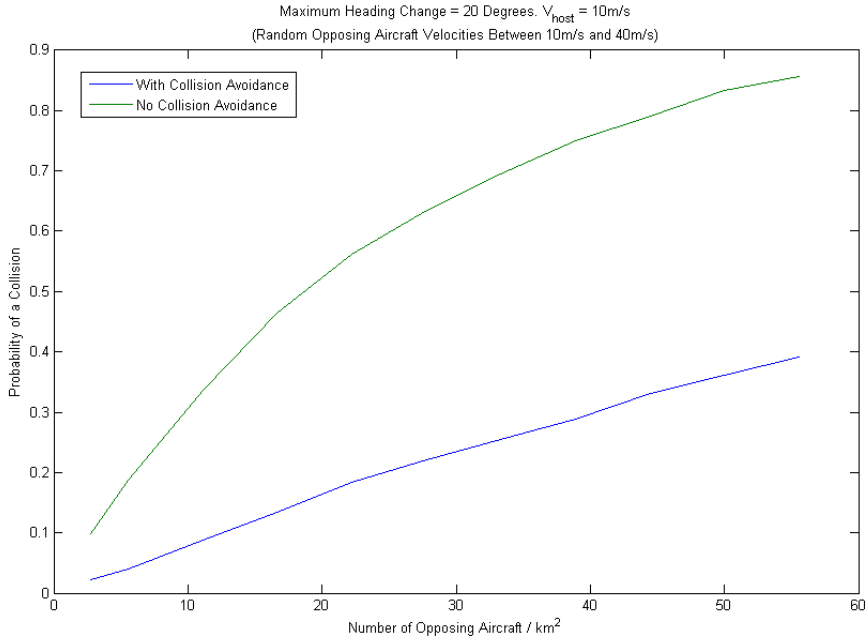

Figure 5.18: Random Opposing Aircraft Velocities with $10\frac{m}{s}$ Host

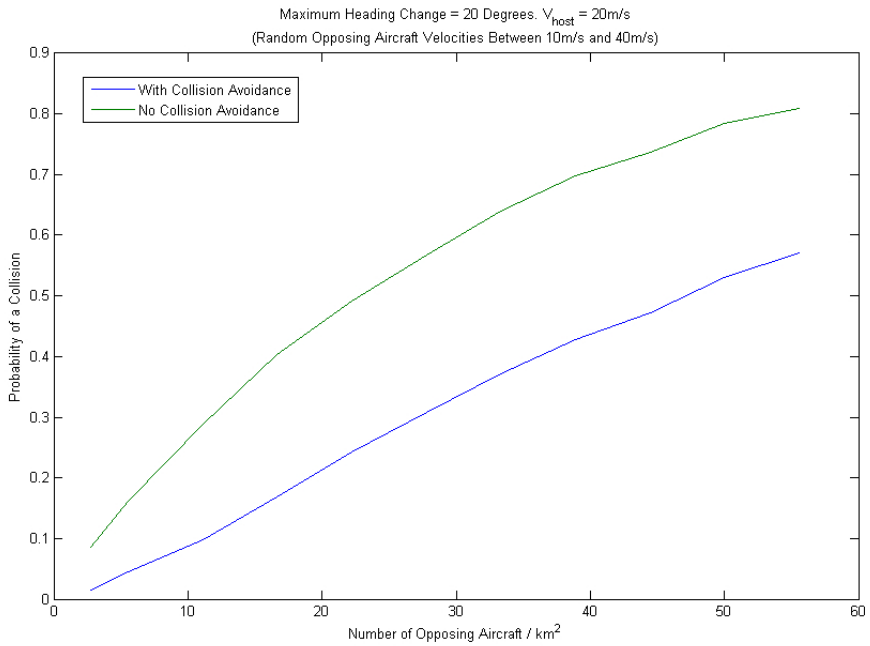

Figure 5.19: Random Opposing Aircraft Velocities with $20\frac{m}{s}$ Host

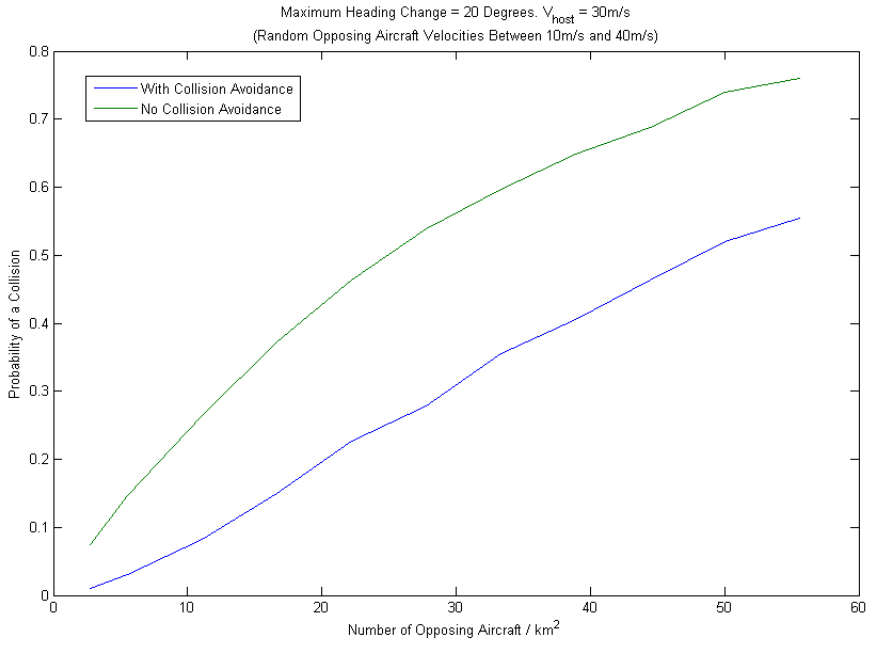

Figure 5.20: Random Opposing Aircraft Velocities with $30\frac{m}{s}$ Host

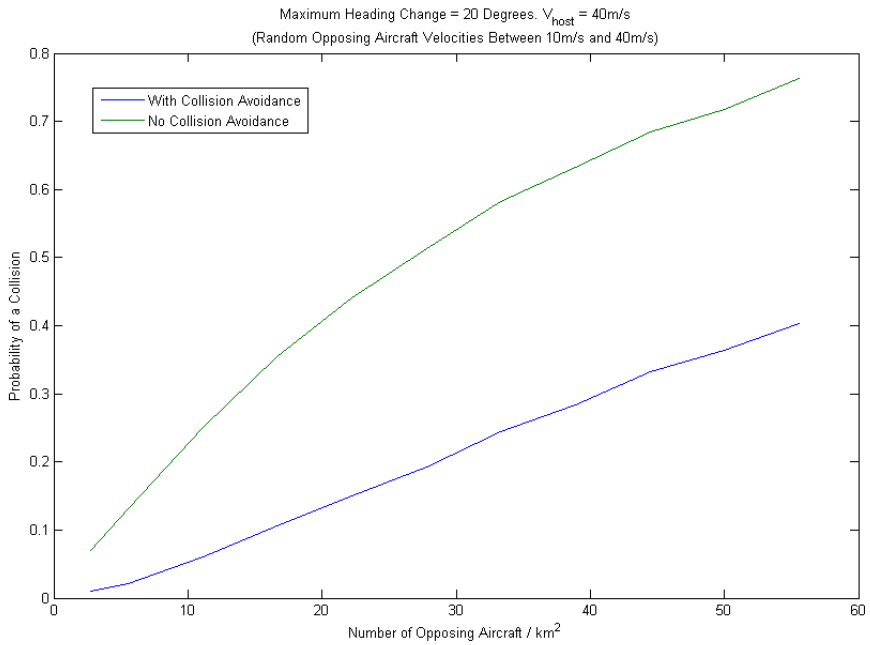

Figure 5.21: Random Opposing Aircraft Velocities with $40\frac{m}{s}$ Host

aircraft velocities, the simulations show that out of the examined configurations, the best efficacy is achieved when the host vehicle velocity is half the opposing vehicle velocity. With this velocity configuration, there is adequate time for the "cloud" of opposing aircraft to pass by the host vehicle. Increasing the host vehicle speed is detrimental to the performance in that it increases the closing speeds between the host and any opposing aircraft. This increased closing speed reduces the amount of time available for the host to clear the various collision regions.

The situation is reversed (for airspace densities up to $44\frac{aircraft}{km^2}$) once random opposing aircraft velocities are introduced. Under these conditions, the best efficacy achieved during this research occurs when the host vehicle velocity is equal to the upper bound of the opposing aircraft velocity distribution. This is explained by the "threat cloud" not dispersing due to the low speed vehicles. Simultaneously, the host

vehicle lacks to velocity to escape high velocity opposing aircraft which penetrate the cloud of low speed vehicles.

The efficacy of the algorithm is evaluated for airspace densities up to 55.56 $\frac{aircraft}{km^2}$ (see Figure 5.22) at which point the probability of a collision exceeds 30% for many of the scenarios in section 5.5. It should be noted, however, that such airspace densities are highly improbable. For the sake of example, it can be assumed that the highest airspace density occurs within the airspace surrounding airports (the FAA classifies these regions density as "Class B" airspace) [68]. The busiest airport in the world (according to the number of takeoffs and landings) is the Hartsfield-Jackson Atlanta International Airport (ATL) in Atlanta, Georgia with 950,119 such events in 2010 [69]. While ATL's class B airspace, see Figure 5.24, extends up to $56km$ from the airport itself, the physical area within which the runways are contained can be modeled as a rectangle $4.64km$ wide by $3.7km$ long, see Figure 5.25 [7][8]. This results in an area of $17.17km^2$ through which it is assumed all aircraft serviced by ATL must pass. The average duration of a scenario in section 5.5 is 36.76 seconds and there are 858,458.3 such time periods within a year. Assuming a uniform distribution of aircraft arrival and departures, throughout any given day there must be 1.1 flying aircraft over ATL every simulation period. This gives rise to an average airspace density of $0.0641\frac{aircraft}{km^2}$ which is 866.8 times less dense than the maximum airspace density simulated in this research. Stated another way, if ATL operated under the maximum airspace density used in this research, an aircraft would be either taking off or landing every 39 milliseconds ($25.9\frac{aircraft}{second}$).

Figure 5.23 shows the data in Figure 5.14 enlarged to provide more detail throughout lower airspace densities. With collision avoidance enabled, the worst case scenario in this data sequence occurs when the host vehicle is traveling at half the velocity of

the opposing aircraft. Extrapolating this data to represent ATL's airspace density results in the probability of a collision decreasing to 2.815x10^{-4}.

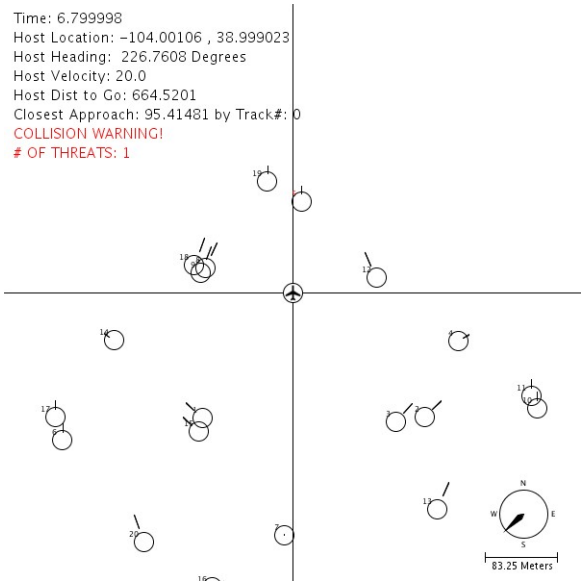

Figure 5.22: Airspace Simulation Screenshot with 55.56 $\frac{aircraft}{km^2}$

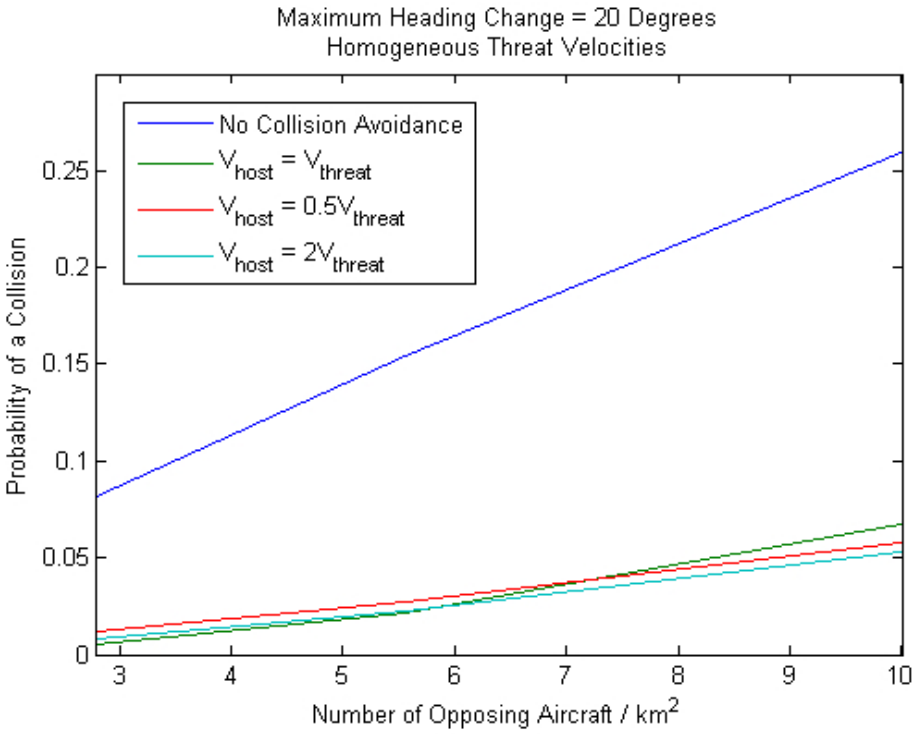

Figure 5.23: Data in Figure 5.14 for Lower Airspace Densities

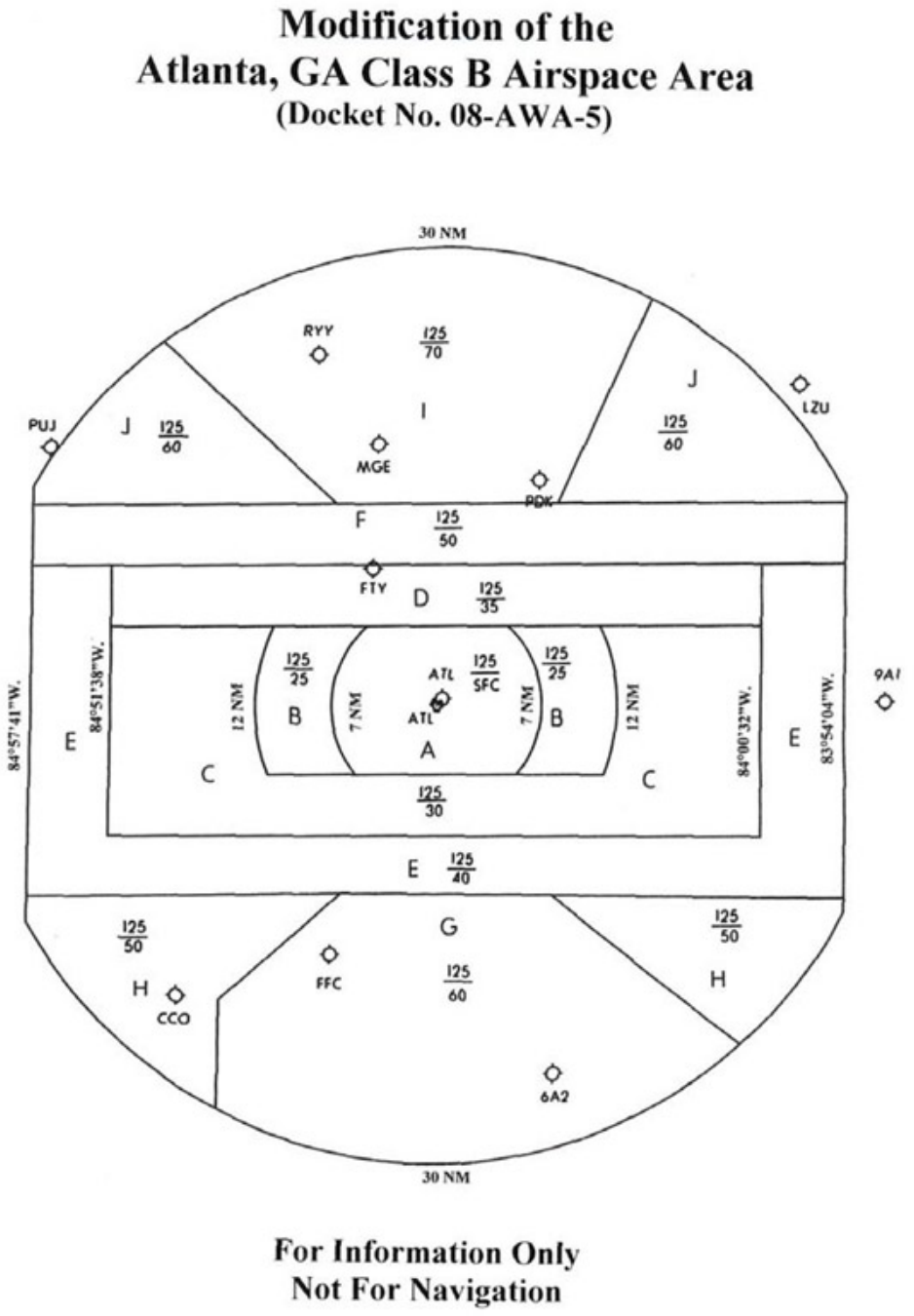

Figure 5.24: Atlanta International Airport Region Airspace Map [7]

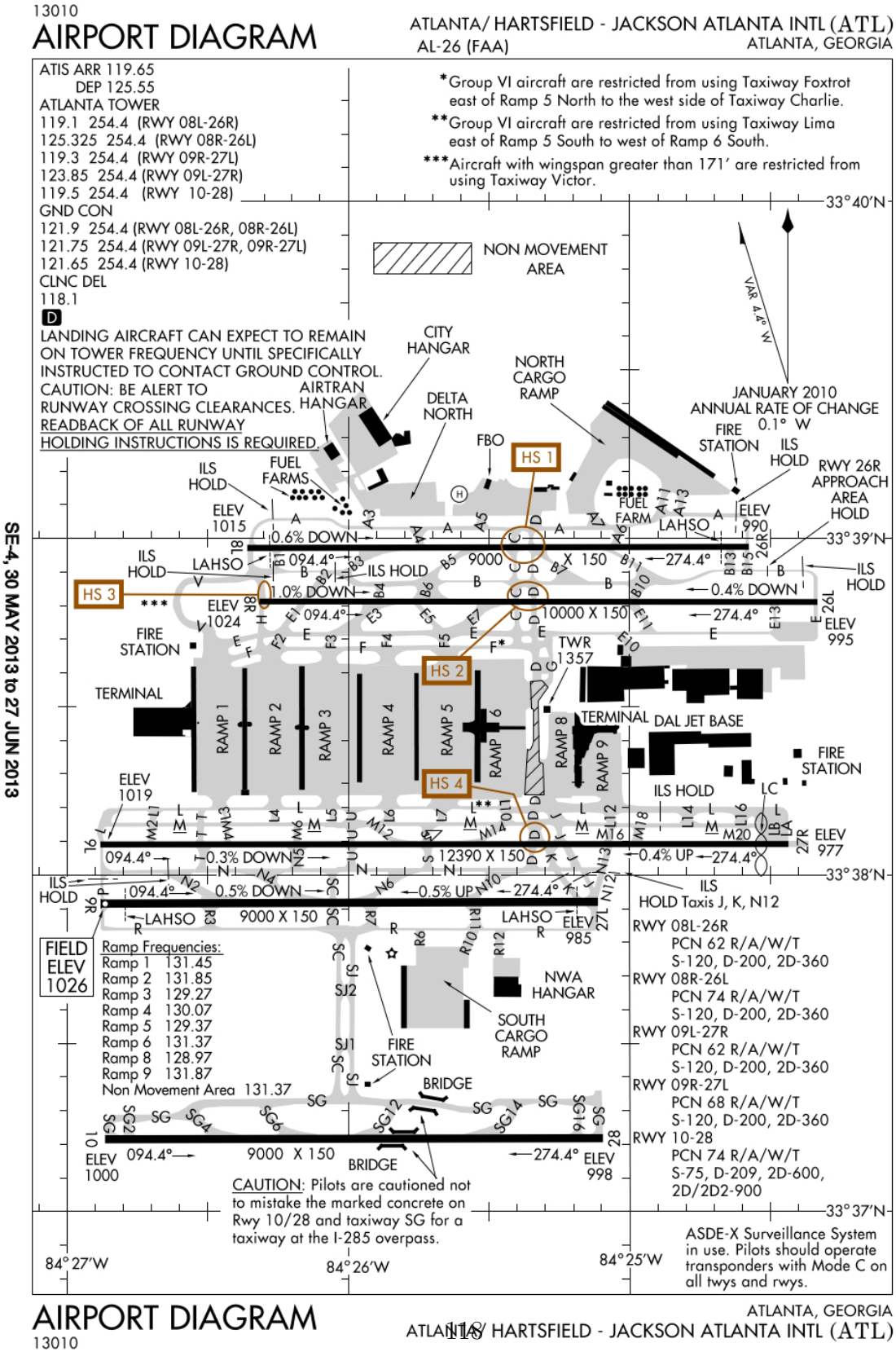

Figure 5.25: Atlanta International Airport Runway Map [8]

Chapter 6

Conclusions and Future Work

6.1 Conclusion

This research presents two components which aim to improve the safety of unmanned aircraft systems and ease their future integration into the national airspace. These components are: a lightweight RADAR sensor capable of not only detecting but also accurately identifying miniature aircraft, and a computationally efficient method for determining collision avoidance maneuvers.

Due to the limitations of the available hardware, the prototype RADAR sensor is evaluated on a small scale using mobile RADAR reflectors to simulate opposing aircraft. This process revealed a number of limitations. Nevertheless, the feasibility of miniature RADAR sensors for collision avoidance is demonstrated. While the hardware is evaluated on a small scale, the collision avoidance algorithm is evaluated extensively in order to characterize its efficacy well beyond the current maximum airspace density.

The uniqueness of this work is exemplified by the small numbers of miniature airborne RADAR systems ever created for the sense and avoid task. As such, certain aspects of this research are protected by U.S. provisional patent# 61/478,681. This research is also unique in that all the information required to create a functional RADAR sensor with accuracy comparable to commercial scanning laser rangefinders is presented within this dissertation. Replicating this research should be possible with few essential non-Commercially available Off The Shelf (COTS) hardware elements and the cost for doing so is anticipated to be well below the acquisition costs of many UAV platforms. It is hoped that other researchers will escalate the investigation of miniature RADAR sensors and non-cooperative collision avoidance techniques.

6.2 Future Work

The research performed up to this point can be advanced along two paths: hardware and algorithm development. The hardware developed throughout this research is suitable for demonstrating certain fundamental concepts. However, the low power and low update rates preclude its use as a drop-in sense and avoid system. Therefore, the future work must involve improving the overall detection range and update rate while maintaining sensor masses and volumes comparable with the hardware developed herein. This involves the fabrication of a new microwave front end in addition to the use of more powerful computing hardware.

Additionally, it should be noted that although FSKCW RADARs are suitable for higher altitude collision avoidance where the problems of multipath reflections are greatly reduced, many UAVs tend to operate in regions close to the ground.

Therefore, future RADARs should incorporate a number of different operating modes so that functionality can be maintained throughout various operating environments.

This research explored only a small subset of the available collision avoidance algorithms. In the immediate future, more sophisticated algorithms can be explored and the collision avoidance algorithms and simulation can be expanded to incorporate three dimensional maneuvers.

Finally, this research focuses on sensor-based non-cooperative collision avoidance. However, if sensors of the type developed in this research become widespread, problems caused by radio interference, jamming, and uncoordinated UAV behaviors will have to be addressed.

Bibliography

[1] Johann Borenstein and Yoram Koren. The vector field histogram fast obstacle avoidance for mobile robots. volume 7, pages 278–288. IEEE Robotics and Automation Society, 1991.

[2] International Telecommunication Union. *Recommendation P.676-9: Attenuation of Atmospheric Gases*, Feb 2012.

[3] Carlo Kopp. Technical report apa-tr-2007-0901. Technical report, Air Power Australia, September 2007.

[4] *Introduction to Radar Target Recognition*. Institute of Engineering and Technology, 2005.

[5] Philip G Gallman. *RADAR Reflectors For Cruising Sailboats*, chapter 6. Ulyssian Publications, 2005.

[6] Microwave Solutions. *MDU4210 datasheet*.

[7] Aircraft Owners and Pilots Association. *Atlanta Class B airspace changes take effect March 7*, January 2013.

[8] Federal Aviation Administration. *Atlanta Hartsfield Jackson Intl Airport Diagram*, May 2013.

[9] AeroVironment. Uas advanced development: Black widow.

[10] U.S. Air Force. Rq-4 global hawk. Technical report, U.S. Air Force, 2012.

[11] Kumar V. Shen S., Michael N. Autonomous multi-floor indoor navigation with a computationally constrained mav.

[12] Federal Aviation Administration. *TCAS Home Page*, 2012.

[13] ZAON Flight systems. *XRX User's Manual 2.0*, 2007.

[14] Flarm Technology. Flarm: Motivation. Technical report, FLARM, 2008.

[15] ADS-B Technologies. *ADS-B EXPLAINED*, 2011.

[16] Federal Aviation Administration. *Intorduction to TCAS II.* U.S. Depatrment of Transportation, version 7.1 edition, Feb 2011.

[17] Aircraft Owners and Pilots Association. What is general aviation.

[18] Sarasota Avionics International. Garmin gts850 tcas. http://sarasotaavionics.com/avionics/gts850-tcas-two-antennas, 2011.

[19] ZAON Flight systems. *PCAS MRX Overview*, 2011.

[20] Department of Transportation. 14 cfr part 91, May 2010.

[21] Selex ES. Laser obstacle avoidance system.

[22] Scientific Applications and Research Associates Inc. Optical collision avoidance.

[23] Scientific Applications and Research Associates Inc. Uav acoustic collision-alert system.

[24] Yoko Watanabe, Anthony J. Calise, and Eric N. Johnson. Vision-based obstacle avoidance for uavs. Guidance, Navigation and Control Conference, American Institute of Aeronautics and Astronautics, August 2007.

[25] Heinrich Hertz. *Electric Waves Being Researches on The Propagation of Electric Action with Finite Velocity Through Space.* Dover Publications, 1893.

[26] Arthur Bauer. *Christian Hulsmeyer and about the early days of radar inventions.* 2005.

[27] Greg Goebel. *Microwave Radar at War*, chapter 4. Feb 2013.

[28] Encyclopedia Britannica. Radar.

[29] Peter Tait. *Introduction to Radar Target Recognition*. Institution of Engineering and Technology, Jan 2006.

[30] ImSAR. Product page.

[31] An/zpy-1 starlite small tactical radar. Technical report, Northrop Grumman, 2013.

[32] Martin Schneider. Automoive radar status and trends. German Microwave Conference, 2005.

[33] V.V. Viikari, T. Varpula, and M. Kantanen. Road-condition recognition using 24-ghz automotive radar. *Intelligent Transportation Systems, IEEE Transactions on*, 10(4):639 –648, dec. 2009.

[34] A. Bartsch, F. Fitzek, and R.H. Rasshofer. Pedestrian recognation using automotive radar sensors. *Advances in Radio Science*, 10:45, 2012.

[35] W. Menzel and A. Moebius. Antenna concepts for millimeter-wave automotive radar sensors. *Proceedings of the IEEE*, 100(7):2372 –2379, july 2012.

[36] Richley. An ultra wideband radar for micro air vehicle applications. IEEE International.

[37] Viquerat. Reactive collision avoidance for unmanned aerial vehicles using doppler radar. International Conference on Field and Service Robotics.

[38] Bill Carey. Itt exelis shows sense and avoid radar for navy mq4c. AIN Online, August 2012.

[39] J. Wellman, R. Silvious. Doppler signature measurements of an mi24 hind d helicopter at 92ghz. Technical report, US Army Research Laboratory, 1998.

[40] Peregrine airspace protection system for denying small uav intrusion. http://www.sbir.gov/sbirsearch/detail/80318.

[41] Jose J. Ruz, Orlando Arevalo, Gonzalo Pajares, and Jesus M. de la Cruz. Decision making among alternative routes for uavs in dynamic environments. Emerging Technologies and Factory Automation. IEEE, 2007.

[42] Ankur Naik. Arc path collision avoidance algorithm for autonomous ground vehicles. Master's thesis, Virginia Polytechnic Institude and State University, December 2005.

[43] Thomas Crescenzi, Andrew Kaizer, and Tyler Young. Collision avoidance in uavs using dynamic sparse a*. Technical report, Auburn University, 2007.

[44] Lu fang Gao, Yu Xian Gai, Sheng Fu, and Hui ying Liu. Obstacle avoidance approach in dynamic environment using sonar range finder and optic mice. pages 423–428. IEEE International Conference on Robotics and Biomimetics, 2007.

[45] O. Khatib. Real-time obstacle avoidance for manipulators and mobile robots. In *Robotics and Automation. Proceedings. 1985 IEEE International Conference on*, volume 2, pages 500 – 505, mar 1985.

[46] *UAV Trajectory Design Using Total Field Collision Avoidance*. American Institute of Aeronautics and Astronautics, 2003.

[47] Jason Ruchti, Robert Senkbeil, James Carrol, James Holt, and Saad Biaz. Uav collision avoidance using artificial potential fields. Technical report, University of Aburn, July 2011.

[48] A. Richards and J.P. How. Aircraft trajectory planning with collision avoidance using mixed integer linear programming. In *American Control Conference, 2002. Proceedings of the 2002*, volume 3, pages 1936 – 1941 vol.3, 2002.

[49] John Saunders Bellingham. Coordination and control of uav fleets using mixed integer linear programming. Master's thesis, Massachusetts Institute of Technology, 2002.

[50] Roberto Conde, David Alejo, JoseAntonio Cobano, Antidio Viguria, and AnÃ-bal Ollero. Conflict detection and resolution method for cooperating unmanned aerial vehicles. *Journal of Intelligent & Robotic Systems*, 65:495–505, 2012.

[51] David Rathbun, Ph. D, Sean Kragelund, and Anawat Pongpunwattana. An evolution based path planning algorithm for autonomous motion of a uav through uncertain environments. In *Algebra Universalis*, pages 551–607, 2002.

[52] Jung-Woo Park, Hyon-Dong Oh, and Min-Jea Tahk. Uav collision avoidance based on geometric approach. In *SICE Annual Conference, 2008*, pages 2122 –2126, aug. 2008.

[53] Jimmy Krozel, Mark E Peters, and George Hunter. Conflict detection and resolution for future air transportation management. Technical report, Seagull Technology Inc, April 1997.

[54] Paolo Florini and Zvi Shiller. Motion planning in dynamic environments using velocity obstacles. *International Journal of Robotics Research*, 17, July 1998.

[55] Tracy V. Wallace, Randy J. Jost, and Paul E. Schmid. *Principles of Modern RADAR: Basic Principles*, chapter 10. 2010.

[56] *Introduction to Radar Systems*. McGraw-Hill, 1981.

[57] *Satellite Systems Engineering in an IPv6 Environment*, chapter 3. Auerbach Publications, 2009.

[58] Bob Richardson. *The Gunnplexer Cookbook*. The Ham Radio Publishing Group, 1981.

[59] *Antenna Engineering Handbook*, chapter 14 Horn Antennas. McGraw-Hill, 2007.

[60] Tower Hobbies. *Hobbico CS-80 Giant Scale 2BB Servo U*, February 1999.

[61] Pololu Corporation. *Pololu 3pi Robot User Guide*.

[62] Hokuyo Automatic CO LTD. *Scanning Laser Range Finder URG-04LX-UG01 Specifications*, August 2009.

[63] U.S. Department of Transportation. Order jo 7110.65u. Technical report, Federal Aviation Administration, 2012.

[64] Horizon Hobby. Ultra stick 25e arf. Technical report, 2013.

[65] Cessna Aircraft Company. *Pilot's Operating Handbook: Skyhawk 1978 Model 172N*, 1977.

[66] Bell Helicopter Textron Inc. *Bell Jetranger III Rotorcraft Flight Manual*, version 8 edition, October 2000.

[67] Russ Niles. Cessna to offer diesel skyhawk. AVweb, October 2007.

[68] Federal Aviation Administration. *Instrument Flying Handbook*. US Department of Transportation, 2001.

[69] ACI. Traffic movements 2010 final. Technical report, Airports Council International, 2011.